JOHANNES GUTENBERG UNIVERSITÄT MAINZ

Quest for an Ultracold Hybrid Atom-Ion Experiment

Masterarbeit

vorgelegt dem Institut für Physik
des Fachbereichs 08 – Physik, Mathematik und Informatik
der Johannes Gutenberg-Universität Mainz

von

Norman Vincenz Ewald

Mai 2015

Erstgutachter: Dr. René Gerritsma
Zweitgutachter: Univ.-Prof. Dr. Patrick Windpassinger

Abstract

The intention of this thesis is on the one hand to describe my contribution to the development and experimental progress of the currently evolving hybrid Li–Yb^+ experiment, as well as the analysis of the hybrid atom-ion systems in terms of analytical and numerical simulations. On the other hand, this thesis constitutes the first documentation of the entire experimental apparatus, planned sequence, and all laser setups in the context of the new research group HyQS.

This novel experiment should enable studies on the interactions of ultracold lithium atoms and cold ytterbium ions within the quantum regime. For this purpose, the atoms will get cooled to temperatures on the order of μK to nK inside an optical dipole trap. Evaporative cooling close to a Feshbach resonance allows for a wide range of tuneability of the interatomic interations, from attractive to vanishing and repulsive. This should pave the way to the observation of phases such as degenerate Fermi gases, molecular Bose-Einstein condensates and BCS-like phases. For trapping the ions, a radio frequency quadrupole trap is employed. Here, they crystallise in a controlled way into nearly periodic Coulomb crystals and therefore induce a band structure into the ultracold atom cloud. This emulates the scenario of an electron gas in a solid. The ultimate goal for this hybrid experiment is to become a quantum simulator for quantum mechanical phenomena of solid-state physics. Just before the submission of this thesis, the assembly of the ion trap and the vacuum system has been finished. All ion trap components are integrated. Withal, mostly all lasers have been installed. Therefore, the first photoionisation, trapping and Doppler-cooling of Yb^+ ions is within reach. Proximately, the completion of the Zeeman slower embodies the next step before atoms may get loaded into a magneto-optical trap, which serves as cooling pre-stage. Last but not least, the high-power ytterbium fibre laser will have to get installed, which will then create the optical dipole trap for lithium.

A significant amount of time has been spent building up two complete diode laser systems with external grating-stabilisation, including the control electronics for driving, thermally stabilising and fine tuning the laser diodes. They comprise the photoionisation laser of Yb at $\lambda = 398.9\,\mathrm{nm}$ and a re-repumper of Yb^+ at $\lambda = 638.6\,\mathrm{nm}$. Their readiness for use will be put to the test soon. Moreover, I have constructed five optical shutters for ultrafast control over the laser beams. Within the context of this thesis, I have investigated neutral-ion sympathetic cooling in theory, additionally. Emphasis is put on the impact of the atom-ion mass ratio $\mathfrak{M}_{\mathrm{ai}} = \frac{m_{\mathrm{a}}}{m_{\mathrm{i}}}$ and the ionic micromotion on hybrid collisions. Moreover, I explicate the eigenmodes of ion crystals with two and also three ions, since this is essential for the proposal of a two-ion detector. It should serve as a sympathetic dector for the atoms inside the optical dipole trap: One ion gets immersed into an ultracold atom cloud, while a second ion—the detection ion—is trapped besides. Coupling to this auxiliary ion happens via the crystal phonons. Together with the trap confinement, the interionic Coulomb interaction causes detectable changes in the motion of the detection ion, which arise from collisions of the immersed ion with atoms. The stability of these two-ion crystals is investigated.

Zusammenfassung

Entstehung eines ultrakalten hybriden Atom-Ionen-Experiments

Die Intention dieser Arbeit ist zum einen die Beteiligung an der Entwicklung und dem experimentellen Fortschritt des neu entstehenden hybriden Li–Yb^+-Experiments, als auch die Durchführung begleitender theoretischer Untersuchungen der hybriden Atom-Ionen-Systeme. Zum anderen stellt sie die erste derartige Dokumentation des kompletten Aufbaus, geplanten Ablaufs und der Lasersammlung im Rahmen der neu entstandenen Arbeitsgruppe HyQS dar.

In diesem hybriden Experiment sollen die Wechselwirkungen ultrakalter Lithium Atome mit kalten Ytterbium Ionen im Quantenregime erforscht werden. Hierfür werden die Atome in einer optischen Dipolfalle auf Temperaturen der Größenordnung μK bis nK herunter gekühlt. Evaporatives Kühlen nahe einer Feshbach-Resonanz ermöglicht es, die interatomare Wechselwirkung attraktiv, verschwindend oder auch repulsiv zu gestalten. Dies soll den Zugang zur Beobachtung von Phasen wie entarteten Fermi-Gasen, molekularen Bose-Einstein-Kondensaten, und BCS-verwandten Phasen ebnen. Eine Radiofrequenz-Quadrupol-Falle dient zum Fangen der Ionen. Dort kristallisieren sie kontrolliert zu Coulomb-Kristallen, die durch ihre nahezu räumliche Periodizität eine Bandstruktur in die ultrakalte Atomwolke induzieren. Dies emuliert das Szenario eines Elektronengases im Festkörper. Das höchste Ziel ist es, das hybride Experiment als Quantensimulator für quantenphysikalische Phänomene der Festkörperphysik einzusetzen. Zum Zeitpunkt der Abgabe dieser Arbeit wurde der Zusammenbau der Falle und des Vakuumsystems abgeschlossen, sowie diese miteinander vereint. Nahezu alle Laser sind aufgebaut, sodass alsbald mit dem Ionisieren, Fangen und Dopplerkühlen der Ionen begonnen werden kann. Danach stellt die Fertigstellung des Zeeman-Bremsers den nächsten Schritt zum Laden der Atome in die vorkühlende magneto-optische Falle dar. Zu guter Letzt wird der Hochleistungs-Ytterbium-Faserlaser installiert, der zur Erzeugung der optischen Dipolfalle für Lithium dient.

Als wesentlicher Teil dieser Arbeit wurden von mir zwei komplette Diodenlasersysteme mit externer Gitterstabilisierung samt Kontrollelektronik zum Treiben, thermischen Stabilisieren und Feinabstimmen der Laserdioden aufgebaut. Es handelt sich hierbei um den Photoionisationslaser von Yb bei $\lambda = 398.9\,\mathrm{nm}$ und einen Rück-Rückpumper von Yb^+ bei $\lambda = 638.6\,\mathrm{nm}$. Ihre Einsatzbereitschaft wird alsbald an der Ionenfalle getestet werden. Zudem wurden zur Kontrolle der Laserstrahlen fünf ultraschnelle optische Shutter von mir angefertigt. Im Rahmen dieser Arbeit habe ich außerdem das sympathetische Kühlen der Ionen durch die ultrakalten Atome theoretisch untersucht. Die Bedeutung des Massenverhältnisses zwischen Atom- und Ionenspezies $\mathfrak{M}_{\mathrm{ai}} = \frac{m_{\mathrm{a}}}{m_{\mathrm{i}}}$ und der Mikrobewegung für hybride Kollisionen wird betont. Zudem erläutere ich die Eigenmoden von Ionenkristallen mit zwei und drei Ionen, da diese essentiell für den Vorschlag eines Zwei-Ionendetektors sind. Dieser soll der sympathetischen Detektion von ultrakalten Atomen in der optischen Dipolfalle dienen: Hierzu wird ein Ion in die Atomwolke getränkt und das Zweite – das Detektions-Ion – bleibt außerhalb. Die Kopplung an das Detektions-Ion geschieht über die Phononen des Zwei-Ionenkristalls. Die interionische Coulombwechselwirkung sorgt gemeinsam mit dem Falleneinschluss für eine detektierbare Bewegungsänderung dieses Ions, welche von Kollisionen des eingetauchten Ions mit den Atomen herrührt. Die Stabilität dieser Zwei-Ionenkristalle wird untersucht.

Contents

List of Figures

List of Tables

Chapter 1

Hybridising Atom and Ion Quantum Systems: A Solid Look-Alike

Hybrid Atom-Ion Systems

Within the last decade, a novel domain of physics and quantum chemistry has emerged from the hybridisation of cold trapped ions and ultracold atomic gases [1, 2]. Two established fields are merging together, enabling a variety of new research on topics such as cold atom-ion collisions, ultracold chemistry, quantum information science, many-body and condensed matter physics [1, 2]. Only rather recently have the two quantum systems been combined successfully by immersing ions into ultracold atom clouds [3–5].

The hardest part in bringing hybrid atom-ion experiments to fruition is the challenge of integrating two overlapping traps for ions and atoms into a single apparatus [1]. To this date, all groups in this new field employ multipole radio frequency traps for the ions due to their superb controllability, but different traps for the atoms, namely magneto-optical traps [6–11], magnetic traps or optical dipole traps [2, 12, 13]. Setups using a MOT are well suited for studying chemical reactions such as charge transfer and molecule formation in the cold regime, but their minimal temperatures on the order of 100 μK are not sufficiently low enough to study, e.g., solid-state phenomena [1]. Here is where ODTs or magnetic traps are employed, since they allow reaching much lower temperatures, higher particle densities and are able to operate with atoms in their electronic ground state. The latter is essential in entering the quantum regime which is commonly delimited by the so-called s-wave scattering regime. To further improve the control over the ionic part, often a single ion is employed instead of a crystal which is then immersed into, e.g. a spin-polarized atomic bath [14], an ultracold atomic gas [15] or a BEC [16]. One exciting idea is to use such a hybrid atom-ion system as a quantum simulator for solid-state physics [17].

Quantum Simulation

In contemporary physics, *quantum simulation* has manifested itself as a key tool to understand, and conceptualise models of complex quantum phenomena [18–20]. Ranging from quantum optics to atomic, molecular, condensed matter and solid-state physics, its impact and platforms are quite diverse. In trying to understand the physics of, e.g. complex modern materials, their simulation is an irreplaceable tool. To push their development to the quantum regime, their simulation cannot be performed sufficiently efficient on a classical computer anymore [21, 22]. Its performance limits in the computation of many-body quantum systems. Due to the Hilbert space's exponential growth in dimensions with particle number, the required computational power and memory capacity for describing a many-body quantum system do so, too [18, 21–23]. Especially quantum mechanical attributes such as many-particle correlations and entanglement cannot be simulated on classical computers for large particle numbers.

To circumvent this issue, a mathematically akin, but physically dissimilar quantum system

can be employed that simulates the system of interest [19, 21]. This idea was first introduced by Richard P. Feynman in 1982 [21]. Since nature seems to be portrayed quantum mechanically, a quantum simulator inherently obeys the laws of quantum mechanics and physics. In some cases, a quantum simulator may also be referred to as a *quantum emulator* which mimics the basic physical properties of the genuine system, thus being at least to some extent *physically akin*. In our experiment, e.g., the intrinsically introduced band structure of ytterbium ions onto lithium atoms emulates the similar scenario as within a solid [17].

A crucial requirement a quantum simulator has to meet is its *controllability*—it has to outperform the one of the original system [18, 20]. Precise control is needed for state preparation to initialise the simulator in a specified state $|\Psi(t_{\text{init}})\rangle$, as well as for proper implementation of its evolution in time and subsequent detection. For this purpose, the corresponding Hamiltonian H is imprinted onto the quantum system by exploiting the *tuneability of internal and external interactions*. The *simulation result* is then given by the *final state of the simulator* $|\Psi(t_{\text{fin}})\rangle = \exp(-iHt_1/\hbar)\,|\Psi(t_{\text{init}})\rangle$, or more general its density matrix, which has to be read out by detection with sufficient fidelity at time t_{fin}. This holds for unitarily operating analogue quantum simulators, whereas digital quantum simulators discretise time and are based on algorithms of quantum gates [18, 24]. A quantum computer can then be identified as a universal digital quantum simulator [23, 24]. Besides possible universality of a quantum simulator, its scalability is another concern. In [25] a large scale quantum computer with modular architecture, i.e. a juxtaposition of atomic quantum memories and photonic qubit interconnections is proposed.

Platforms Used as Quantum Simulator

Realisations affirming at least a proof of concept of quantum simulators are achieved on diverse platforms with various simulation intentions such as:

Ions trapped in radio frequency traps [26, 27] are used to simulate spin-spin interaction models, e.g., Heisenberg and Ising models [28–31]. In general, quantum magnetism is vastly investigated, ranging from the smallest possible frustrated magnetic network, which consists of three antiferromagnetic quasi spin-$\frac{1}{2}$ particles arranged in a triangle [29], to frustration of multi-ion ground-states of complex two-dimensional crystals, e.g., two-leg zigzag ladders [28, 32–34] and hexagonal lattices [35]. Moreover, research is done on magnetic phase transitions [36] to, e.g., a quantum spin liquid [28]. Besides, digital quantum simulation with ions in radio frequency traps is demonstrated and investigated in [30] with sequences of up to 100 gates and 6 qubits that digitally simulate the full time dynamics of spin-$\frac{1}{2}$ systems.

Atoms may get trapped in optical dipole traps [37], enabling the quantum simulation of strongly correlated fermionic and bosonic few-body systems [38, 39], the transition from few- to many-body effects in reduced dimensions [40], and many-body physics like BEC and BCS phase transitions in ultracold Fermi gases [41] and BKT-phase transitions in strongly interacting 2D Bose gases [42]. Quantum gases in optical lattices form a unique tool to simulate models of strongly correlated quantum matter due to their wide range of exact parameter controllability [18, 43]. Here, the dynamics of electrons moving through a crystal lattice is simulated by the dynamics of ultracold atoms trapped by a web of laser light. The two main challenges are reaching nK temperatures for quantum effects to become dominant, and the lack of intrinsic long-range interactions between the atoms. Besides the study of solid-state phenomena such as quantum magnetism and the quantum Hall effect [44] with the help of, e.g., superfluid and Mott insulator phases [18, 43], quantum simulations on optical lattices are proposed for standard model tests for QCD [45], lattice gauge theories [46] and Higgs-mechanism [47].

Other platforms for quantum simulation include ultralong-range-interacting Rydberg molecules [48], NMR [49], circuit-QED systems for the simulation of spin models [50], superconducting circuits for the simulation of fermionic models [51] and the quantum Hall effect [52]. Moreover, photonic platforms are used which simulate, e.g., ground states of frustrated Heisenberg spin systems [53] and fermionic statistics [54] with entangled photons which are bosons.

Our Experiment and Choice of Species

We are currently developping a hybrid atom-ion experiment using a $^{6(7)}$Li–$^{171(174)}$Yb$^+$ combination as proposed in [17]. The ions will be be trapped in a linear quadrupole radio frequency trap, i.e. a Paul trap [26], where they arrange in periodic Coulomb crystals, and the fermionic (bosonic) atoms will be trapped in an ODT.

The concept for a quantum emulator is to replace a crystalline solid's electrons by the ultracold fermionic atoms, while its positively charged atomic cores get replaced by the ions. In analogy to a solid, an intrinsic phonon-fermion coupling exists—but this time between the motional modes of the ion crystal and the ultracold fermionic atoms—that induces a band structure in the atoms [17]: According to Bloch's theorem, periodic interaction potentials lead to a band structure with forbidden gaps in the atom spectrum, in analogy to a real solid [55]. In our case, a generalised periodic Kronig-Penney potential [55] serves as description [56]. More general than Bloch's theorem is Kramer's theorem, from which it follows that due to the crystal's translational invariance, an energy gap lifts the degeneracy of the fermions' energy at the borders of the Brillouin zones [57]. Consequently, the periodic translational invariance of the atom-ion potential and Hamiltonian lead to discrete allowed energy values and a band structure [57].

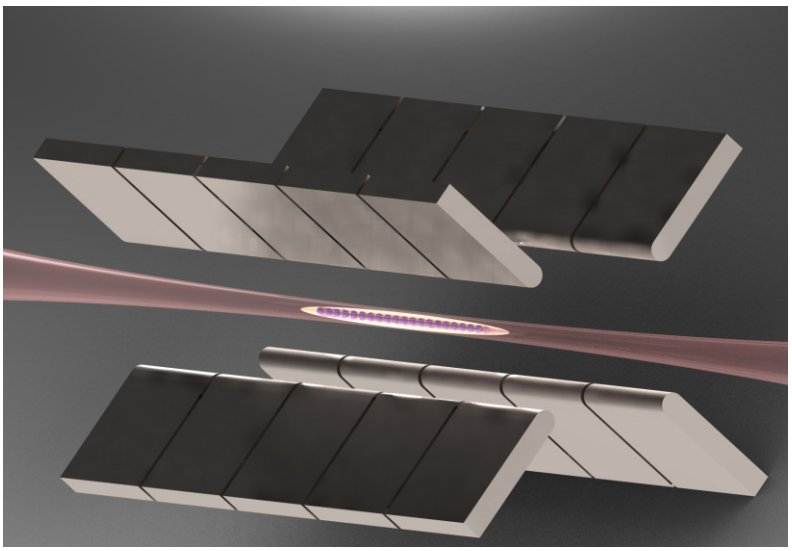

Figure 1.1.: Visualisation of an ion crystal immersed into an atom cloud. The (blue) Yb$^+$ ions will be trapped by the (grey) linear radio frequency quadrupole trap, and the atoms in an optical dipole trap, indicated by the red light beam.

Hybrid atom-ion systems combine the remarkable experimental controllability of the trapped atom and ion systems. These are the tight and well-controllable confinement of the ions allowing for extremely long storage times and strong localisation, and the strong inter-ionic interaction enabling single-site laser resolution within an ion crystal comparatively easy [1]. Neutral atoms can be prepared in large, and dense, but also dilute clouds of millions of atoms

due to their weak interaction [1]. Moreover, they can be cooled to temperatures on the order of nK, thus allowing for sympathetic cooling of ions [7, 11, 58, 59]. Another important feature is the controllability of the atom cloud's scattering properties via Feshbach resonances. Moreover, atom-ion Feshbach resonances are predicted to enable a wide tuneability of the hybrid interactions [59].

A temperature limit on the atom-ion mixture is set by the micromotion of the ions which is induced by the trap driving frequency of the radio frequency trap [58, 60]: The lowest temperatures achievable through neutral-ion sympathetic cooling strongly depend on the atom-ion mass ratio. In general, hybrid collisions cause heating due to excess kinetic energy in the micromotion [58, 60]. Our combination, ^{6}Li & $^{171}Yb^{+}$, has the highest experimentally feasible mass ratio of approximately 28, yielding the smallest relative heating due to collisions [58]—just 1 % compared to a ^{87}Rb–$^{171}Yb^{+}$-mixture with a mass ratio of ca. 2. Furthermore, our mixture exhibits a comparatively high s-wave limit of approximately 8.58 μK, as compared to 0.045 μK for Rb–Yb^{+}. This temperature seems to be within reach [58, 59]. Unwanted inelastic collisions, radiative charge transfer and radiative association are predicted to be at least 3 orders of magnitude lower in rate than elastic collisions between temperatures of 100 nK and 1 mK [59]. In addition, access to the regime of quantised ion motion should be granted [58].

Thesis Outline

Subsequent to this introduction, an introductory theory is given in chapter 2, starting with the description of trapped atomic ions in linear quadrupole RF traps, their micromotion, crystal stability and eigenmodes. It also involves the basics of ultracold quantum gases in optical dipole traps and the interactions of atoms and ions in hybrid traps.

The following two chapters are dedicated to the evolving experiment: First, the complete experimental apparatus and planned experimental procedure are depicted in chapter 3. Here, not only the hybrid trap made of a Paul trap and a ODT will be described, but also the Zeeman slower and MOT which are needed for the preparation of the atoms. Secondly, the lasers are logged in chapter 4. Their optical setups, characteristics and intended applications will be addressed. Here, special attention is paid to the two diode lasers with external cavity stabilisation that have been built up and installed in the context of this thesis.

Last but not least, atom-ion interactions are investigated theoretically in chapter 5 by means of analytical and numerical simulations. The neutral-ion sympathetically coolable mass ratio will be analysed, pointing out the benefits of the Li–Yb^{+} mixture. Next, the stability of a two-ion crystal will be analysed due to its importance for the proposal of the *two-ion detector*. It should enable sympathetic detection of the atoms via one interacting ion inside the atom cloud and one auxiliary detection ion for readout.

Chapter 2

Introductory Theory

This chapter provides the theoretical background of the individual quantum systems that make up the hybrid ultracold atom-ion system studied in this thesis. Firstly, atomic ions in RF[1] traps are described with special attention paid to the role of the dynamic trapping field due to its extensive impact on the hybrid interactions [58]. Secondly, neutral atoms in ODTs[2], and their low-energy collisional behaviour are sketched, followed by, thirdly, an explanation of atom-ion interactions in hybrid traps.

There exist multiple ways of trapping atomic ions, among which a linear RF quadrupole trap, named Paul trap, is the most widely employed trap geometry [26, 61–64]. More suitable for large numbers of charged particles—on the order of hundreds to thousands—are Penning traps which are based on a static electric quadrupole field and a constant magnetic field for trapping [63]. Another, rather recent approach utilises optical trapping of ions [65, 66] in ODTs, hitherto predominantly used for neutral atom trapping [37, 66–69].

2.1. Trapped Atomic Ions

2.1.1. RF Paul Trap

Before Maxwell's equations were published in 1863 [70], Earnshaw's theorem was already known for roughly 20 years [71]—stating, that pointlike charged particles cannot be held in a stable stationary equilibrium, i.e. get trapped, by exclusive electrostatic interactions or magnetic fields. This theorem applies to all classical inverse-square law forces of physics. Laplace's equation[3] incorporates this fact mathematically, $\Delta\Phi = 0$. Consequently, no local minima or maxima of the potential Φ can exist, but saddle points can. Flapping such a saddle potential—created by, e.g. an electric quadrupole field—in time with trap frequency Ω, traps the charged ions due to their inertia in the trap centre[4]. This is where the overall effective radial trapping potential, named pseudo-potential, vanishes. The harmonic trapping potential classically results in linear restoring forces, and can, based on [61, chap.2], be decomposed into a static part, proportional to the voltage U, and a sinusoidally oscillating part, proportional to the voltage $\tilde{U}$:

$$\Phi(x,y,z,t) = \frac{U}{2}\left(\alpha x^2 + \beta y^2 + \gamma z^2\right) + \frac{\tilde{U}}{2}\cos(\Omega t)\left(\tilde{\alpha}x^2 + \tilde{\beta}y^2 + \tilde{\gamma}z^2\right) . \tag{2.1}$$

$$\overset{\Delta\Phi=0}{\Longrightarrow} \qquad \alpha+\beta+\gamma = 0 \qquad \text{and} \qquad \tilde{\alpha}+\tilde{\beta}+\tilde{\gamma} = 0\,, \tag{2.2}$$

[1] radio frequency
[2] optical dipole traps
[3] Poisson's equation for charge-free space.
[4] Or trap axis in case of linear RF traps.

where the above conditions for the geometric factors $\alpha, \beta, \gamma, \tilde{\alpha}, \tilde{\beta}$ and $\tilde{\gamma}$ result from Laplace's equation. Their dimension is an inverse squared length.

The voltages applied to the trap electrodes are conventionally defined between spatially mutually opposite electrodes, fig. 3.5. The trap geometry can be set by the choice of the "static" and "RF" geometric factors α, β, γ and $\tilde{\alpha}, \tilde{\beta}, \tilde{\gamma}$, respectively. For a linear Paul trap with dynamical confinement in the x–y plane and static potential confinement for positively charged particles in the z-direction, the geometric factors fulfill the conditions [26, 61][1]:

$$-(\alpha+\beta) = \gamma > 0\,, \qquad \tilde{\alpha} = -\tilde{\beta}\,, \qquad \tilde{\gamma} = 0\,. \tag{2.3}$$

In an ideal Paul trap, the classical e.o.m.s[2] are decoupled in spatial coordinates. Therefore, only the 1D case needs to be discussed, the other are analogous[3]. The 1D classical e.o.m. is, in analogy to [61], given by:

$$m\ddot{x}(t) = -Ze\frac{\partial \Phi}{\partial x} = -Ze\left(U\alpha + \tilde{U}\cos(\Omega t)\,\tilde{\alpha}\right)x(t)\,, \tag{2.4}$$

where Ze is the ionic charge. In our case singly charged ions, $^{171\,(174)}\mathrm{Yb}^{+}$, will be used.

2.1.2. Secular and Micromotion

Commonly, the e.o.m. (2.4) gets transformed into the standard form of Mathieu's differential equation by making the convenient substitutions [61]:

$$\xi = \frac{\Omega t}{2}\,, \qquad a_x = \frac{4ZeU\alpha}{m\Omega^2}\,, \qquad q_x = -\frac{2Ze\tilde{U}\tilde{\alpha}}{m\Omega^2} \tag{2.5}$$

$$\Rightarrow \quad \frac{d^2x(\xi)}{d\xi^2} + \Big(a_x - 2q_x\cos(2\xi)\Big)x(\xi) = 0\,. \tag{2.6}$$

This differential equation exhibits periodic coefficients and according to Floquet theorem, the general Ansatz for stable solutions can be written as [61]:

$$x(\xi) = Ae^{i\beta_x\xi}\sum_{n=-\infty}^{\infty} C_{2n}e^{i2n\xi} + Be^{-i\beta_x\xi}\sum_{n=-\infty}^{\infty} C_{2n}e^{-i2n\xi}\,. \tag{2.7}$$

Here, the real valued characteristic exponent β_x and the coefficients C_{2n} are functions of a_x and q_x only, and do not depend on the initial conditions to be chosen. To fulfill boundary conditions, amplitudes A and $B \in \mathbb{C}$ can be matched accordingly. Plugging the Floquet series Ansatz (2.7) into the e.o.m. (2.6) results in a recursion relation:

$$C_{2n+2} - D_{2n}C_{2n} + C_{2n-2} = 0 \qquad \text{with} \qquad D_{2n} = \frac{a_x - (2n+\beta_x)^2}{q_x}\,. \tag{2.8}$$

Purposeful rearrangements and recursive use of (2.8) yield two continued fractions, linking C_{2n} with neighbouring coefficients of the recursion C_{2n-2} and C_{2n+2}:

$$\frac{C_{2n}}{C_{2n+2}} = \frac{1}{D_{2n} - \frac{1}{D_{2n-2} - \frac{1}{D_{2n-4} - \frac{1}{\ddots}}}} \qquad \text{and} \qquad \frac{C_{2n}}{C_{2n-2}} = \frac{1}{D_{2n} - \frac{1}{D_{2n+2} - \frac{1}{D_{2n+4} - \frac{1}{\ddots}}}}\,. \tag{2.9}$$

[1] Note the deviating axes-labelling of the three spatial Cartesian coordinates in [26, 61, 64], and thus different signs for the Mathieu parameters, etc.

[2] equations of motion

[3] Except for conventional signs.

Inserting (2.9) into (2.8) gives an expression for D_{2n}:

$$D_{2n} = \frac{1}{D_{2n-2} - \frac{1}{D_{2n-4} - \frac{1}{\ddots}}} + \frac{1}{D_{2n+2} - \frac{1}{D_{2n+4} - \frac{1}{\ddots}}} , \tag{2.10}$$

and setting $n = 0$ results in $D_0 = \frac{a_x - \beta_x^2}{q_x}$, and thus a relation for β_x:

$$\beta_x^2 = a_x - q_x \left(\frac{1}{D_{-2} - \frac{1}{D_{-4} - \frac{1}{D_{-6} - \frac{1}{\ddots}}}} + \frac{1}{D_2 - \frac{1}{D_4 - \frac{1}{D_6 - \frac{1}{\ddots}}}} \right) . \tag{2.11}$$

Chopping the implicit continued fractions in (2.11)[1] at the step of desired accuracy gives numerical values for β and the coefficients. Note however, that the right-hand side of (2.11) still depends on β itself. It's also worth noticing, that the contributions from higher order terms to the continued fraction rapidly drop. For the case usually referred to, one chops at $n = \pm 1$, i.e. assuming $C_{\pm 4} \simeq 0$, and subsequently performs a Taylor expansion in q around 0, keeping terms up to first order. From this, one obtains the relation [61]:

$$\beta_x \overset{|a_x|, q_x^2 \ll 1}{\approx} \sqrt{a_x + \frac{q_x^2}{2}} , \tag{2.12}$$

which results in the motional harmonic approximation (2.18) that will be introduced in the following. Consequently, β only depends on the Mathieu parameters a and q, or, expressed in terms of experimental parameters, on the static and RF voltages, U and $\tilde{U}$, and the RF trap frequency Ω, $\beta = \beta(a_i, q_i) = \beta(U, \tilde{U}, \Omega)$—for a chosen ion species.

The stability regions for each spatial coordinate $i \in \{x, y, z\}$ are determined by pairs of a_i and q_i, resulting in characteristic exponents β_i between $0 \leq \beta_i \leq 1$, for all $i \in \{x, y, z\}$. Equality holds for the edges of the stability region [61]. To provide an overview, the three interesting codomains of β values are discriminated in tab. 2.1. Since complex β's lead to real exponential functions in the series Ansatz (2.7), their solutions all have an exponential amplitude growth in time and are thus all instable. Integer β's correspond to the edges of the stability region which are not stable in the long run.

β_i's codomain	impact of $e^{i\beta_i \xi}$	stability of solution
$\mathbb{C}$	exponential amplitude growth	all instable
$\mathbb{R} \setminus \mathbb{Z}$	oscillation with const. ampl.	periodic and stable
$\mathbb{Z}$	oscillation with increasing ampl.	periodic, but instable ($\hat{=}$ edges of stability regions)

Table 2.1.: Stability of the secular motion in dependence of the characteristic exponent β.

From this, $\beta \in [0, 1]$, a condition for the radicand in the harmonic approximation for β (2.12) can be deduced, setting also a lower limit for a, conditional on q. Besides the upper limits for a and q forced by the harmonic approximation, the lower limit for a follows from the radicand's

[1] Note that these equations deviate from the ones in review reference "Quantum dynamics of single trapped ions" [64].

indispensable positivity:

$$|a_i|, q_i^2 \ll 1 \qquad \text{and} \qquad a_i > -\frac{q_i^2}{2}\,. \tag{2.13}$$

The choice of the geometric factors in (2.3) made for the linear Paul trap geometry, yields conditions for the static and dynamic Mathieu parameters [61]:

$$q_y = -q_x\,, \qquad q_z = 0\,, \qquad \text{and} \qquad a_x = a_y = -\frac{1}{2}a_z\,. \tag{2.14}$$

The opposite sign in the first expression means, that the RF voltages applied to neighbouring rods, $\tilde{U} \equiv U_{\mathrm{RF}}$, are out of phase. From $q_z = 0$, it follows in harmonic approximation, that no micromotion can be observed along the trap axis z. Therefore, the time-independent, effective axial harmonic trapping potential, as separable part of (2.1), can be written as $\Phi_{\mathrm{axial}} = \gamma\frac{U}{2}z^2$. Combined with (2.4) and (2.14), yielding the e.o.m. and axial trapping frequency ω_z [72]:

$$m\ddot{z}(t) = -Ze\frac{\partial\Phi}{\partial z} = -ZeU\gamma z(t) \tag{2.15}$$

$$\omega_z := \beta_z\frac{\Omega}{2} = \sqrt{a_z}\frac{\Omega}{2} = \sqrt{-2a_\rho}\frac{\Omega}{2} = \sqrt{\frac{ZeU\gamma}{m_i}}\,. \tag{2.16}$$

Furthermore, the radial modes are degenerate and can be expressed in terms of the axial frequency ω_z and the radial Mathieu parameter $q_\rho := q_x$ [72]:

$$\omega_r := \omega_x = \omega_y = \frac{\Omega}{2}\sqrt{a_\rho + \frac{q_\rho^2}{2}} = \frac{\Omega}{2}\sqrt{\frac{q_\rho^2}{2} - 2\left(\frac{\omega_z}{\Omega}\right)^2}\,. \tag{2.17}$$

The region where (2.12) holds, is the so-called sability region I, which is characterised by small q_i and a_i, or more specifically $|a|, q^2 \ll 1$ [61, 64]. Here, the "lowest order classical motion" [61] with $C_{\pm 4} \simeq 0$ can be written in terms of two superimposed oscillations on different time scales with real angular frequencies, usually reffered to as the slow (ω_i) secular motion[1], and the fast (Ω) micromotion:

$$x(t) \approx \underbrace{x_{\mathrm{c}}}_{:=2A\cdot C_0} \cdot \cos(\omega_x t)\left[1 - \frac{q_x}{2}\cos(\Omega t)\right] \quad \text{and} \quad \omega_i = \beta_i\frac{\Omega}{2} \approx \sqrt{a_i + \frac{q_i^2}{2}}\frac{\Omega}{2}\,. \tag{2.18}$$

Here, the $2A$ as part of the complex amplitude x_{c}, and the first slow cos-oscillation result from an adequate choice of boundary conditions in the Floquet series ansatz (2.7), namely $B = A$. It's worth noticing, that $A = A(\boldsymbol{p}_0, \boldsymbol{x}_0, \phi_0) \in \mathbb{C}$ depends on the ion's initial conditions only, its momentum $\boldsymbol{p}_0$, position $\boldsymbol{x}_0$, and phase ϕ_0 w.r.t.[2] the trap field, whereas $C_0 = C_0(a_i, q_i) \in \mathbb{R}$ incorporates trap characteristics such as geometry, applied voltages, radio frequency, and also properties of the chosen ion species, m_i and Z. Alternatively, one can rewrite the complex amplitude $2AC_0$, by splitting the x-trajactory into two linearly independent terms:

$$x(t) = x_{\mathrm{C}}\cos(\omega t)\left(1 + \frac{q}{2}\cos(\Omega t)\right) + x_{\mathrm{S}}\sin(\omega t)\left(1 + \frac{q}{2}\cos(\Omega t)\right)\,. \tag{2.19}$$

In "Trapping and cooling of atomic ions" [61], it is shown, that the present analysis also has a quantum analoque, just as e.g. in "Micromotion in trapped atom-ion systems" [60].

[1] also called macromotion

[2] with respect to

2.1.3. Coulomb Ion Crystals

Crystallisation of ions requires preparatory cooling into the low motional regime. This is achieved by laser cooling with diverse techniques, among which the ones that will be used in our experiment will be discussed in chapter 4. When the motional and thermal excitation is suppressed strong enough in comparison to the interionic Coulomb repulsion, the ions crystallise into, e.g. a 1D string or more complex multidimensional crystals, as e.g. a 2D *zigzag* crystal, depending on the trapping parameters and number of ions [33]. Since the crystal stability will be investigated further in sec. 5.3 among others, special interest lies in the ions' equilibrium positions and crystal eigenmodes. The descriptions on eigenmodes, dispersion relations and phase transitions in planar ion crystals in [32, 73, 74] served as additional references.

In the following, the quasi-one-dimensional trapping scenario, and crystals of single ion species are assumed, in analogy to [75].[1] Strong binding in the radial directions, x and y, compared to rather loose axial confinement suppresses motion along the radial axes, i.e. $\omega_x, \omega_y \gg \omega_z$. This important characteristic for the crystal stability is expressed in the trap anisotropy parameter $\alpha = (\frac{\omega_z}{\omega_i})^2$, for $i = x, y$ [33]. N_i ions of mass m_i and charge Ze, trapped at positions $\boldsymbol{x}_m(t)$, i.e. axially $z_m(t)$, experience the overall harmonic trapping potential and also the interionic Coulomb force on each single m-th of them:

$$F_{\mathrm{C},m} = \sum_{n\neq m}^{N_i} \kappa (Ze)^2 \frac{z_m(t) - z_n(t)}{|z_m(t) - z_n(t)|^3} \,, \tag{2.20}$$

m being counted along the axial direction from left to right, starting with the smallest z_m. Here, $\kappa := \frac{1}{4\pi\varepsilon_0}$ has been introduced, with ε_0 being the permittivity of free space. Jointly, yielding the potential energy of the ion crystal:

$$V_{\mathrm{crystal}} = \sum_{m=1}^{N_i} V_{\mathrm{ext}}(z_m) + \frac{1}{2} \sum_{\substack{n,m=1 \\ m\neq n}}^{N_i} V_{\mathrm{int}}(|z_m - z_n|) \tag{2.21}$$

$$= \sum_{m=1}^{N_i} \frac{1}{2} m_i \omega_z^2 z_m^2(t) + \frac{1}{2} \sum_{\substack{n,m=1 \\ m\neq n}}^{N_i} \kappa \left(Ze\right)^2 \frac{1}{|z_n(t) - z_m(t)|} \,. \tag{2.22}$$

Since crystallisation occurs when the motional excitation energy is comparatively small to the binding energy, which pins the ions to their equilibrium positions $x_m^{(0)}$, it is convenient to express the trajectories in terms of small displacements [75], $x_m(t) \approx x_m^{(0)} + q_m(t)$. With this and the typical length scale $l^3 := \frac{\kappa Z^2 e^2}{m_i \Omega^2}$, the energy minimising the dimensionless equilibrium positions $u_m = x_m^{(0)}/l$ obey a N_i-fold set of algebraic equations [75]:

$$u_m - \sum_{n=1}^{m-1} \frac{1}{(u_m - u_n)^2} + \sum_{n=m+1}^{N_i} \frac{1}{(u_m - u_n)^2} = 0 \quad \text{for} \quad m = 1, \ldots, N_i \,. \tag{2.23}$$

The description of the crystal eigenmodes will play a crucial role in a subsequent section, sec. 5.4,

[1] For comparison and an even more general theoretical description, [76] is drawn on.

especially for the cases of $N_i = \{2, 3\}$, where analytical solutions to (2.23) can be found[1]:

$$N = 2: \qquad u_1 = -(1/2)^{2/3} = -u_2 \tag{2.24}$$

$$N = 3: \qquad u_1 = -(5/4)^{1/3} = -u_3 \qquad \text{and} \qquad u_2 = 0\,. \tag{2.25}$$

Numerically determined values for higher numbers of ions are listed in [75]. The crystal potential's Hessian matrix is needed to describe the harmonic ion dynamics with a Lagrangian:

$$L = \frac{m_i}{2}\sum_{m=1}^{N_i}\dot{q}_m^2 - \frac{1}{2}\sum_{n,m=1}^{N_i} q_n q_m \left[\frac{\partial^2 V_{\text{crystal}}}{\partial x_n \partial x_m}\right]_{q_n=q_m=0} \tag{2.26}$$

$$= \frac{m_i}{2}\Big[\sum_{m=1}^{N_i}\dot{q}_m^2 - \omega_x^2 \sum_{n,m=1}^{N_i} A_{nm} q_n q_m\Big]\,. \tag{2.27}$$

Here, the matrix elements A_{nm} account for mutual coupling between the ions resulting from position shifts from their equilibrium positions, and is given by:

$$A_{nm} = \begin{cases} 1 + 2\sum\limits_{\substack{p=1\\ p\neq m}}^{N_i} \frac{1}{|u_m - u_n|^3}, & n = m \\ -\frac{2}{|u_m - u_n|^3}, & n \neq m\,. \end{cases} \tag{2.28}$$

The eigenvalues of A are positive, since physicality and symmetry of the Coulomb interaction demand the matrix to be real, symmetric and non-negative definite [75]. Consequently, the ion crystal's motional eigenmodes can be expressed in an ONB[2] of eigenvectors $\boldsymbol{b}_m^{(p)}$, for ions $p = 1, \ldots, N_i$ with corresponding eigenvalues $\mu_p \geq 0$:

$$\sum_{n=1}^{N_i} A_{nm}\boldsymbol{b}_n^{(p)} = \mu_p \boldsymbol{b}_m^{(p)} \quad (p = 1, \ldots, N_i)\,. \tag{2.29}$$

In the case of a 2- or 3-ion string, the eigensystem can be determined algebraically [75], and the resulting eigenvectors and eigenvalues for axial and radial directions are listed in tab. 2.2. For long chains with a large number of ions, statistical mechanics is the commom way of description, e.g. in [77].

The ionic motion's *normal modes* are given by $Q_p(t) = \sum_{m=1}^{N_i} \boldsymbol{b}_m^{(p)} q_m(t) = \boldsymbol{b}_m^{(p)} \cdot \boldsymbol{q}_m(t)$ [75]. Collective oscillation of all ions in phase with the same amplitude, corresponding to $\boldsymbol{b}^{(1)}$, is called the *COM*[3] *mode*, $Q_1(t)$. It's eigenvalue is $\mu_1 = 1$, and thus eigenfrequency $\omega_{\text{COM}} = \omega_z$. The second mode, Q_2, describes ions oscillating with an amplitude proportional to their distance from the trap centre, and is referred to as *stretch mode*. This mode is also reffered to as the *breathing* or *shear mode* in the axial or radial directions, respectively. In the axial case considered in the above calculations, its eigenvalue is $\mu_2 = 3$ and hence, $\omega_{\text{str}} = \sqrt{3}\omega_z$. For three trapped ions, there also exists Q_3, corresponding to $\boldsymbol{b}^{(3)}$, with $\mu_3 = \frac{29}{5}$, and thus $\omega_{\text{Egyptian}} = \sqrt{29/5}\,\omega_z$—the so-called *Egyptian mode*, named after the stylised walking like an Egyptian as depicted in ancient Egyptian ornate art of masonry. Self-evidently, these modes exist for each spatial direction of oscillation, x, y and / or z, although the eigenfrequencies differ, as mentioned above.

[1] The single-ion case is trivial, since there is no inter-ionic Coulomb interaction.

[2] orthonormal basis

[3] centre of mass

N_i	axial			radial		
	COM $\mu_1 = 1$ $\boldsymbol{b}^{(1)}$	stretch $\mu_2 = 3$ $\boldsymbol{b}^{(2)}$	Egyptian $\mu_3 = \frac{29}{5}$ $\boldsymbol{b}^{(3)}$	COM $\boldsymbol{b}^{(1)}$	stretch $\boldsymbol{b}^{(2)}$	Egyptian $\boldsymbol{b}^{(3)}$
1	1 			1 		
2	$\frac{1}{\sqrt{2}}\begin{pmatrix}1\\1\end{pmatrix}$ 	$\frac{1}{\sqrt{2}}\begin{pmatrix}-1\\1\end{pmatrix}$ 		$\frac{1}{\sqrt{2}}\begin{pmatrix}1\\1\end{pmatrix}$ 	$\frac{1}{\sqrt{2}}\begin{pmatrix}-1\\1\end{pmatrix}$ 	
3	$\frac{1}{\sqrt{3}}\begin{pmatrix}1\\1\\1\end{pmatrix}$ 	$\frac{1}{\sqrt{3}}\begin{pmatrix}-1\\0\\1\end{pmatrix}$ 	$\frac{1}{\sqrt{6}}\begin{pmatrix}1\\-2\\1\end{pmatrix}$ 	$\frac{1}{\sqrt{3}}\begin{pmatrix}1\\1\\1\end{pmatrix}$ 	$\frac{1}{\sqrt{3}}\begin{pmatrix}-1\\0\\1\end{pmatrix}$ 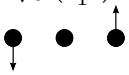	$\frac{1}{\sqrt{6}}\begin{pmatrix}1\\-2\\1\end{pmatrix}$ 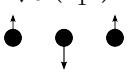

Table 2.2.: Axial and radial eigenmodes $Q_p(t)$ classified by increasing eigenvalues μ_p and corresponding normalised eigenvectors $\boldsymbol{b}^{(p)}$ of linear 1-,2- and 3-ion crystals. The index p labels the eigenmodes, while there exist one per spatial degree of freedom and per ion, accounting to $3N_i$ modes in total. The arrows pointing away from the ions, being the black dots, visualise the crystals' eigenmodes. Their lengths are to relative, but not to absolute scale. [75]

2.2. Ultracold Atoms

2.2.1. Atoms in Optical Dipole Traps

Neutral atoms are conventionally trapped in magneto-optical traps, magnetic traps or optical dipole traps. We will employ a mMOT[1] as cooling pre-stage for a cODT[2], which will be part of the actual hybrid trap.

In the semi-classical oscillator model, the trapping force is an optical dipole force that originates from dispersive interaction of the induced atomic electric dipole moment with the intensity gradient of the laser light [37]. Far-detuned light causes only little absorptive dipole interaction. Thus, the limiting factor of residual photon scattering which heats the atoms is small, and ultralow temperatures on the order of nK can be reached using ODTs [37].

A classical light field $\boldsymbol{E}(r,t)$ of amplitude E_0 induces an atomic dipole moment $\boldsymbol{p}$ along its direction of polarisation which oscillates at the light's frequency ω. The amplitude of the dipole moment is proportional to the field amplitude, $p = \alpha E_0$, where α denotes the complex polarisability [37, 78]. Naturally, the induced dipole moment interacts with the field itself which can be described by the interaction potential, named optical dipole potential [37]:

$$U_\mathrm{dip} = -\frac{1}{2}\langle \boldsymbol{p}\cdot\boldsymbol{E}\rangle = -\frac{1}{2\varepsilon_0 c}\Re(\alpha) I\,. \tag{2.30}$$

Here, the angular brackets represent the time averaging over the fast oscillating terms, the light field intensity is $I = 2\varepsilon_0 c|E_0|^2$, and the factor $\frac{1}{2}$ is due to the dipole moment being an induced, not a permanent one. The in-phase component of the dipole oscillation leads to dispersive interaction, which can be described by the real part of the complex polarisability, $\Re(\alpha)$ [37, 78]. The conservative dipole force appears at places with non-vanishing potential

[1] mirror magneto-optical trap

[2] crossed optical dipole trap

gradient [37]:

$$\boldsymbol{F}_{\mathrm{dip}}(\boldsymbol{r}) = -\nabla U_{\mathrm{dip}}(\boldsymbol{r}) = \frac{1}{2\varepsilon_0 c}\Re(\alpha)\,\nabla I(\boldsymbol{r})\,. \tag{2.31}$$

Consequently, the optical dipole force is proportional to the gradient of the light intensity. In contrast, absorptive interaction can be ascribed to the out-of-phase component of the dipole oscillation being described by the imaginary part of the complex polarisability, $\Im(\alpha)$ [37, 78]. This causes absorption of power from the radiation field, later emitted as dipole radiation [37]:

$$P_{\mathrm{abs}}(\boldsymbol{r}) = \langle \dot{\boldsymbol{p}} \cdot \boldsymbol{E} \rangle = \frac{\omega}{\varepsilon_0 c}\Im(\alpha) I(\boldsymbol{r})\,. \tag{2.32}$$

The photon scattering rate is then given by $\Gamma_{\mathrm{scat}}(\boldsymbol{r}) = \frac{P_{\mathrm{abs}}(\boldsymbol{r})}{\hbar\omega}$.

From the description of an atom in a classical Lorentz oscillator model, the complex polarisability α can be derived [23, 37, 78]. In general, values for the polarisability can be experimentally determined or also calculated, provided the transition matrix elements of the involved dipole transitions are known. In the prominent case of large detunings and negligible saturation, the dipole potential can be expressed as [37]:

$$U_{\mathrm{dip}}(\boldsymbol{r}) = \frac{3\pi c^2}{2\omega_0^3}\frac{\Gamma}{\Delta} I(\boldsymbol{r})\,. \tag{2.33}$$

It's worth noticing, that the potential energy of atoms in the optical dipole potential is proportional to the laser intensity $I(\boldsymbol{r})$. The detuning, $\Delta := \omega - \omega_0$, of the laser frequency ω from the closest atomic transition frequency ω_0 is an important property. Since we employ a red-detuned ODT, i.e. $\Delta < 0$, the minima of the optical dipole potential are at positions with maximum intensity. That's were the atoms are dragged to.

Since both the optical dipole potential and the absorbed and re-emitted power are proportional to the spatially varying intensity $I(\boldsymbol{r})$, one has to be aware of the spatial intensity distribution of the dipole laser beams. For the characterisation of a focussed Gaussian beam four parameters have to be known: (i) its intensity or power P, (ii) its minimum $\frac{1}{e^2}$-radius named waist size, w_0, which corresponds to the focal point, (iii) its wavelength λ, and (iv) its direction of propagation, assumed to be along the optical axis z. From this, the Rayleigh length z_{R}, and the change of the beam radius $w(z)$ along the trap axis z for which the intensity has dropped to $\frac{1}{e^2}$ of its maximum value can be determined [37, 78]:

$$z_{\mathrm{R}} = \frac{\pi w_0^2}{\lambda}\,, \qquad\qquad w(z) = w_0\sqrt{1 + \left(\frac{z}{z_{\mathrm{R}}}\right)^2}\,. \tag{2.34}$$

Since an ideal focussed Gaussian beam is invariant under rotation around the optical axis z, one radial coordinate $r = \sqrt{x^2 + y^2}$ is introduced. Hence, the intensity distribution of a focussed Gaussian beam is given by [37]:

$$I_{\mathrm{FGB}}(r, z) = \frac{2P}{\pi w^2(z)} \cdot \mathrm{e}^{-2\frac{r^2}{w^2(z)}}\,. \tag{2.35}$$

Consequently, the beam waist w_0 and wavelength λ, or Rayleigh length z_{R} alternatively, determine the $\hat{\boldsymbol{z}}$–$\hat{\boldsymbol{r}}$-anisotropy of the optical dipole potential (2.33). In the first approximation, the optical dipole potential U_{dip} can be assumed to be harmonic in each spatial direction. Usually, the potential in the radial directions is much steeper than in the axial direction, because the Rayleigh length is larger than the beam waist [37], cf. (2.34) keeping in mind that

$w_0 > \lambda$. Moreover, the maximal dipole potential at the centre of an ODT is commonly referred to as trap depth, $\hat{U} = |U_{\mathrm{dip}}(r = 0, z = 0)|$. The trap frequencies can then be expressed as [37]:

$$\omega_r = \sqrt{\frac{4\hat{U}}{m_{\mathrm{a}} w_0^2}}\,, \qquad \text{and} \qquad \omega_z = \sqrt{\frac{4\hat{U}}{m_{\mathrm{a}} z_{\mathrm{R}}^2}}\,, \tag{2.36}$$

in the radial and axial directions, respectively. Here, m_{a} is the mass of the atom.

2.2.2. Fermions vs. Bosons

In the experiment, the primary usage of fermionic ^{6}Li is intended, but in principal the bosonic ^{7}Li isotpe may be used, too. Moreover, one objective is the creation mBECs[1] or dimers of bosonic $^6Li_2$ molecules. Therefore, a brief description of both classes of *identical particles* is enqueued here, mainly based on [55, chap. 9 Multiparticle Systems] and [40, chap. 2]:

In quantum mechanics, the only badge affixed to a particle which can be used for identification, is its *quantum mechanical state*, while "neither individuality nor history can be used for identification" [55]—in contrast to classical physics. The indistinguishability of identical particles occupying the same state is a pillar of quantum statistics that naturally has to be preserved in measurements. This means to guarantee invariance of all expectation values under exchange of identical particles. Therefore, the two-particle exchange operator $\mathcal{E}_{ij}$ has to be norm-conserving and unitary, i.e. $\mathcal{E}_{ij}^2 = \mathbf{1}$, and thus its eigenvalues have to be $\varepsilon = \pm 1$ [40, 55]:

$$\mathcal{E}_{ij}\psi_{ij} := \psi_{ji} = \pm\psi_{ij}\,. \tag{2.37}$$

Here, $\psi_{ij} = \psi(..., i, ..., j, ...)$ is the multiparticle wave function, including the exchanged particels i and j.

Since combinatorially, there are in general multiple non-commutative combinations of permutations equivalent to a single particular permutation[2], i.e. they have a different eigenvalue $\varepsilon = \pm 1$, there have to exist *two classes* of identical particles characterised by their permutational behaviour. According to the *spin-statistics theorem* [55, p. 9.2], fermions with half-integer spin have a totally antisymmetric $(-)$ multiparticle wave function, whereas wave functions of integer-spin particles, bosons, exhibit symmetric permutation behaviour $(+)$. Important to note is that also compound systems behave either fermionic or bosonic, e.g. in interference experiments of large C_{60} molecules or inorganic clusters [80] or in ultracold phases like Bose-Einstein condensates [81].

Consequently, a single state labelled by its quantum numbers can only be occupied by one fermion, which is stated by the Pauli exclusion principle [55]. This results in the well-known fact of different filling of states in case of harmonically trapped fermions and bosons, respectively. The occupation number distribution can mathematically be expressed in the fermionic commutator and bosonic anticommuataor relations of creation and annihilation operators, $\hat{b}^\dagger$ & $\hat{b}$, and $\hat{a}^\dagger$ & $\hat{a}$, respectively [55]. The many-body ground state wave function for N non-interacting fermions is consequently given by:

$$|\Phi_{\mathrm{F}}\rangle = \underbrace{|1\rangle \ldots |1\rangle}_{N\text{times}} |0\rangle \ldots |0\rangle \equiv |\underbrace{1, 1, 1, \ldots, 1}_{N\text{times}}, 0, 0, 0, \ldots\rangle = \prod_{\{i:\, E_i < E_{\mathrm{F}}\}} \hat{b}_i^\dagger\, |0, \ldots, 0\rangle\,. \tag{2.38}$$

Here, the eigenstates of the harmonic oscillator, labelled by the mode index i, have an occupation number of 1 from the ground state to the $(N-1)$-th single-particle excited state with a

[1] molecular Bose-Einstein condensates

[2] A pictoresque group-theoretical description can be found in "Die Tücken des Bilderaufhängens" [79].

corresponding energy E_i. The highest possibly occupied state is at the so-called Fermi energy $E_\mathrm{F} := \mu(T=0,N)$, defined as the chemical potential of N fermions at absolute zero, $T=0$. For an ideal Fermi gas it holds that $E_\mathrm{F} = (6N)^{1/3}\hbar\overline{\omega}$, $\overline{\omega} = (\omega_x\omega_y\omega_z)^{1/3}$ being the geometrical average of the trapping frequencies [82]. Associated with it are the Fermi temperature $T_\mathrm{F} = \frac{E_\mathrm{F}}{k_\mathrm{B}}$, and the Fermi wave vector $k_\mathrm{F} = \hbar^{-1}\sqrt{2mE_\mathrm{F}}$ which constitutes the Fermi surface of a sphere in momentum space. For an ideal Fermi gas in a harmonic trap, the Thomas-Fermi radius gives the density distribution's width at $T=0$, $R_i^0 = \sqrt{2E_\mathrm{F}/m\omega_i^2} = a_\mathrm{ho}(48N)^{1/6}\overline{\omega}/\omega_i$ for all spatial dimensions i [82]. Here, $a_\mathrm{ho} = \sqrt{\hbar/m\overline{\omega}}$ represents the characteristic extension of the harmonic oscillator.

For bosons, energy minimisation favours all particles to coequally occupy the lowest possible single-particle state. Therefore, the ground state wave function of N spinless and non-interacting bosons in state occupation number representation is given by [40, 55]:

$$|\Phi_\mathrm{B}\rangle = |N,0,0,0,\ldots,0\rangle = \frac{1}{\sqrt{N!}}(\hat{a}_0^\dagger)^N\,|0,0,0,\ldots,0\rangle\ , \tag{2.39}$$

where the creation operator $(\hat{a}_0^\dagger)^N$ excites N bosons in the 0-mode, i.e. the single-particle ground state. For non-interacting bosons, it can be shown that the critical temperature for Bose-Einstein consensation, T_BEC, scales as $\propto N^{1/3}$, just as the Fermi energy for harmonically trapped fermions [82]:

$$k_\mathrm{B}T_\mathrm{BEC} \simeq 0.94\hbar\overline{\omega}N^{1/3}\ . \tag{2.40}$$

In an ensemble of particles in thermodynamical equilibrium at temperature T, the change in free energy w.r.t. a change in particle number N is called the chemical potential μ. For fermions, the Fermi-Dirac distribution and for bosons the Bose-Einstein distribution hold, describing the mean occupation number in the i-th state [55]:

$$f_\mathrm{F} = \langle n\rangle_\mathrm{F} = \frac{1}{e^{(E_i-\mu)/k_\mathrm{B}T}+1}\ , \qquad \text{and} \qquad f_\mathrm{B} = \langle n\rangle_\mathrm{B} = \frac{1}{e^{(E_i-\mu)/k_\mathrm{B}T}-1}\ . \tag{2.41}$$

For high particle energies[1] compared to the system's temperature, $E_i \gg k_\mathrm{B}T$, the additional ±1 in both denominators of (2.41) becomes negligible. Thus, in this limit one obtains the classical Boltzmann distribution, independent of the particles' fermionic and bosonic nature [55]:

$$f_\mathrm{cl} = e^{-(E_i-\mu)/k_\mathrm{B}T}\ , \tag{2.42}$$

k_B being the Boltzmann constant. The real-space and momentum space density distributions can be obtained by integrating the occupation number distribution over the continuous $\{\mathbf{k}\}$ or $\{\mathbf{r}\}$ basis, respectively [40]:

$$n(\boldsymbol{r}) = (2\pi\hbar)^{-3}\int \mathrm{d}\boldsymbol{k}\, f(\boldsymbol{r},\boldsymbol{k}) \qquad \text{and} \qquad N = (2\pi\hbar)^{-3}\int \mathrm{d}\boldsymbol{r}\,\mathrm{d}\boldsymbol{k}\, f(\boldsymbol{r},\boldsymbol{k})\ , \tag{2.43}$$

with the density of states $(2\pi\hbar)^{-3}$ per phase space unit volume. Momentum distributions $n_\mathrm{B/F/cl}(\boldsymbol{p})$ can experimentally be determined by the time-of-flight method [83–85]. Recording an atom cloud's shadow projection on an (EM)CCD camera gives one-dimensionally integrated column densities $n_\mathrm{cl}^\mathrm{col}(x,y) = \int \mathrm{d}z\, n_\mathrm{cl}(r)$ which can then get fitted, e.g. by Gaussian functions in the classical case. From this, the particle number N and temperature T of an ultracold atom cloud can be extracted.

[1] and/or small chemical potential μ, which is fulfilled for dilute quantum gases

2.2.3. Elastic Low-Energy Collisions and s-Wave Scattering Length

Scattering properties are important for the characterisation of ultracold atoms. Since most ultracold atom clouds are sufficiently dilute, it's a good approximation to only consider two-body collisions. In the following, the s-wave scattering length of elastic two-body collisions at ultralow temperatures will be explained.

For interaction potentials V_{int} depending on the interparticle distance only, it's convenient to separate out the angular dependence in the one-particle Schrödinger equation, after separating out the centre-of-mass motion and introducing relative spherical coordinates (r, θ, ϕ) [40]:

$$\Big(-\frac{\hbar^2}{2\mu}\nabla^2 + V_{\text{int}}(r)\Big)\psi = E\psi\,, \tag{2.44}$$

where $\mu = \frac{m_1 m_2}{m_1+m_2}$ is the reduced mass. With the common separation of variables into $\psi = r^{-1}R_l(r)Y_l^m(\theta,\phi)$, $R_l(r)$ being the radial wave function and $Y_l^m(\theta,\phi)$ the spherical harmonics, the equation for the radial wave function becomes [55, chap.4.2.4]:

$$\Big(-\partial_r^2 \underbrace{+\frac{l(l+1)}{r^2}}_{\text{centrifugal barrier}} + \frac{2\mu}{\hbar^2}V_{\text{int}}\Big)R_l(r) = \frac{2\mu E}{\hbar^2}\cdot R_l(r)\,. \tag{2.45}$$

The wave function has been expanded into partial waves characterised by their angular momenta l. The repulsive angular momentum-induced centrifugal barrier becomes evident for central forces in general. For large distances r_0 with negligible interaction strengths compared to the collision energy, i.e. $V_{\text{int}}(r_0) \ll E$, an asymptotic wave function can be generated by the superposition of an incoming plane wave, e^{ikz}, from $-z$, and an isotropically outgoing spherical wave, $\frac{e^{ikr}}{r}$, with a relative amplitude $f_k(\theta)$ called the scattering amplitude [40]:

$$\psi(\boldsymbol{r}) \propto e^{ikz} + f_k(\theta)\frac{e^{ikr}}{r}\,. \tag{2.46}$$

The differential cross section is then given by $\frac{d\sigma_k}{d\Omega} = |f_k(\theta)|^2$. According to the spin-statistics theorem [55], total antisymmetry or symmetry of the wave function is demanded for fermions (F) and bosons (B), respectively, yielding:

$$\left(\frac{d\sigma_k}{d\Omega}\right)_{\text{F}} = |f_k(\theta) - f_k(\pi-\theta)|^2\,, \qquad \text{and} \qquad \left(\frac{d\sigma_k}{d\Omega}\right)_{\text{B}} = |f_k(\theta) + f_k(\pi-\theta)|^2\,, \tag{2.47}$$

with $0 \le \theta < \pi/2$. By investigating the asymptotic behaviour of an incident and outgoing wave during scattering at large radial distance $r \gg r_0$, one recognises, that the only effect of an elastic collision on the wave function is adding a phase shift δ_l to each spherical wave [40, 55]. Thus, the scattering amplitude can be expressed in relation to these phase shifts, yielding [55]:

$$\sigma_{k,\text{tot}} = \sum_l \sigma_{k,l} = \frac{4\pi}{k^2}\sum_{l=0}^{\infty}(2l+1)\sin^2(\delta_l)\,, \tag{2.48}$$

where $\delta_l \propto k^{2l+1}$. For low scattering energies, i.e. scatterers' momenta $k \to 0$, only the lowest partial wave contributes to the outgoing wave function—the s-wave with $l = 0$. In this case, the contributions of higher order terms in the series (2.48) drop rapidly. This results in a scattering amplitude that's independent of the outgoing angle, $f_k \approx f_{k,l=0} = \frac{1}{2ik}\left(\mathrm{e}^{2i\delta_0} - 1\right)$.

The s-wave scattering length a is then defined to be [55]:

$$a := -\lim_{k\to 0} \frac{\tan\delta_0}{k} \,. \tag{2.49}$$

In most ultracold atom experiments, the densities are low enough that only two-particle interactions are important, and the temperatures are sufficiently low so that elastic interactions can be described by a single parameter, the s-wave scattering length a.

In the zero-energy limit, i.e. $ka \ll 1$, the total cross section becomes energy independent, $\sigma_{k,\mathrm{tot}} = 4\pi a^2$. Moreover, scattering of two indistinguishable particles may happen via two indistinguishable scattering processes that interfere with each other. Therefore, the total cross sections in the zero-energy limit will add up for indistinguishable bosons, but get subtracted for fermions [40, 55]:

$$\sigma_{k,\,\mathrm{tot,\,B}} = 8\pi a^2 \,, \qquad\qquad \sigma_{k,\,\mathrm{tot,\,F}} = 0 \,. \tag{2.50}$$

Consequently, no scattering of identical fermions occurs at ultralow temperatures and they are thus well described by an ideal Fermi gas [40, 55]. It's worth noticing, that this involves using a spin-mixture for evaporative cooling of fermionic atoms inside an ODT, since it's based on re-thermalisation at lower energies through collisions.

2.3. Atom-Ion Interactions in Hybrid Traps

Assuming an ion and an atom confined in a hybrid trap, the electric field $E(r) = \frac{e}{4\pi\varepsilon_0 r^2}$ of the ionic charge $+e$ induces an atomic dipole moment $p(r_{\mathrm{ia}}) = 4\pi\varepsilon_0\alpha E(r_{\mathrm{ia}})$ into the polarisable atom [1]. Here, $r_{\mathrm{ia}} = |\boldsymbol{r}_{\mathrm{a}} - \boldsymbol{r}_{\mathrm{i}}|$ is the atom-ion separation, e the elementary charge, ε_0 the vacuum permittivity, and the atom's static polarisability is given by α. An attractive force is experienced by the polarised atom that originates from the inhomogeneity of the electric field and drags the atom to the ion. The atom-ion interaction is thus dominated by the coupling between the induced dipole moment and the electric field itself, especially for large atom-ion separations. Hence, the long-range polarisation potential describes the atom-ion interaction for large distances r_{ia} [1, 17]:

$$V_{\mathrm{pol}}(r_{\mathrm{ia}}) = -\frac{1}{2}p(r)E(r) = -\frac{C_4}{r_{\mathrm{ia}}^4} \,. \tag{2.51}$$

Here, $C_4 = \frac{1}{(4\pi\varepsilon_0)^2}\frac{e^2\alpha}{2}$ is the long-range induction coefficient for charge-induced dipole interaction.

In analogy to the purely atomic case in subsec. 2.2.3, a centrifugal barrier, $l(l+1)\hbar^2/(2\mu r_{\mathrm{ia}}^2)$, exists [1], cf. (2.45). This sets both a characteristic length scale $R^* = \sqrt{2\mu C_4/\hbar^2}$, typically on the order of 100 nm [17], and an energy scale $E^* = \hbar^2/(2\mu(R^*)^2) = \hbar^4/(4\mu^2 C_4)$. For the ^{6}Li–^{171}Yb$^+$-mixture, they amount to approximately $E^* \approx 8.6\,k_{\mathrm{B}}\,\mu$K, and $R^* \approx 70$ nm. This characteristic energy E^* is associated with the $s-$wave scattering limit E_s. Thus, this comparatively high E^* indicates that the s-wave scattering regime is reached at far higher temperatures for our atom-ion combination compared to others [1, 17], please cf. sec. A.4.

For small atom-ion distances r_{ia} compared to R^*, V_{pol} doesn't hold anymore. This is obvious, because the long-range polarisation potential V_{pol} doesn't allow collisions to happen. At small distances, e.g. quantum defect theory may be employed or hard core repulsion can be introduced by a modeled potential [16]. Interactions between an atom and ion, $1/r^4$, are much more long-range than the $1/r^6$ van der Waals potential between neutral ground state atoms, but of shorter range than the $1/r^3$ interaction between dipoles [1].

Both, the interaction between the cold atoms and between atoms and ions can be tuned by Feshbach resonances. Feshbach resonances occur for certain magnetic fields when a molecular bound state is resonant with the incoming particles' energy. This allows for tuning the scattering properties of the ultracold Li atoms via the applied magnetic field. With this, investigations on the mBEC–BCS crossover will be possible, just as in [86].

Descriptions on the dynamics and collisions of ions in (ultra)cold atomic gases can be found in, e.g. [87, 88]. In [58] the influence of the micromotion is analysed with regard to sympathetic cooling of ions with ultracold atoms. They show that the heating of ions undergoing micromotion due to elastic atom-ion collisions scales as $\propto m_{\mathrm{a}}^{5/3}/m_{\mathrm{i}}$. Consequently, neutral-ion sympathetic cooling favours a small atom-ion mass ratio $\mathfrak{M}_{\mathrm{ai}} = \frac{m_{\mathrm{a}}}{m_{\mathrm{i}}}$ [17, 58]. The favourable temperature range for sympathetic cooling of Yb^+ with an ultracold Li cloud extends from 10 mK to 10 nK [59].

Elastic atom-ion collisions cause heating of the atom cloud, atom loss, and may cool, but also heat the colliding ion. The latter drastically depends on the mass ratio and collision phase of the ionic micromotion [58], which will become more evident in sec. 5.2.

Inelastic Collisions and Cold Chemical Reactions

Besides elastic collisions, also inelastic collisions and cold chemical reactions occur in hybrid atom-ion systems, causing loss of atoms and ions. In order to determine the scattering properties, i.e. scattering lengths and rates for radiative loss and the ratio of elastic to inelastic collisions, of a hybrid atom-ion system, it's potential energy curves have to be computed precisely. The electronic structure of the Li–Yb-mixture is computed in [59].

Inelastic scattering changes the internal state of the scatterers. Generally, inelastic losses may happen via spontaneous radiative charge transfer [59]:

$$\mathrm{Yb}^+ + \mathrm{Li} \rightarrow \mathrm{Yb} + \mathrm{Li}^+ + h\nu \,, \tag{2.52}$$

where the ion annexes one electron from the atom, and radiative association forming charged molecules:

$$\mathrm{Yb}^+ + \mathrm{Li} \rightarrow (\mathrm{LiYb})^+(\nu, l) + h\nu \,. \tag{2.53}$$

In our case, molecule formation is unwanted, but it might be studied using stimulated photoassociation:

$$\mathrm{Yb}^+ + \mathrm{Li} + h\nu' \rightarrow (\mathrm{LiYb})^+(\nu', l') \,. \tag{2.54}$$

Here, a laser with frequency ν unites the ion and atom into an excited molecular ion, $(\mathrm{LiYb})^+$.

As pointed out in [59], the main source of radiative loss is radiative association with a rate that is two orders of magnitude larger than for radiative charge transfer. Moreover, unwanted inelastic collisions, radiative charge transfer and radiative association are estimated to be at least three orders of magnitude lower in rate than elastic collisions, between temperatures of 100 nK and 1 mK [59]. As a consequence, radiative losses should not hinder sympathetic cooling of Yb^+ ions with ultracold Li atoms. Moreover, feasible control over cold atom-ion chemistry with Feshbach resonances is predicted [59]. It's important to mention, that Feshbach resonances cannot only be used for tuning the scattering properties of the ultracold atoms, but they also enable to control molecule formation rates and the ratio of elastic to inelastic collision rates [59].

Chapter 3

Hybrid Experiment

This chapter gives an overview of the experimental setup and presents the planned essential experimental steps. The purpose and functionality of the individual experimental parts as well as their intertwining needed for studying ultracold atoms and ions will be described. Details on the optical setups and applications of the considerable laser collection will be presented in chapter 4.

3.1. Overview and Projected Experimental Procedure

An overview of the complete planned experimental setup is given in fig. 3.1 in form of a CAD drawing. Currently, the vacuum system is being baked out.[1]

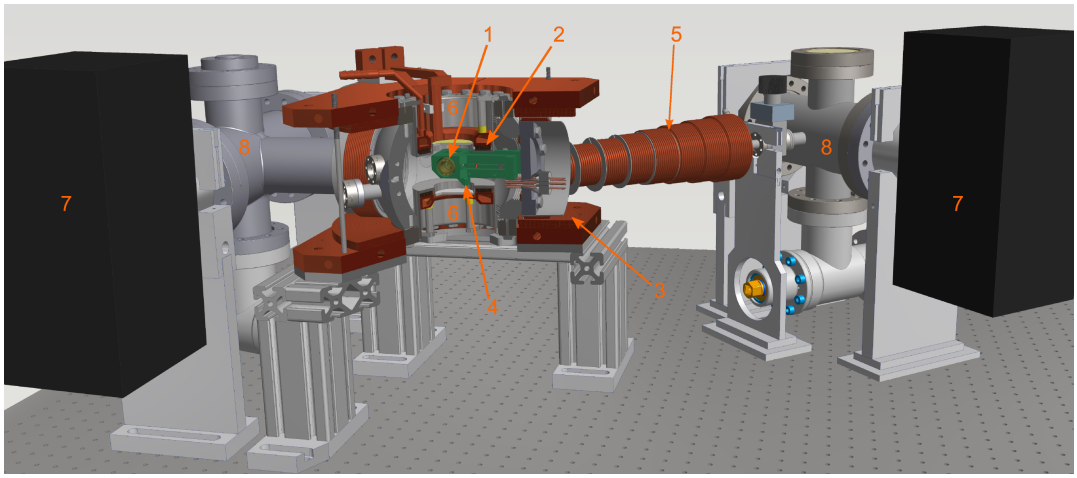

Figure 3.1.: Overview of the complete planned experimental setup as CAD drawing. (1) hybrid trap, (2) Feshbach coils, (3) mMOT coils, (4) mMOT mirror (5) Zeeman slower, (6) inverted viewports, (7) ion pumps, (8) vacuum crosses for flanging additional vacuum pumps and the Li oven.

For the supply of atoms and ions to the centrally displayed (1) hybrid trapping region, two individual ovens are needed. The Yb oven is placed right besides the mount of the ion trap inside the main vacuum chamber and filled with a material sample of ytterbium with natural isotope abundance. Isotope selection happens via in situ two-colour photoionisation inside the (1, dark green) ion trap, cf. sec. 4.3. In contrast, the Li oven is connected to a vacuum flange of the right (8) vacuum cross. Each of the vacuum crosses has an (7) ion pump flanged to it. An additional titanium sublimation pump will be flanged to the left (8) vacuum cross. Both crosses have a valve attached for connecting a turbomolecular pump which is used to

[1] Detailed descriptions on the trap and vacuum design will be presented in the dissertation [89] of Jannis Joger, who also designed the Rb–Yb^+ precursor experiment [90].

pre-pump the system during bake-out. On the right-hand side in fig. 3.1, lithium atoms enter the (5) Zeeman slower from the right (8) vacuum cross. A (greyish blue) rotatable atom beam blocker is attached to the oven-side of the Zeeman slower. It's controllable via the experimental control programme MCP and also manually via the black screw on top. Moreover, there is a (4) mMOT whose two (3) coils are wrapped around the outside of the vacuum chamber. Two (2) Feshbach coils are embedded into (6) inverted viewports.

For an illustrative conceptualisation of the *planned experimental procedure* fig. 3.2 can be drawn on, displaying the two experimental planes as horizontal cross-sections inside the main vacuum chamber. In the *lower plane* fig. 3.2 [*left*], the Zeeman slower's Doppler-cooling beam crosses under an angle of 42 °. It enters the Zeeman slower, whose first coil can be spotted in the lower left corner. From here, an isotope selected, pre-cooled and collimated atomic lithium beam gets loaded into the centrally displayed mMOT. One of the two mutually orthogonal red beams is reflected at the (light grey) mirror, and both are retro-reflected externally, thus enabling magneto-optical trapping of the atoms with the help of the MOT coils. Then, sub-Doppler cooling is projected to be performed to cool and shrink the atom cloud, namely grey-molasses cooling [91]. The laser cooling serves as first step towards quantum degeneracy [92].

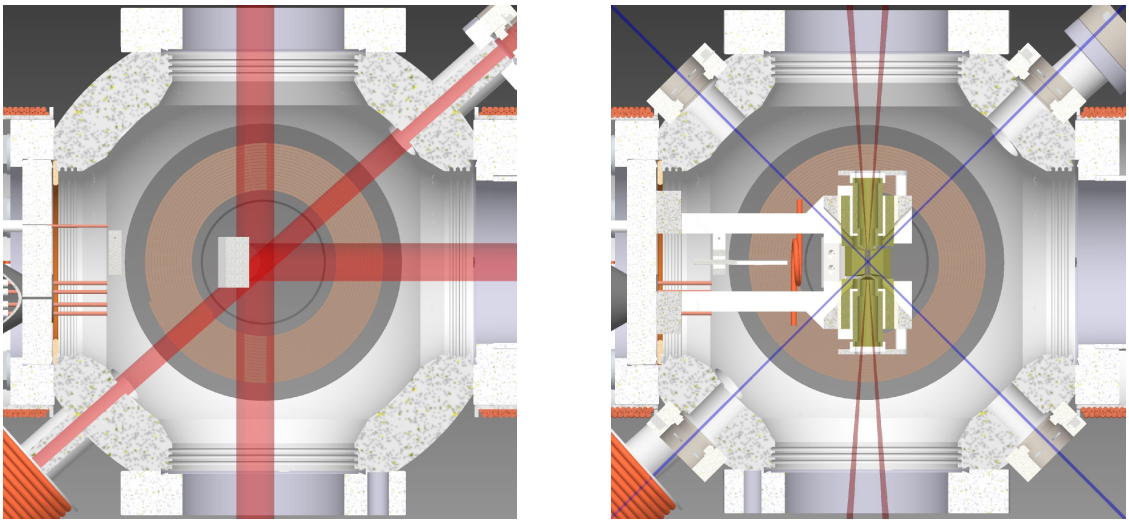

Figure 3.2.: Two experimental planes—horizontal cross-sections of the hybrid trapping experiment's vacuum chamber as CAD drawing. [*left*] *Lower plane* showing the centred mMOT, i.e. its mirror, and its mutually perpendicular laser beams (MOT coils not shown). Moreover, the Doppler-cooling beam under $42\,^\circ$ is displayed, which enters the Zeeman-slower. From here, the mMOT gets loaded with a precooled and collimated atomic lithium beam. [*right*] Upper plane with (green) quadrupole RF ion trap in the centre and the cODT's (red) laser beams crossing under a small angle, which are focussed through holes in the ion trap's endcaps. Two mutually orthogonal (blue) Raman beams which cross under $\pm 45\,^\circ$, will be used for laser cooling, and internal and external state manipulation of the ions. Vertical optical access, i.e. parallel to the experimental planes' normal vectors orientation, is guaranteed by inverted viewports, whose projections are indicated by the inner grey circles. Here, the Feshbach coils can be seen. Additional coils for magnetic transportation are wrapped around both right and left flange. (Colours of hardware and lasers used for highlighting.)

The next step is the transport of the atom cloud into the *upper plane*, fig. 3.2 [*right*]. It happens via magnetic levitation. For this purpose, a pump laser, σ^+ on D1, populates a magnetically trappable state of the lithium atoms. They get pumped into a low-field seeking

state, namely the highest magnetic sub-level of the $2^2S_{1/2}$ hyperfine manifold, cf. $|6\rangle$ in fig. A.2. Consequently, they can be trapped inside the minimum of a magnetic quadrupole field. A change in relative current of the six coils—two MOT, Feshbach and additional transportation coils each—shifts the magnetic field minimum upwards, transporting the atom cloud into the crossed optical dipole trap, (red) in fig. 3.2 [*right*].

The cODT's centre is at the same time the ion trap's one. In this hybrid trap, the atoms get depumped into a spin mixture, containing states $|1\rangle$ and $|2\rangle$, to make them interactive, which is required to evaporatively cool them afterwards. This happens close to a Feshbach resonance, allowing for a wide tuneability of interactions—from a DFG[1], to a mBEC of $^6Li_2$ and BCS[2]-phases—and thus granting a wide field of experimental investigations.

3.1.1. Vacuum System

Residual gas causes unwanted collisions and chemical reactions with the trapped atoms and ions. Since among other things, we are interested in low-energy collisions of single quantum mechanical particles, a pressure as low as 10^{-11} mbar is demanded. As already mentioned, two identical ion pumps[3] are employed to continuously maintain the UHV. The ion pumping mechanisms handle the non-getterable gases such as argon and methane and it's advertised to efficiently pump noble gases, hydrogen, methane, and helium. By igniting the additional titanium sublimation pump[4] from time to time one supports the pumping, because TSPs have an extra high getterable gas pumping speed.

For vacuum compatibility, long endurance and negligible magnetic permeability[5], all metal vacuum components are made of stainless steel 316L. The main vacuum chamber[6] is customised to our needs. Two inverted viewports[7] are embedded for optimal optical access and bringing the Feshbach coils close to the hybrid trap. In fig. 3.1 not all viewports of the main vacuum chamber can be shown due to perspective and the $\frac{1}{4}$-cut, but they can be spotted in the two horizontal cross sections in fig. 3.2. In fact, the main chamber doesn't simply just have the approximated shape of a cheese wheel, but it's also as full of viewports as a Swiss cheese of holes: four viewports for the Raman lasers[8], one viewport for the Zeeman slower beams[9], two viewports for MOT & ODT lasers[10], and one viewport for the MOT[11] alone. Moreover, one viewport is needed on top of the right vacuum cross in fig. 3.1 for observing the Li oven and the atom flow into the Zeeman slower[12].

3.1.2. Computer Experiment Control

For precisely timed experiment control, an ultra-fast signal generator, the so-called *Bertha*, and a C++ based experiment control programme, named MCP[13] are employed [93]. Bertha was locally developed in WA QUANTUM by Dipl.-Ing. Heinz Lenk *et al.*, and refined further by Vidyut Kaushal, M.Sc. for superior sequential timing and supply of analogue and digital control voltages. 32 digital output channels are provided via BNC connections, moreover 24 analogue output channels via an external SMA distribution box. It gets triggered via the

[1] degenerate Fermi gas
[2] Bardeen-Cooper-Schrieffer
[3] Agilent Technologies VacIon Plus 75 StarCell, $p_{\text{start-max}} \leq 5 \times 10^{-2}$ mbar, $p_{\text{min}}^{t\to\infty} < 10^{-11}$ mbar
[4] Agilent Technologies TSP Filament Cartridge
[5] compared to stainless steel type 304
[6] Kimball Physics MCF600-SphSq-F2E4A8 (custom), CF-Flanges: 2× DN100, 4× DN64, 6× DN16
[7] Kurt J. Lesker XTEMP-FT (custom), Fused Silica, Tri-Coating @ $\{370, 670, 935\}$ nm, CF DN100
[8] Vacom VPCF16UVQ-L-VAR370/935/1068-316L, Fused Silica, Tri-Coating @ $\{370, 935, 1068\}$ nm, CF DN16
[9] Hositrad HOVPZ16QVAR-NM, Fused Silica, Coating @ 671 nm, CF DN16
[10] Hositrad HOVPZ64Q-NM, Fused Silica, Tri-Coating @ $\{671, 935, 1068\}$ nm, CF DN16
[11] Hositrad HOBVPZ64-NM, Kodial, Coating @ 671 nm, CF DN63
[12] Hositrad HOVPZ64Q-NM, Fused Silica, no special coating
[13] Master-Control-Program

MCP. The experiment control programme has to a large extend been developped by K. Singer, and further customised and documented by Thomas Ruster in [93, app. A], where detailed descriptions of the MCP and camera software implementation can be found. Implemented into the MCP are classes for triggering and control of various hardware components common in our research group, e.g. EMCCD-cameras, NI-PCI-cards or Bertha. It comes with a customisable graphic user inferface for real-time experimental control and observation. Graphic applications can easily be created in C++ without having to cope with GUI[1] programming.

3.2. Hybrid Trapping

The experiment's centrepiece is the hybrid trapping region. As displayed in its close-up view fig. 3.3, it consists of the (1 & 2, dark green) linear quadrupole RF ion trap and the (3) high-intensity infrared crossed optical dipole trap. Besides these two traps, the preceding Zeeman slower and (5) mirror magneto-optical trap are explained in this section.

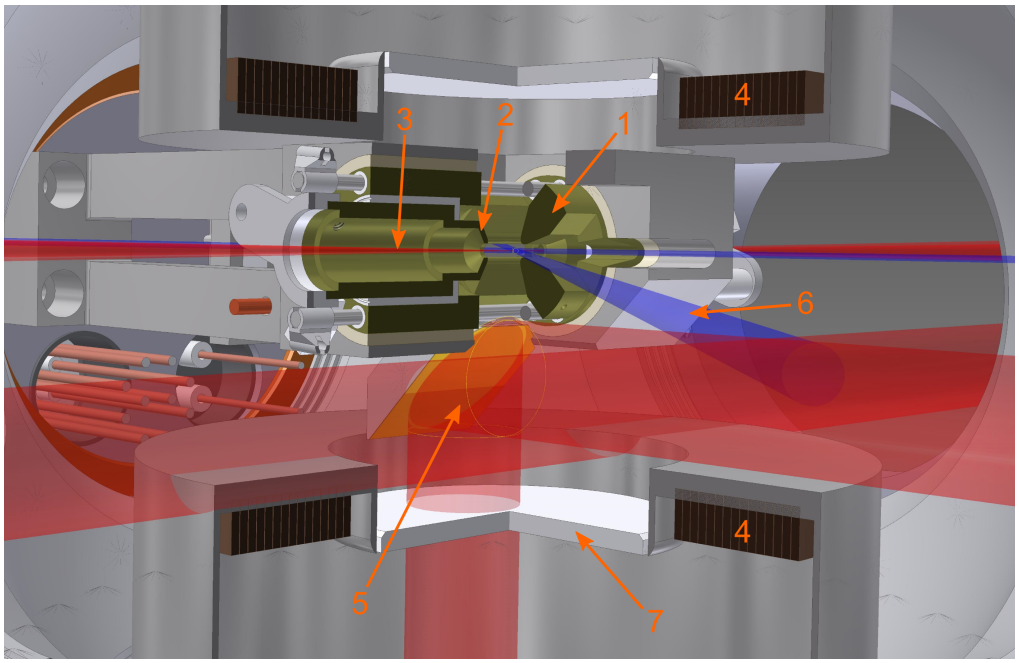

Figure 3.3.: Hybrid trapping region. (green) linear quadrupole radio frequency ion trap with (1) RF blades, and (2) endcaps. (3,red) High-power laser beams of IR optical dipole trap, which are focussed through the ion trap's endcaps. (4) Feshbach coils, (5) mMOT with overlapped molasses laser beams in front of its (yellowisch) mirror, (6,blue) Raman laser beams crossing the trap axis under an angle of $\pm 45°$, respectively, and (7) antireflexion coated windows in inverted viewports, allowing for large apertures. The electric connections to the ion trap are not shown for clarity, but their feedthrough is in the left background. (Colours of hardware and lasers used for highlighting.)

[1] graphical user interface

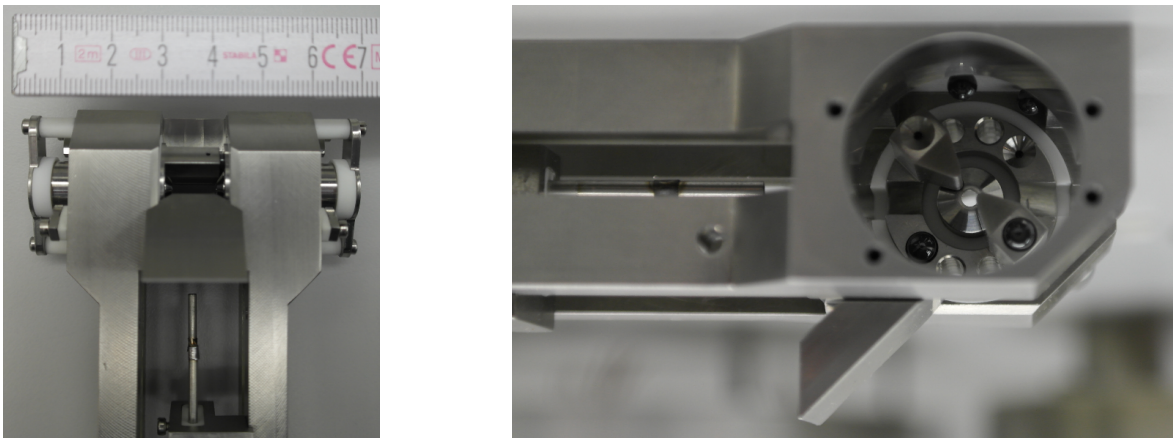

Figure 3.4.: Photographs of the hybrid trapping region. [*left*] Bottom view. [*right*] Lateral view with only half the ion trap built into its mount for a better view. Light shines trough the endcap's centred apperture. Next to it one can spot two of four trap blades with a hyperbolic cross-section. The mount for the mMOT's mirror is attached below the ion trap. The pictures were taken upside-down to prevent the mount from touching the underlaid mat.

3.2.1. Ion Trap

The ion trap is a macroscopic linear quadrupole radio frequency trap and its geometry is depicted in fig. 3.5: [*upper*] showing an axially centred radial cross-section of, and [*lower*] a lateral view onto the ion trap. The RF voltages, $\tilde{U}$ in (2.1), are mutually applied to two opposite (light grey) blades w.r.t. the neighbouring ones. Close to the trap axis, which is radially centered in [*upper*] and pointing straight out of the paper, the blades approximate a hyperbolic profile. This is necessary to obtain the desired trapping potential (2.1).

The blade-distance is $2r_0 = 3$ mm and the 2 mm measure indicates the diameter of the axially centred hole in the ion trap endcaps, which serves as aperture for the high-intensity optical dipole trap laser beams. According to (2.3), only a DC voltage is applied to the endcaps, while the endcap-distance ammounts to $2z_0 = 10$ mm. The blade-length is just slightly smaller, namely 9 mm. The whitish wrapping is made of cemarics, which electrically and thermally insulates the trap electrodes from the mount and surrounding, as can be seen in fig. 3.3 and fig. 3.4.

Additionally, the ion trap is equipped with slits for the Raman laser beams, which are tilted by $\pm 45°$, w.r.t. the trap axis, respectively. In fig. 3.5, they appear as cutouts in [*lower*], best seen in the ceramics, while their concave aperture is most noticeable in [*upper*].

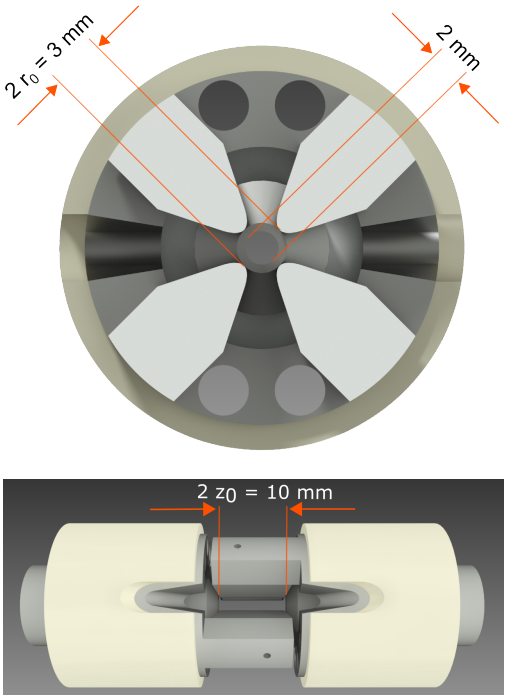

Figure 3.5.: [*upper*] Axially centred radial cross-section and [*lower*] lateral view of the ion trap. The blade-distance measures $2r_0 = 3\,\text{mm}$, while the endcap-distance is $2z_0 = 10\,\text{mm}$. The axial entrance apertures for ODT laser beams measure 2 mm [*upper*], and the slits for the Raman laser beams are tilted by $\pm 45°$, w.r.t. the trap axis, respectively, [*lower*].

Photoionisation will be performed in situ, necessitating additional access for not only a stream of ytterbium atoms entering horizontally as can be seen in fig. 3.1, but also an ionisation laser. The latter passes vertically through the upper inverted viewport, orthogonal to the trap axis.

Simulations on the voltage characteristics of the ion trap are performed to obtain an estimate of the voltages one has to apply to the RF trap blades and endcaps for achieving a proper q Mathieu parameter and secular frequency. In fig. 3.6 the relations $U_{\mathrm{RF}}(q)$ and $\omega_z(U_{\mathrm{DC}})$ are plotted. [*left*] shows the linear relation between RF ion blade voltage and the Mathieu parameter q, which is determined by (2.5) and plotted for three typical values of the RF trap driving frequency Ω. Note the quadratic dependence on the latter. Assuming the static Mathieu parameter to vanish, i.e. $a = 0$, the radial secular trap frequencies ω_r (2.17) at the points marked in red are given by approximately: a) 222 kHz, b) 444 kHz, c) 555 kHz, d) 1.111 MHz, e) 1.111 MHz, and f) 2.221 MHz. In fig. 3.6 [*right*], the axial secular trap frequency ω_z exhibits a square root relation to the endcap voltage U_{DC}. To account for the geometry of the endcap electrodes, (2.16) gets modified with a constant parameter κ, which will have to be determined experimentally for the real ion trap. It can be estimated to be roughly $\kappa \approx 0.27$, resulting in $\omega_z = \sqrt{\frac{2\kappa Q U_{\mathrm{DC}}}{m_{\mathrm{i}} z_0^2}} \approx 2\pi \cdot 17.58\sqrt{U_{\mathrm{DC}}}\,\mathrm{kHz\,V^{-1/2}}$.

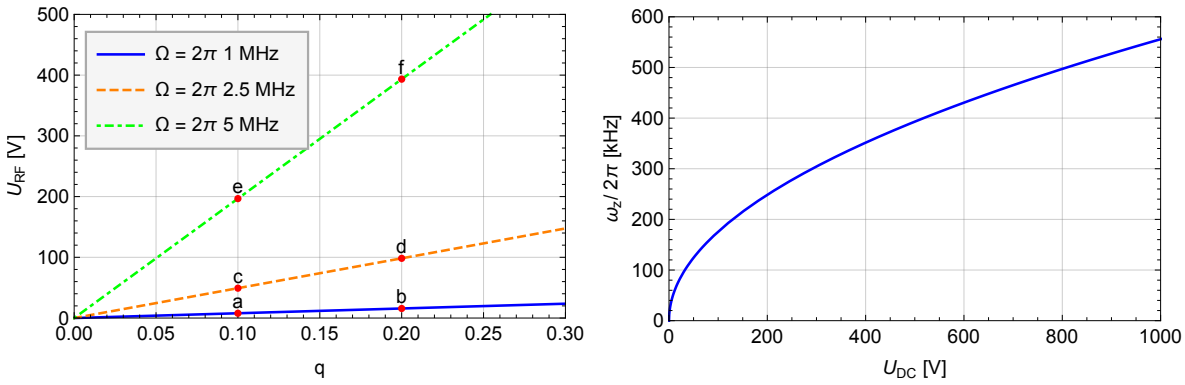

Figure 3.6.: Influence of voltages applied to ion trap blades and endcaps. [*left*] RF ion blade voltage U_{RF} in relation to the Mathieu parameter $q \equiv q_\rho$. The linear relation is determined by (2.5) and plotted for three typical values of the trap driving frequency Ω, following a quadratic dependence. Assuming $a = 0$, the radial secular trap frequencies ω_r at the points marked in red are given by approximately: a) 222 kHz, b) 444 kHz, c) 555 kHz, d) 1.111 MHz, e) 1.111 MHz, and f) 2.221 MHz. [*right*] Axial secular trap frequency ω_z in relation to the endcap voltage U_{DC}, obeying a square root relation in accordance with (2.16).

3.2.2. Zeeman Slower

The work on the Zeeman slower has mainly been done by Henning Fürst, who adapted the design from the group of Selim Jochim at University of Heidelberg [94]. At the time of writing, it is still under construction.[1] The main reasons for implementing a Zeeman slower are the enhancement of the experimental repetition rate, and the benefits of a preslowed and collimated atomic beam. With the help of it, the mMOT can be loaded much faster and more precisely, i.e. without unnecessarily spilling atoms onto the surrounding vacuum components. The increase in experimental repetition rates is beneficial, because data acquisition in atomic physics requires obtaining statistics—and in particular, the atomic part of the hybrid experi-

[1] Detailed descriptions on the Zeeman slower will be presented in Henning Fürst's dissertation [95].

ment takes way longer for preparation than the ionic part. For ions, experimental repetition rates are on the order of 50 Hz, whereas for atoms it's 0.01 . . . 1 Hz.

The Zeeman slower's objective is thus to cool an atomic beam, coming from the atomic oven, from thermal velocities on the order of a few hundred meters per second and a comparatively broad Boltzmann velocity distribution, to an exit speed of a few dozen meters per second with a narrow spread.

Its working principle is to Doppler-cool atoms by a partial compensation of the velocity dependent shift in atomic resonance with the help of the Zeeman effect. For this, a red-detuned cooling laser is required, which slows the counter-propagating atoms of certain velocity classes by Doppler cooling, which will be explained in sec. 4.4. The B-field inside the slower will be generated by surrounding coils, as depicted in the CAD inset of fig. 3.7 [*upper*]. The magnetic field strength and gradient are designed in such a way that the atoms cooling transition remains resonant throughout the deceleration process. The atomic Zeeman shifts' spatial change compensates the decreasing Doppler-shift, $\delta_{\mathrm{D}} = -kv_{\mathrm{a}}$, of slower and slower atoms as they propagate along the slower towards the mMOT. The (red dashed) ideal B-field configuration for deceleration is drawn for the purpose of comparing it to the (dark red) simulated realistic magnetic field configuration shown in fig. 3.7 [*upper*].

The resulting realistic lithium atoms' phase portrait inside the Zeeman slower is displayed in fig. 3.7 [*lower*]. A trade-off between capture, and also exit velocity, and the slower's length has to be made. Due to its finite length of roughly 40.9 cm, the first coil on the oven side has to generate a larger B-field compared to the other coils in order to approximate the square root dependence better. It simply has no overlap to another field of an adjacent coil on the oven side. For the sake of the B-field's axial square root dependence, the second coil has to generate a comparatively smaller field to compensate the first one's excess field. The following fields show a nearly linear decrease,

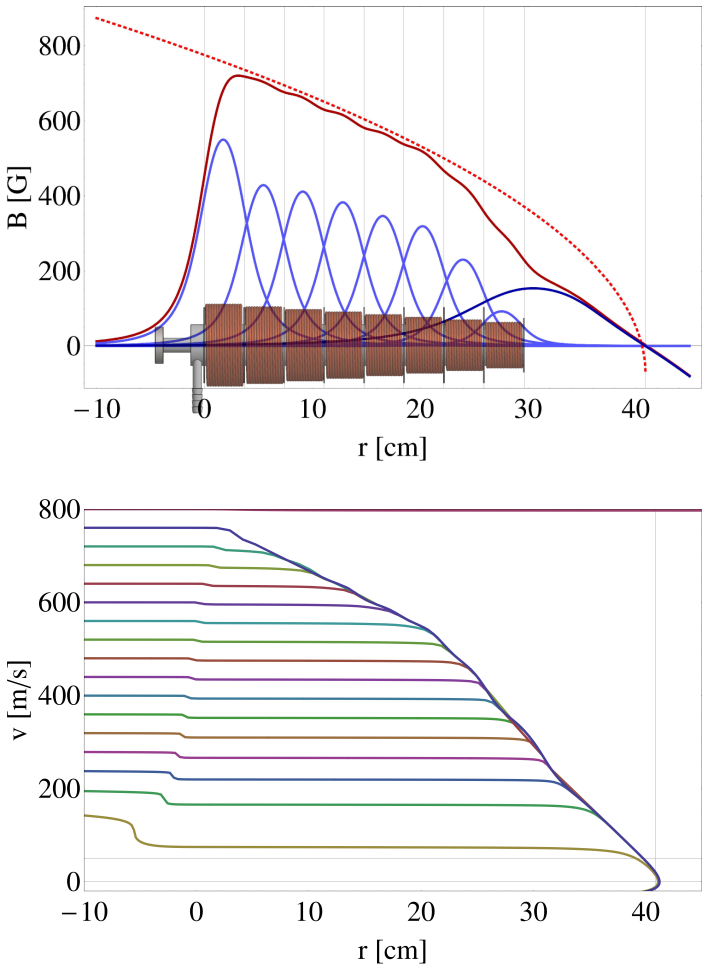

Figure 3.7.: Simulation of the Zeeman slower's B-field configuration and phase portrait. [*upper*] Simulation of the Zeeman slower's magnetic field configuration: (red dashed) ideal square root like behaviour to decelerate all desired velocity classes, (blue) magnetic fields emerging from the individual coils wound around the concave vacuum tube, and (dark blue) the big MOT coil, bridging the magnetic fields between Zeeman slower and trapping region; (dark red) resulting accumulated B field. [*lower*] Phase portrait for different velocity classes of ^{6}Li atoms passing the Zeeman slower. Atoms at initial velocities up to 760 m s^{-1} get focussed in phase space at the mMOT's centre, corresponding to $r \approx 40.9$ cm.

since a square root is linear to first approximation. On the other hand, the last two coils are smaller, since the mMOT's B-field is superimposed, which is the rightmost and darker blue curve in fig. 3.7 [*upper*]. Furthermore, the steepness of the (dark red) sum-field has to be restricted, because otherwise atoms would be resonant for only a too short time at the slower's end. This would lead to an insufficiency of scattered Doppler-cooling photons.

In the simulation, the number of windings gets varied in a certain range around its optimum to account for imperfections in the building process, especially the coil winding, and check for still proper functionality. Thus, the winding numbers of the individual coils are still flexible. The roundish coil wire's outer diameter is 1.1 mm, and the numbers of windings from oven to experimental side are planned to be 430, 320, 305, 280, 250, 230, 160, and 60. A constant current of 6.4 A through all coils is projected. Maybe, the two or three last coils on the experimental side will be driven separately, since they might need to be switched off fast. The reason for this is the mandatory provision of degeneracy of the atoms' fine structure's magnetic sub-levels, i.e. no Zeeman effect, for grey-molasses inside the mMOT.

It's worth noticing, that the lithium's slowing inside the Zeeman slower is isotope selective, since on the one hand, the Doppler shift is different for the isotopes, and on the other hand, the relative isotope shift of the D2 cooling transition is large compared to the laser linewidth. Also note that the lithium source is isotope enriched though, and has an isotopic purity of ^{6}Li of 95 %, cf. tab. A.1.

3.2.3. Mirror MOT

The mMOT to be implemented is displayed in the lower experimental plane in fig. 3.2 [*left*], as well as in fig. 3.3. It requires a magnetic quadrupole field and six laser beams with properly chosen σ^+ and σ^- polarisation w.r.t. their direction of propagation to create the cooling light for the 3-D MOT [6, 7, 96, 97]. The magnetic quadrupole field is generated by two huge coils in anti-Helmholtz configuration, resulting in a field-free trap centre, and a constant gradient in each spatial direction of maximally $\nabla B_\mathrm{z} = 2\nabla B_\mathrm{rad} \approx 50\,\frac{\mathrm{Gauß}}{\mathrm{cm}}$. Since the MOT coils are outside the vacuum chamber and thus relatively far away from the mMOT, they have to generate high magnetic fields. This is achieved through a large product of number of windings and coil current, $N \cdot I$, resulting in the need of large coils, cf. fig. 3.1. The MOT coils have $N = 98$ windings and are planned to generate magnetic field gradients of $\nabla B_\mathrm{z} = 2\nabla B_\mathrm{rad} \approx 36.8\,\frac{\mathrm{Gauß}}{\mathrm{cm}}$ when powered with $I = 38\,\mathrm{A}$. This in turn facilitates to bridge the B-fields from the Zeeman slower, as shown in fig. 3.7 [*upper*].

The constant magnetic field gradients are accompanied by a linear spatial dependence of the magnetic sub-levels' Zeeman shifts of the lithium atoms. Together with the lasers' polarisations, used to pump between these magnetic sub-levels, this leads to magneto-optical trapping in the overlapping region—just in front of the MOT's mirror. This region is tagged in the CAD drawing of the hybrid trap fig. 3.3.

By conventional Doppler-cooling, the minimally achievable temperature of the atom cloud in the MOT is theoretically limited to the Doppler-temperature, $T_\mathrm{D} = \frac{\hbar\Gamma}{2k_\mathrm{B}}$. It is basically determined by the linewidth Γ of the cooling transition. For the D1 transition used for cooling, the Doppler cooling limit amounts to $T_\mathrm{D} \approx 141\ \mu\mathrm{K}$, cf. tab. A.3. However, the hyperfine structure splitting of lithium is not resolved in the $2\,^2\mathrm{P}_{3/2}$ state, which results in an artificial broadening of the cooling transition and thus higher minimal achievable temperatures on the order of 500 μK [94]. To reach lower temperatures and increase the phase-space density before the atoms get transferred to the ODT, a sub-Doppler cooling scheme will be employed, namely grey-molasses cooling. As explained in [91], the trick is to artificially create a narrow fluorescence line to cool to lower temperatures. This narrow-band transition is created by a strong coupling laser, also called cooling laser, which then jointly acts with a second laser, a

repumper. Grey-molasses cooling is the reason for the need of the D1 laser, described in sec. 4.8. With the help of it, the Li atom cloud's temperature can be lowered to $T = 40.5(0.1)\,\mu$K [91]. One advantage is, that the shrinked cloud can be transferred more easily into the ODT, since the mirror has to be bypassed during atomic transport and it has to fit between the ion trap blades, cf. fig. 3.3 and fig. 3.4.

It's important to note, that for the grey-molasses cooling scheme, the magnetic hyperfine sub-levels have to be degenerate [91], i.e. the atoms mustn't sense any magnetic field. Thus, in order to prevent the cooled atomic cloud from expanding and gravitationally falling downwards, both the MOT and Feshbach coils have to get switched off rapidly.

3.2.4. High-Intensity IR Crossed Optical Dipole Trap

As described in sec. 3.1, the lithium atoms will get magnetically levitated into the cODT, forming the atomic part of the hybrid trap. The basic underlying theory is explained in subsec. 2.2.1. In order to be far enough red-detuned from any electronic transition of lithium, the wavelength of the used laser is in the IR, with $\lambda = 1064\,$nm. Due to the small interaction strength between the atoms and the light field, a high-power laser has to be employed. It's a 200 W ytterbium fibre laser[1] and will not be described in detail in this thesis, since its installation has not yet begun.

The calculated intensity profile of the crossed optical dipole trap is shown in fig. 3.8, plotted inside the measures of the ion trap. Two Gaussian beams (2.35) cross under an angle of approximately $5.7\,^\circ$ and the resulting intensity distribution is normalised to a single beam. Idealised, there is no interference of the two beams, since the fibre laser's coherence length is only on the order of 3 cm. Additionally, one can choose perpendicular polarisations of the crossing beams to reduce unwanted interference effects even more. This is essential for the shape and homogeneity of the atom cloud.

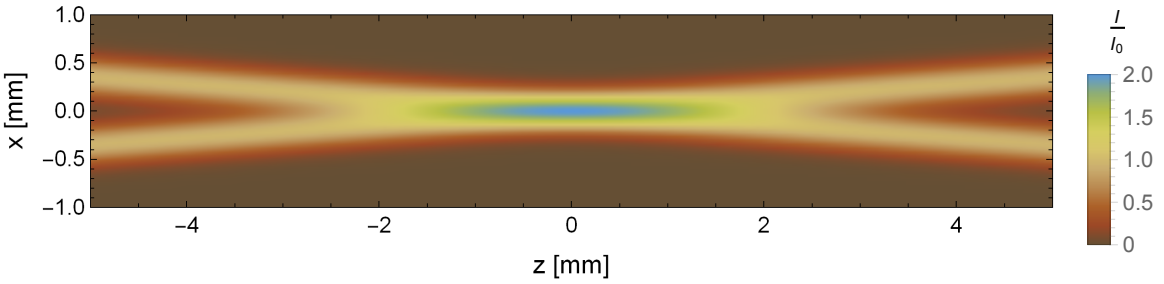

Figure 3.8.: Cross-section of the cODT's laser intensity in the x–z plane. The intensity I is normalised to the maximal intensity of a single of the two focussed Gaussian beams, I_0, which are crossed under an angle of approximately $5.7\,^\circ$. According to (2.33), the atoms' trapping potential is proportional to it. The atoms will form an elongated cigar-shaped cloud with a density profile that matches the inner blue shape, but smaller, cf. fig. 3.9 and text.

The beam profiles' spot sizes of the fibre laser are assumed to be $w(30\text{ cm}) = 3.7\,$mm, 30 cm away from the centre of the cODT, cf. (2.34). Thus, the beams' Rayleigh length is $z_\mathrm{R} = \frac{w_0^2\pi}{\lambda} \approx 2.2\,$mm due to focusing, resulting in a beam waist of approximately $w_0 = 27\,\mu$m in the trap centre.

According to (2.33) and (2.35), the trap depth of the cODT has a linear relation to the total laser power P, as displayed in fig. 3.9 [*left*]. For the maximal laser power of 200 W, the trap

[1] IPG Laser, YLR-200-LP-WC Ytterbium Fiber Laser LP, 200 W, water cooled, with guide laser.

depth has its maximum of approximately 16.6 mK. It's an approximately harmonic trapping potential with degenerate transverse trap frequencies $f_r = f_x = f_y$ in the radial directions x and y. In fig. 3.9 [*right*], one notes the square root relation to the laser power P, cf. (2.36). The axial trap frequency f_z is much smaller, leading to looser confinement along the optical axis z. Mathematically, this is expressed in the trap anisotropy parameter, which amounts to $\alpha = (\frac{\omega_z}{\omega_r})^2 \approx \frac{1}{201}$ for the cODT, ω's being the corresponding angular frequencies.

Since the trapping potential is harmonic in each spatial direction, the two transverse modes are degenerate, and the trap anisotropy parameter is tiny, the atoms arrange in a cigar-shaped cloud which is elongated along the optical axis z, cf. fig. 3.10.

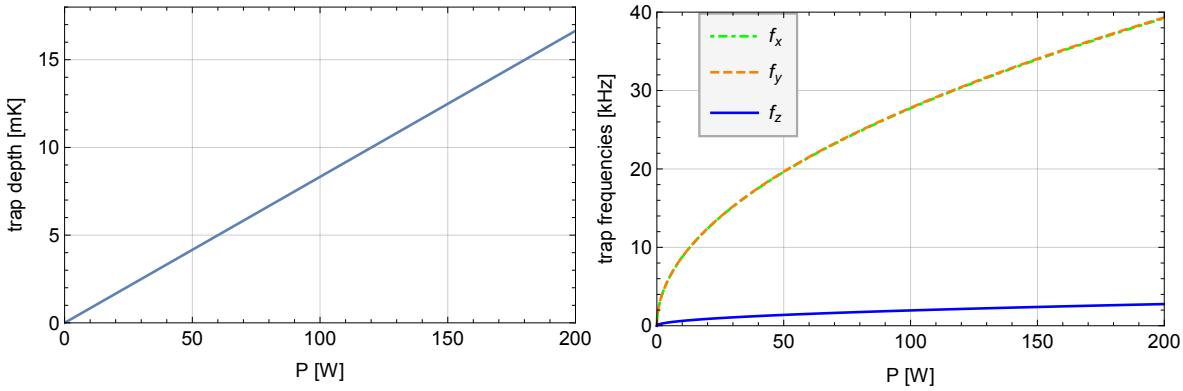

Figure 3.9.: Trap depth and frequencies of the cODT as a function of the laser power. [*left*] The trap depth shows a linear relation to the laser power that forms the cODT. For the maximal laser power of 200 W, the trap depth has its maximum of approximately 16.6 mK. [*right*] All trap frequencies obey a square root relation. The transverse trap frequencies f_x and f_y are degenerate to f_{rad} and the trap anisotropy parameter amounts to $\alpha = (\frac{\omega_z}{\omega_r})^2 \approx \frac{1}{201}$. This results in an elongated cigar-shaped atom cloud.

Depumping the atoms into a spin mixture, $|1\rangle$-$|2\rangle$, makes them interactive and thus enables evaporative cooling into degeneracy. For this, the trapping potential, i.e. trap depth, will get lowered stepwise by attenuating the laser power. In order to tune the interaction with the help of Feshbach resonances, the already mentioned *Feshbach coils* are applied to tune the properties of the spin mixture via B-field magnitude and sign. They support currents of up to $I_{\max} \approx 400\mathrm{A}$, while 14 windings generate magnetic fields of $B_{\max} \approx 850\mathrm{G} = 0.085\mathrm{T}$. For supply of these two coils two identical 6000 W power supplies[1] are employed. For fast switching of the Feshbach and transport coils, the respective power supplies have an additional fast programming option. Furthermore, the Feshbach coils need to get switched rapidly from anti-Helmholtz configuration—used for transportation—to Helmholtz configuration for creating Feshbach resonances. For this purpose, the polarity of one Feschbach coil power supply has to get switched, which will be guaranteed by a fast high-current switching board [95], based on [98].

[1] Delta Elektronika SM 15-400 (P166), $I_{\max} = 400\,\mathrm{A}$, $U_{\max} = 15\,\mathrm{V}$, http://www.delta-elektronika.nl/en/products/sm6000-series.html. For transport coils: SM 30-200 (P167), $I_{\max} = 200\,\mathrm{A}$, $U_{\max} = 30\,\mathrm{V}$, and for MOT coils: SM 45-70 D, $I_{\max} = 70\,\mathrm{A}$, $U_{\max} = 45\,\mathrm{V}$, http://www.delta-elektronika.nl/en/products/sm3000-series.html

3.2.5. Detectors

The most important detector in our experiment is an *EMCCD*[1] *camera*[2]. It has a high tunable gain, high detection speed and unprecedented quantum efficiency. Moreover, a photomultiplier tube, PMT[3] and a CCD camera[4] are planned to be implemented. The PMT has a photon-counting mode which can be used to determine the ions' fluorescence rates and changes, and thus, e.g. the number of ions in the crystal and cooling rates.

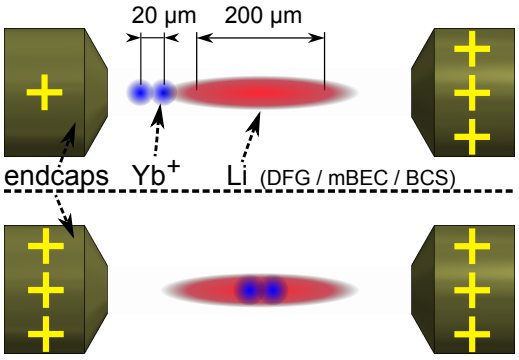

Figure 3.10.: Hybrid trapping scheme. [*upper*] First, ions are trapped off-centre by applying different DC endcap voltages and an atom cloud is trapped in the ODT. [*lower*] Matching endcap voltages shifts the ions and makes them overlap with the cloud.

In our experiment the atoms' absorption and ions' fluorescence imaging beams share a common axis, namely the vertical axis, x. In a first realisation, both are planned to be detected on the same EMCCD. An aspheric lens and dichroic mirror will be employed to decouple the detection light beams from the hybrid trapping region. Along with it comes a subtlety, the different scales of the atomic cloud's extension and the inter-ionic distances. As schematically drawn in fig. 3.10 the extension of the ^{6}Li cloud is on the order of 200 μm, while the inter-ionic distances are on the order of 1 to 20 μm. Therefore, different magnifications M have to be employed. For the atoms it should be $M_\mathrm{a} \approx 1$ and for the ions $M_\mathrm{i} \approx 40$ for the purpose of imaging a number of ions on the order of 10. This is why the (red) transmitted and the (blue) fluorescence light will have to undergo different optical paths outside the vacuum chamber.

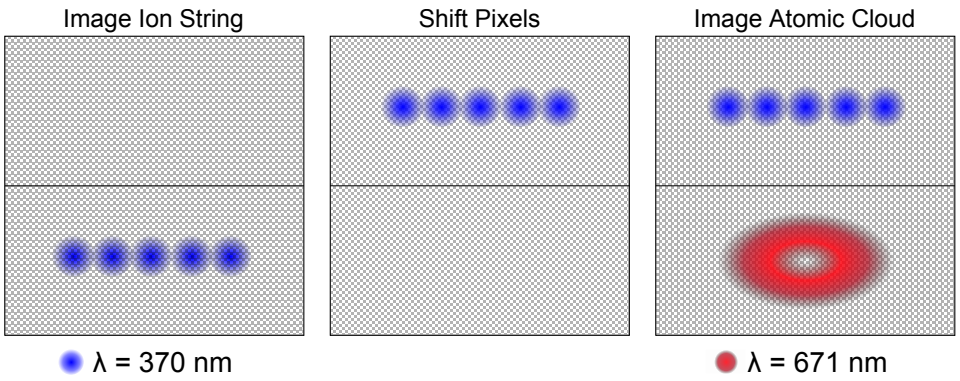

Figure 3.11.: Alternating imaging of ions and atoms on an EMCCD. [*left*] (blue) fluorescence imaging of Yb^+ ion string at 370 nm, [*middle*] shifting of pixels including signal amplification, and [*right*] (red) absorption imaging of Li atom cloud at 671 nm casting a shadow.

The innovative difference between an EMCCD and a usual CCD camera is the unique electron-multiplying (EM) structure that is directly built into the chip. In contrast to a CCD, the clocking of the initial photo-electron charges through the register is performed at higher voltages. This feature has multiple outstanding consequences: Electron-hole pairs are created

[1] electron-multiplying charge-coupled device
[2] Andor Luca-R DL-604M-OEM
[3] Sens-Tech photodetector module P25PC, spectral response range 280 to 630 nm, http://www.sens-tech.com/scientific/fluorescence-spectroscopy/
[4] Allied Vision Technologies Stingray F-033B, https://www.alliedvision.com/en/products/cameras/detail/f-033.html

due to the excess kinetic energy of the initial electrons. An avalanche-like effect makes gains of thousands possible. An interesting characteristic is the linear tunability of this EM gain via the applied voltage. Furthermore, the scan rate is really fast compared to CCDs, but at the same time with little noise. Common high-speed amplifiers require a wide bandwidth resulting in a high noise level. This is suppressed by the on-chip electron multiplication. Last but not least, an EMCCD harnesses the full quantum efficiency of the silicon sensors in contrast to intensifier tubes of ICCDs[1]. Infos taken from [99–102].

The active region of the used EMCCD has an image area of roughly $8 \times 8\,\mathrm{mm}^2$ and consists of 1004 pixels in horizontal times 1002 in vertical direction, respectively. Each one having a pixel size of $8 \times 8\,\mu\mathrm{m}^2$. Its comparatively high readout rate accounts for 13.5 MHz maximum, while having a frame rate of 12.4 fps. First test measurements of the EMCCD's quantum efficiency have confirmed the specifications of 22 % and 25 % at wavelengths of 350 nm and 375 nm, respectively.

[1] intensified charge-coupled devices

Chapter 4

Laser Log

Since the hybrid experiment incorporates two different chemical elements, an extensive laser collection is required for ionisation, cooling, state preparation and detection. The lasers' individual setups, characteristics and experimental functionalities are discussed. First, special attention is paid to the two self-made diode laser systems which have been constructed in the context of this thesis. Next, the self-made optical shutters based on loudspeakers are described as well as AOMs. Subsequently, a detailed account is given of all Yb and then Li related lasers that have been installed to this day.

4.1. Home-Made Laser Systems

The design of the two home-made diode laser systems with a compact grating-stabilisation has undergone several steps in the development: from its origin in [103], through [104] and [90] in the local research group Cold Ions and Experimental Quantum Information[1], to even further adaptions in our group. Besides the hardware's description, the following aims at explaining the control and its benefits over the current I, temperature T, and resonator length L dependence of the laser wavelength:

$$\lambda = \lambda(I, T, L) \,. \tag{4.1}$$

In order to drive the laser diodes, two current controllers have been built up. Additionally, a reliable temperature stabilisation is required for the LDs to operate under reproducable conditions, in particular to lase at a certain tunable wavelength. Furthermore, a Piezo element can be used to tune the length of the external cavity and thus the laser wavelength even more precisely, since the LD's mode selection happens via external cavity stabilisation [78]. The self-made lasers are the one used for the 1st step in isotope-selective photoionisation, described in sec. 4.3, and the so-called re-repumper for ionic ytterbium, explained in sec. 4.6. All the diode lasers' electronics, i.e. twofold current drivers fig. B.2, temperature feedback controls fig. B.3 and piezo transducer triggerings fig. B.4, are integrated into an electronics rack. It's supplied via a connection to a Statron power supply[2].

A CAD drawing of the home-made lasers is shown in fig. 4.1. The lasers are each enclosed in an (5) anti-reflective housing on top of a solid metal block, both made of eloxadized aluminium—not only for height adaption to the optics reference height of 9 cm, but also to increase thermal stability.

The parts relevant for lasing itself are placed on a U-shaped one-piece nickel silver block, which can be used for vertical adjustment via a micrometer screw. Another block mounts the (1) collimation tube with a lens a the LD inside. It's the model Nichia NDV4316[3] for the 1st step of two-colour photoionisation, and the model Thorlabs L637P5[4] for ytterbium

[1] http://quantenbit.de/

[2] Statron 6371.16 with a nominal current of 2 A per output and two times three 9-pin D-sub outputs, both sets of three galvanically isolated.

[3] http://www.nichia.co.jp/specification/products/ld/NDV4316-E.pdf

[4] http://www.thorlabs.de/thorcat/QTN/L637P5-SpecSheet.pdf

re-repumping. All relevant specifications of the installed components can be found in tab. 4.2 or in the referenced data sheets.

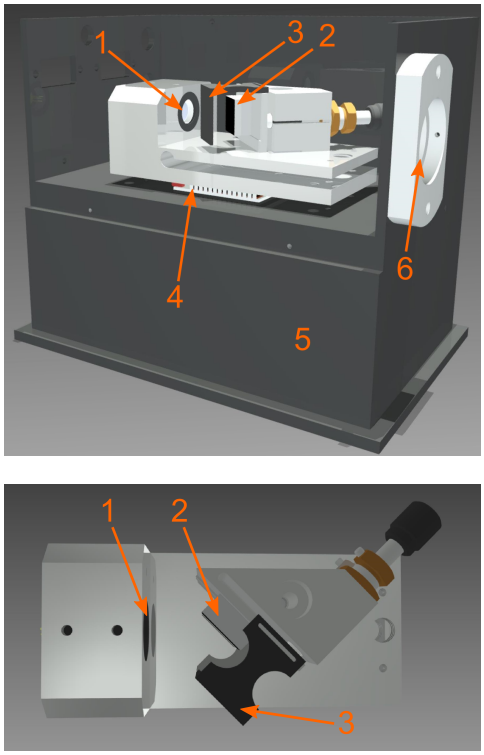

Figure 4.1.: CAD drawings of the grating stabilised diode lasers. [*upper*] Oblique view of opened housing and [*lower*] top view of important components. (1) LD in collimation tube, (2) holographic grating, (3) decoupling mirror, (4) Peltier element, (5) anti-reflective housing with huge thermal mass, and (6) laser aperture with framed mount.

For proper collimation, collimation tubes and especially collimation lenses and their compatibility are optimised. The installed ones have adapted focus length, working distance, numerical aperture and AR-coating, cf. tab. 4.2. The opposite mount is rotatable and a (2) holographic grating and (3) mirror are glued and screwed to it, respectively. The mirror's mount can be translated, and slightly tilted and rotated, because there are multiple threads. Beneath, a (4) Peltier element used for temperature stabilisation can be seen. The laser light leaves the housing through a (6) laser aperture which can be closed by transmission windows.

Littrow Configuration

For mode selection and locking, optical feedback is supplied through an external cavity. It consists of a holographic grating which is placed in Littrow configuration w.r.t. the LD itself, i.e. the 1$^{\text{st}}$ diffraction order is coupled back into the LD [103]. To determine the approximate Littrow configuration angle θ_{L}, the diffraction equation $2a\sin(\theta_{\text{L}}) = n\lambda$ is used. Here, a is the grating slit separation which is the inverse of the grating constant $g = \frac{1}{a}$, and n gives the diffraction order to be fed back. The choice of gratings is made such that θ_{L} is as close to 45° as possible for the outcoupling to work properly, values given in tab. 4.1. Please note that the grating is not placed in the middle of its holder's side, but shifted to its acute angle to get illuminated as well as possible.

This setup diffracts approximately 20 % of the incident light back into the LD[1] for Q-enhancement. For good optical alignment, one can thus lower the LD current stepwise and turn the micrometer screws to seed the diode inside its lasing region better and better. Hitting the LD with its fedback light reduces the threshold current I_{thr} required for population inversion and thus lasing. In doing so, a bright laser spot flashes up. The light which is coupled out via mirror[2] consists of the 0$^{\text{th}}$ diffraction order [103].

Property	Symbol	ionisation @ 398.9 nm	re-repumper @ 638.6 nm
grating constant	$g = \frac{1}{a}$	$3600\,\text{mm}^{-1}$	$2400\,\text{mm}^{-1}$
Littrow angle	θ_{L}	45.9°	50.1°

Table 4.1.: Littrow configuration parameters for the home-made diode lasers. The wavelength and grating constant determine the Littrow configuration angle for optical feedback of the 1$^{\text{st}}$ diffraction order, to be $\theta_{\text{L}} = \arcsin\left(\frac{g\lambda}{2}\right)$.

[1] laser diode

[2] Mirrors are glued to the translatable and slightly rotatable holder with two-component adhesives, just as the grating to its post.

For good optical alignment, properly chosen collimation lenses and tubes have to be employed. Before the grating mount is placed into the optical path, the light gets collimated over a distance of roughly 2 m—across the lab to the wall. This is longer than the length of the beams' optical path on the optical table before it's being coupled into an optical fibre, cf. fig. 4.5. The optimised components of the collimation optics are given in tab. 4.2. Please note that the laser beam leaving the LD is elliptical due to the asymmetry of the diode's frontal lasing area [78]. Here, the semi-major axis of the beam is alligned horizontally by carefully rotating the collimation tube. The two holes above the (1) collimation tube, as indicated in fig. 4.1 [*lower*], are used for fixing its position with plastic screws.

All in all, special care has to be taken in all steps that involve proper illumination of the stabilisation grating and the decoupling mirror: first of all flat and precise glueing of the grating and the mirror, carefull installation and alignment of the diode, decent alignment and fixing of the grating-mounting block and then the mirror mount. For vertical alignment through tilting and bending of the U-shaped block, one micrometer screw and two M2 screws are used. They are screwed into the three most outer holes on the right side in the laser's top view fig. 4.1 [*lower*].

component	ionisation @ 398.9 nm	re-repumper @ 638.6 nm
laser diode	Nichia Violet LD NDV4316 $\lambda_{\text{selected}} = 400$ nm $P_{\text{CW}} = 120$ mW $P_{\text{abs-max}} = 140$ mW $\varnothing = 5.6$ mm, 4-pin socket: Roithner Laser LDS-T-4 $I_{\text{thr}} = 27.9$ mA, $I_{\text{op}} = 98.0$ mA, $V_{\text{op}} = 4.83$ V $\theta_{\parallel} = 9.5°(2)$, $\theta_{\perp} = 19.4°(9)$	Thorlabs L637P5 $\lambda_{\text{typical}} = 637^{+3}_{-7}$ nm $P_{\text{CW}} = 5$ mW $P_{\text{abs-max}} = 7$ mW $\varnothing = 5.6$ mm, 3-pin, C pin code socket: S7060R $I_{\text{thr}} = 15$ mA, $I_{\text{op}} = 20$ mA, $V_{\text{op}} = 2.2$ V $\theta_{\parallel} = 8°(3)$, $\theta_{\perp} = 34°(6)$
collimation tube & aspheric lens	LT110P-A C230TMD-A f = 4.51 mm, NA = 0.55, AR-coated: 350-700 nm	LT230P-B A230TM-A f = 4.51 mm, NA = 0.55, AR-coated: 350-700 nm
stabil. grating	UV Reflective Holographic Grating GH13-36U $g = 3600\,\text{mm}^{-1}$ $(12.7\,\text{mm})^2 \times 6\,\text{mm}$	Visible Reflective Holographic Grating GH13-24V $g = 2400\,\text{mm}^{-1}$ $(12.7\,\text{mm})^2 \times 6\,\text{mm}$
decoupling mirror	Tafelmaier float glass LPF/30 T $R > 99\%$ @ 400 nm, $\varnothing = 15$ mm, 1 mm thick	Tafelmaier float glass HR/11 E, $R > 99\%$ @ 640 nm, $\varnothing = 15$ mm, 1 mm thick
aperture window	WG11050-A AR-coated 1" NBK7 broadband precision window 350–700 nm	WG11050-B AR-coated 1" NBK7 broadband precision window 650–1050 nm

Table 4.2.: Components and their properties of the two home-made diode lasers. All components except for the LD for ionisation, its socket and the coated decoupling mirrors are from Thorlabs.

LD Current Driver and Stabilisation

The circuit diagram of the LDs' current driver is displayed in fig. B.2. It regulates and stabilises the voltage applied to the LD and supplies it with the desired current, since LDs are extremely sensitive to voltage peaks. With the help of a 10 kΩ potentiometer with 10 gears one can set the output current by tuning the input voltage of a ultralow noise precision operational amplifier[1]. The current amplification is then performed by a MOSFET[2]. Static discharge has to be avoided when handling with LDs, hence an antistatic wrist strap has to be worn and protection switches are installed. One switch on the control console directly grounds both output pins of the current driver by shorting them. Another switch at each laser housing shortens the contacts to the LD and should be used for turning the lasers on and off.

LD Temperature Feedback Control

For the principles of electronic feedback control systems and an application to the temperature stabilisation of an ultra-high finesse cavity, please cf. my Bachelor thesis [105]. The temperature controllers' circuit diagram fig. B.3 is appended in Electronics and Circuit Diagrams.

A NTC thermistor[3] serves as temperature sensor, which is made of a semiconductive sintered metal oxide. It's characterised by a comparitively large negative change in resistance when undergoing a temperature change, $\frac{dR}{dT} < 0$. The exponential behaviour of its characteristic curve, $R(T) = R_\mathrm{N} \exp(\frac{E_\mathrm{A}}{k_\mathrm{B}}(\frac{1}{T} - \frac{1}{T_\mathrm{N}}))$, yields precise temperature measurements in a small region, and can be ascribed to the thermal excitation of crystal imperfections, e.g. due to doping. Here, T_N and R_N are the nominal temperature and resistance, respectively, and the activation energy is labelled E_A. Those are material-related properties, and we use a common $R_\mathrm{N} \approx 10\,\mathrm{k\Omega}$ NTC thermistor.

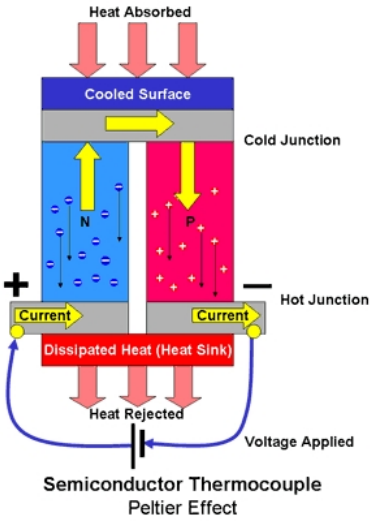

Figure 4.2.: Peltier effect in a semiconductor thermocouple. [106]

The temperature controller[4] itself is advertised to have a linear temperature stability of 0.0009 °C over one hour. It's used to monitor the actual and setpoint temperatures by choice. Moreover, it supports 1.5 A for the supply of a Peltier element[5]. The latter one is employed since no mechanically movable parts nor refrigerants are acceptable for regulating the lasers' temperatures. It's operation is bi-directional, allowing for cooling and heating, but not symmetric, which is explained in the following.

The heat transport results from the current induced thermo-electric Peltier effect, described in [107, chap. 9.6]: A current flux $\boldsymbol{j}$ is always accompanied by a heat flux, proportional to the material-related Peltier coefficient Π, $\boldsymbol{j}_Q = \Pi \boldsymbol{j}$. The working principle is sketched in fig. 4.2. The trick is to alternately stack semiconductive n- and p- doped blocks such that they are electrically in series and thermally parallel, since they exhibit different Peltier coefficients, $\Pi_\mathrm{p} < \Pi_\mathrm{n}$, yielding to different heat fluxes from both sides. Due to the transition of conduction electrons from the p- into the n-doped pins, the heat flux $\Delta j_Q^{\mathrm{p}\to\mathrm{n}} = (\Pi_\mathrm{n} - \Pi_\mathrm{p})|\boldsymbol{j}|$ is divested from the surroundings, thus cooling the Peltier's cold side to T_cool. Physically, this behaviour can be described by the different Fermi energies and filling of states in the differently doped regions [107].

[1] LT1028
[2] FQP27P06
[3] negative temperature coefficient thermal resistor
[4] Wavelength Electronics HTC1500, http://www.teamwavelength.com/downloads/datasheets/htcseries.pdf.
[5] Quick-Cool QC-71-1.4-8.5M

The effective cooling power on the cool side is composed of the Peltier effect $Q_\mathrm{P} \propto T_\mathrm{cool} I$, the Joule heating $Q_\mathrm{J} = \frac{1}{2} R I^2$, and heat transport due to the temperature difference of the two sides $Q_{\Delta T} \propto \Delta T$. It's given by $Q_\mathrm{cool} = Q_\mathrm{P} - Q_\mathrm{J} - Q_{\Delta T}$. The dissipated heat at the hot side is larger than the absorbed heat by twice the Joule heat flux [108]. It's worth noticing, that due to the contributions' different proportionalities regarding I, the cooling capability is not only limited, but even decreases for currents above a critical value. Therefore, even the cold side can heat, if only the current is too high—flipping the Peltier over breaks down the feedback control. This fact and the need for long cycle stability are important for the dimensioning of a Peltier element's cooling capacity [108].

Since the efficiency degrades with high temperature differences between the hot and cold side, good thermal contact is necessary. For this purpose, the Peltier elements are spread with heat-conductive paste, and the laser housings are placed on a solid post with a comparatively huge thermal mass to provide sufficient thermal inertance, as can be seen in fig. 4.1.

LD Piezo Control

As mentioned above, a piezo element[1] is stuck between the micrometer screw and the thin bendable grating mount. It's a piezo-stack actuator. For fine-tuning of the resonator length L and thus change in wavelength, the piezo actuator's control electronics, as shown in fig. B.4, are built up. A versatile IC function generator[2], and an operational amplifier[3] fed by an offset generator form the main part of the piezo control electronics.

Not only *constant position offsets*, resulting from DC offset voltages $U_\mathrm{offset} \approx -10 \ldots 10\,\mathrm{V}$, but also delta voltages can be selected manually. Tuning the delta voltage amplitude and frequency in a range of $U_\Delta \approx 0 \ldots 10\,\mathrm{V}$ and $f_\Delta \approx 5 \ldots 100\,\mathrm{Hz}$, respectively, enables *delta-shaped frequency scans* within a mode-hop-free range. This is required, e.g. to scan the laser wavelength for photoionisation in order to efficiently ionise isotope-selectively. Higher delta voltage frequencies can be set at the expense of a shrinking amplitude, e.g. to 0.53 V at 940 Hz.

Laser Safety and Safety of Home-Made Diode Lasers

Regarding *laser safety*, all reflective and dispersive components on the optical table have been handled with special care—screwing them to the table and blocking of the beam when passing the lasers' optical paths. Due to the variety of wavelengths involved, the laser protection glasses[4] have special custom filters.

The laser housings are totally enclosed and the top cover is screwed to the mount to prevent the lasers from being opened unintendedly. To separate the two lasers from the rest of the laboratory, their breadboard is fenced by cardboard. Additionally, *neutral density filters* serve as beam attenuators in case of too high powers inside the laser housing and during adjustment. They are placed right before the exit windows of the diode lasers. For future purposes, i.e. when the required laser powers are known precisely enough, the NDFs may also be screwed into the apertures' window frame, cf. (6) in fig. 4.1

The employed optical neutral density filters[5] are absorptive and have an anti-reflective coating to prevent detrimental back reflections—for laser diodes as well as the human eye. Their optical density, OD, is defined by the negative logarithm of their transmittance, $\mathcal{T} := \frac{I}{I_0} =: 10^{-OD}$. The decadic logarithm is due to conventions, in contrast to the common Lambert-Beer law, describing the exponential relation between optical depth, τ, and transmittance, $\mathcal{T} = e^{-\tau}$.

[1] Piezomechanik, Piezostacks PSt 150/4/5, http://www.piezomechanik.com/de/produkte/
[2] XR-2206
[3] OP27A/E
[4] Laservision
[5] Here, Thorlabs A-coated absorptive NDFs with optical densities of 1, 2, 3 and 6 (type NE10B-A, NE20B-A, NE30B-A and NE60B-A), but also B-coated ones.

4.2. Control & Manipulation of Laser Light

4.2.1. Optical Shutters

For fast optical switching, homemade mechanical shutters based on "low-cost personal computer loudspeakers" are implemented, as proposed by K. Singer *et al.* in [109]. Five of those optical shutters are built during this thesis and the modified circuit diagram fig. B.1 can be found in app. B. The control electronics are basically a bi-polar power amplifier as output stage, as described in [110, chap. 15], to drive the optical shutter.

It consists of a push-pull final amplifier made of two pairs of complementary transistors that are biased and thus controllable via a TTL[1] signal from the Bertha. Essential for the proper running are identical DC properties of the NPN and PNP transistors, respectively.[2] The bi-directional operation enables a continous current flow keeping the speaker in maximal positive or negative deflection for precise shutting with a little flag attached to it.

For connection of the power supplies, control electronics and loudspeakers[3] 3.5 mm three-pole audio Klinke cables appeared appropriate. To increase the mobility of the shutters in the lab, compact and mobile off-the-shelf power supply units[4] are used. Due to their way of voltage generation, a lot of electronic noise in the AF[5] range, 3 Hz to 30 kHz, is produced which passes on to the control electronics. Here, a passive 2$^{\text{nd}}$ order low-pass filter is integrated to significantly reduce the absolute level of the severely audible audio frequencies in order to reduce the lab's background noise tremendously. Above its cut-off frequency $f_{\text{cut}} = \frac{1}{2\pi\sqrt{LC}}$ the attenuation amounts to approximately -40 dB per frequency decade [110]. For this purpose a huge ferrite-core coil with an inductance of $L = 330\,\mu\text{H}$, and a capacitor of $C = 1000\,\mu\text{F}$, are required, yielding $f_{\text{cut}} \approx 277\,\text{Hz}$.

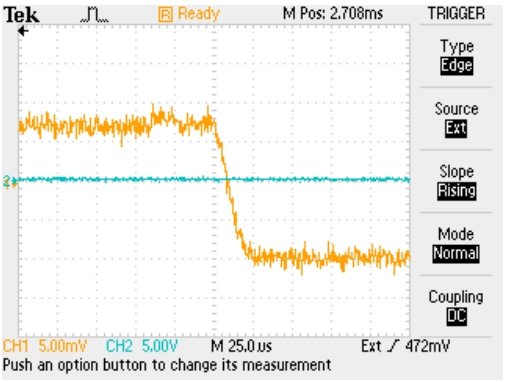

Figure 4.3.: Laser shutting process of the loudspeaker-shutter imaged onto a fast photodiode and recorded on an digital oscilloscope. The photo voltage is shown in (yellow) channel 1. The time-axis scaling is set to 25 μs/DIV. A TTL signal triggered both, the shutter and the recording. The shutting time from total opening to shutting is approximately 25 μs.

This should have no impact on the time scale of shutting, since it only depends on the switching characteristics of the TTL signal and the transistors, and the speakers' lifting speed. To increase the lifting speed and reduce the acoustic level at the same time, the inert speaker membrane is cut out, and a little hole is pierced through the upper stopper membrane on both sides of the actual beam blocker. This minimises the mass of the moving parts and lets the voice coil move more freely. The beam blocker itself is demanded to be as light and as anti-reflective as possible. The ultrathin IC RAM[6] chips of obsolete DDR2 memory modules satisfy these requirements and are thus hot glued to the top of the stopper membrane. Instead, plastic or aluminium foil can be used, too [109].

As can be seen in the recordings of the fast photodiode's[7] voltage on a digital storage oscilloscope[8] in fig. 4.3, the shutting time accounts to approximately 25 μs. It means from totally letting the laser beam pass, to entirely blocking it. This is

[1] transistor-transistor logic
[2] NPN: BD237 and PNP: BD238
[3] VISATON SC 4.7 ND (8Ω), with "clear highrange reproduction" and a frequency response range from 220 to 20000 Hz [111]
[4] goobay NTS 1500 EuP, Rotary Switch Adaptor
[5] audio frequency
[6] random access memory
[7] Thorlabs, PDA10A-EC Si Amplified Detector 200–1100 nm
[8] Tektronix TBS 1022, 25 MHz, 500 MS/s

comparatively fast, according to [109]. A schematic of the optical setup used for testing the loudspeaker-based optical shutters is shown in fig. 4.5, where the fast photodiode is placed in front of the outcoupling fibre coupler on the experiment's end of the optical fibre.

4.2.2. AOMs

Precise laser frequency tunability is an essential tool in modern atomic physics and quantum optics experiments, ranging from the addressing and driving of qubits to all kinds of laser spectroscopy. Since lasers' wavelength availability and fine-tuning [78], as well as affordability and space on optical tables are restricted, AOMs[1] and EOMs[2], are employed to circumvent those issues. Wavelength fine-tuning via AOM and EOM happens through RF electronic signals, which are generated by VCOs[3], which in turn can be switched by the MCP via Bertha.

An AOM's centrepiece is a special crystal that gets excited with the help of piezoelectric transducers [78, 112]. Their precise movement control per radio frequency voltages allows for supersonic oscillations of the crystal modes. Locally, those supersonic acoustic waves lead to a density modulation which imposes a modulation in refractive index. Naturally, this causes heating of the AOM, especially at the RF input side on short time scales, relevant for fast switching processes due to drifts in diffraction angles and intensities. On the opposite AOM side, absorption of acoustic waves causes some heating on longer time scales. The phononic excitation creates an optical diffraction grating with the phonons wavelength Λ as scattering-plane distance, $d = \Lambda$, where incoming light gets Bragg-diffracted [112] according to Bragg's law $n\lambda = 2\Lambda \sin\theta$ [113]. Here, photons gain or loose energy due to scattering with phonons, while the total quasi-momentum is conserved.

Therefore, interference leads to optically separable beams of different diffraction order, i.e. they have a well-defined and deterministically shifted energy of integer multiples of $\Delta E_{\mathrm{AOM}} = nE_{\mathrm{RF}} = n\hbar 2\pi\nu_{\mathrm{RF}}$, in accordance with their diffraction order n. Typical AOM frequencies ν_{RF} are on the order of dozens to several hundreds of MHz. By slightly rotating an aligned AOM, one can change the power diffracted into the different orders, although it's experimentally hard to reach orders higher than 2 or 3 in most cases. For the following schematics of the optical laser setups, the symbol of an AOM has an arrow indicating its direction of positive diffraction orders, rather than the sign of its frequency shift.

A RF power amplifier which has been developped in-house, serves as final stage to drive the AOMs[4] in the experiment. Changing the voltage applied to the VCOs linearly changes their output frequency by approximation. This determines the laser's frequency shift when passing through the AOM. The RF amplitude can be tuned with the help of a modulation input of the AOM driver. With this, the diffraction efficiency and thus laser power can be controlled. Furthermore, the AOM drivers are equipped with a digital input which directly regulates its RF output and consequently enables fast optical switching, e.g. of $+1^{\mathrm{st}}$ order beams. Switching times are typically on the order of 100 ns [112].

4.3. Yb Photoionisation @ 398.9 nm

The first step towards trapping ions is obviously the controlled ionisation process itself. With regard to loading the RF trap with singly ionised atomic ions of the ^{171}Yb isotope, resonantly enhanced isotope-selective photoionisation is planned. A two-colour scheme (399 nm and 369 nm) as described in [114, 115], is being implemented. Advantages compared to one-colour

[1] acousto-optic modulators
[2] electro-optic modulators
[3] voltage-controlled oscillators
[4] *several* types from Gooch & Housego

photoionisation and electron impact ionisation are its high efficiency, its intrinsic isotope-selectivity, and the "nearly deterministic loading of a desired number of Yb ions" [114]. This enables trap loading rates that are several orders of magnitude higher (roughly 3000 times for electron impact ionisation), which in turn reduces the required neutral atom flux drastically, therefore avoiding contamination of the traps and the whole vacuum system [114]. Moreover, no degradation of the trapping potential occurs as in the case of electron bombardment which leads to excess charge in the trap volume.

The isotope-selectivity is due to the two-step procedure being a resonantly enhanced process as shown in fig. 4.4. One benefits from this, since there is no need for isotopically enriched sample material, but already natural isotope abundance suffices. This is cost-effective, since the separation of isotopes is difficile, especially for chemically akin materials such as ytterbium being a metallic rare earth element. In addition, its isotopes have only a small relative mass difference, cf. tab. A.12, complicating meticulous isotopic purification.

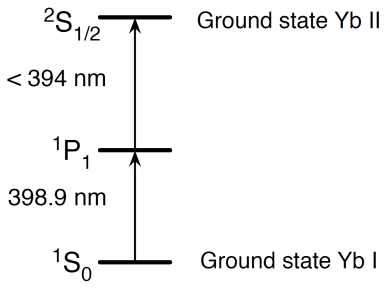

Figure 4.4.: Two-colour ionisation of neutral atomic ytterbium, YbI, via the $^1P_1$ state. Taken from [114].

The essence is to choose one out of many energy levels for first excitation to make the ionisation process isotope-selective. Therefore, a wavelength with inexpensive LDs available is commonly chosen. For this purpose one out of two homebuilt lasers—the one at 398.9 nm—was constructed during this thesis. It's used to drive the optical dipole transition $^1S_0$–$^1P_1$ shown in fig. 4.4. The ionisation continuum can then be reached with a second laser light-field with sufficient energy, i.e. $\lambda < 394$ nm [114]. The lower threshold of the ionisation continuum is at the ionisation energy and corresponds to the ground state $^2S_{1/2}$ of singly ionised Yb^+, also named YbII. Here, it's reasonable to make use of the Yb^+ cooling laser near 370 nm which is needed anyway to drive the $^2S_{1/2}$–$^2P_{1/2}$ transition of YbII, as described in sec. 4.4. Using the cooling laser for the second step entails the neat feature that ions are only created in a region where they can get cooled immediately.

The process can only be isotope-selective if the isotope-shift of the 1st transition of neutral Yb, YbI, can be resolved, requiring resolution of the hyperfine splitting of the ^{171}Yb isotope's $^1P_1$ state. This can be done by reducing Doppler broadening by crossing laser and atomic beam under an angle near 90°. Their entrance slits into the ion trap can be seen in fig. 3.5. Naturally, the isotope shifts of Yb have to be much smaller than the laser's linewidth for the photoionisation to be isotope-selective. Comparing the data given in tab. A.15, one sees that this is obviously true. Additionally, a desired number of ions can be loaded into the trap by simply blocking the ionisation laser, i.e. 1st step in two-colour photoionisation, at the right time.

The ratio between the decay rate of the intermediate $^1P_1$ state into the ground state and the sum of all other decay channels is larger than 10^7 [116]. The $^1P_1$ state has a lifetime of 5.464(5) ns [117] and the saturation intensity of the $^1S_0$–$^1P_1$ transition is $I_{sat} = 60$ mW/cm^2 [97]. Hence, the rather small saturation intensity makes a LD delivering a power on the order of 10 mW more than enough. For its proper lasing, an external cavity stabilisation setup as described in 4.1 is used, which has a small linewidth and is easy to tune with the help of a piezo element, micrometer screw and prevailing temperature. Benefical to picking the desired isotope, is the easy wavelength tuneability of the laser near 398.9 nm to the corresponding $^1S_0$–$^1P_1$ resonance. Peak laser intensities of a Gaussian beam profile in the ionisation region are typically on the order of several W/cm^2, hence a total ionisation laser power on the order of several microwatts is sufficient. [114]

Investigations on the influence of laser detunings on the ionisation process in [114] have

shown, that the exact frequency of the 2nd laser doesn't matter, as long as the ionisation continuum is reached, whereas the 1st laser has to operate resonantly and thus creates a narrow Voigt profile in the ionic resonance fluorescence signal. The natural linewidth of the $^1S_0$–$^1P_1$ transition amounts to $2\pi \cdot 28$ MHz [114]. The ionic fluorescence can be imaged onto a photomultiplier tube in photon counting mode in order to observe the number of trapped ions and also the trap loading rate.

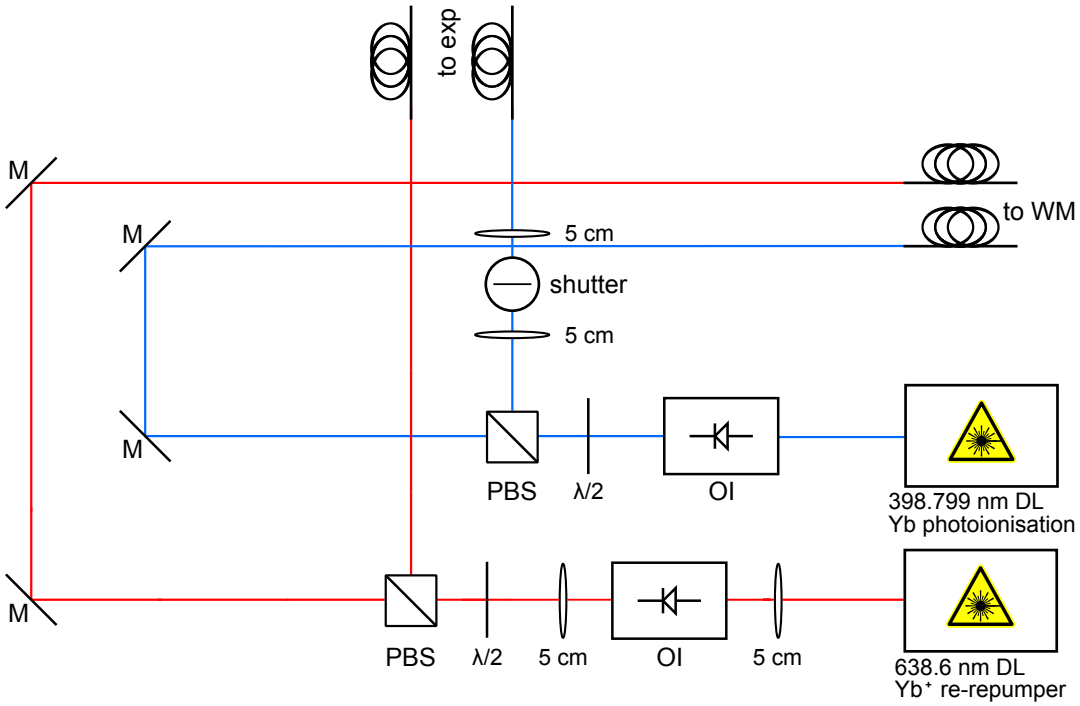

Figure 4.5.: Schematic of the optical setup of the two home-made diode lasers. (blue) Yb photoionisation laser and (red) Yb^+ re-repumper.

In fig. 4.5 a schematic of the optical setup of the two home-made diode lasers is displayed. They are installed on a separate breadboard placed onto the optical table of the vacuum chamber. Connections to the (WM) wavemeter[1] and the future experiment are realised by two optical fibres for each laser.

Both lasers are sent through (OI) optical isolators to prevent detrimental reflections back into the LDs, particularly light of different frequency. Thus, in principle, optical isolators should improve the mode-locking. In case of the (red) Yb^+ re-repumper an intermediate focus is needed to properly inject the elliptical beam into the small aperture of the optical isolator[2], $\varnothing = 2.7$ mm. It is generated by two surrounding identical lenses with a focal length of $f = 5$ cm. The other optical isolator[3] has a larger aperture. Their centre frequencies match the lasers' ones. Next, the relative intensity of each beam in its two paths can be set by a $\lambda/2$ waveplate inside a rotational mount and the subsequent (PBS) polarising beam splitter.

The (M) mirrors are arranged in such a way that the spatial degrees of freedom of the optical paths are adjustable more or less independently. For this, at least two freely translatable, rotatable and tiltable mirrors are required. Moreover, the distances between the last mirrors (or adjustable PBSs) and the corresponding fibre coupler are chosen to be as long as possible. This perceptibly facilitates coupling into the optical fibres with the fibre couplers which are

[1] HighFinesse, Wavelength Meter Ångstrom WS Ultimate 30 and matching mechanical multichannel switch for quasi-simultaneous measurements.

[2] Thorlabs IO-3D-633VLP

[3] Thorlabs IO-5-405-LP

mounted adjustably, too. After its propagation, the laser light emanates from the end of its respective fibre either to the wavemeter or the hybrid experiment.

At a stabilised temperature of 21.5 °C the photoionisation diode laser's wavelength can be tuned by the piezo element to emit laser light of, e.g. $\lambda = 398.79900(1)$ nm. Its mode-hop-free range is 0.00068(1) nm wide, centred around this wavelength. Here, the LD is driven with a current of $I = 63.5$ mA and the decoupled light has a total power of $P = 28.3$ mW. These specifications are determined to be reproducible without further adjustments for a duration of at least four days.

The part of the optical path of the (blue) photoionisation laser going to the experiment can be blocked by an optical shutter, which is based on a loudspeaker and explained in subsec. 4.2.1. Here again, the two surrounding lenses of focal length $f = 5$ cm are used for shrinking the beam by creating an intermediate focus. This is necessary since the speaker's height of stroke is limited. Too big beam diameters simply can't be shutted completely.

4.4. Yb^+ Cooling & Detection @ 369.5 nm

After the 1st step of the two-colour photoionisation, the excited Yb atom's electron needs to reach the ionisation continuum with the help of a second laser—the cooling and detection laser[1]. It's pre-set wavelength is $\lambda = 369.5$ nm and it has an output power of 8 mW. It's original usage is Doppler cooling and detection of $^{171}Yb^+$ ions, but it also accomplishes the ionisation process, enabling in situ photoionisation with immediate Doppler cooling. The energy level scheme of a $^{171}Yb^+$ ion is shown in fig. 4.6, where the wavelengths, lifetimes and the assigned tasks of the involved transitions are specified.

In fig. 4.6 also "Raman" is indicated, i.e. Raman sideband cooling and spin-phonon coupling, for which an additional laser[2] at 369.5 nm is required. It's a tapered amplifier diode laser with frequency doubling done by second harmonics generation (SHG), but has not been built up yet and will thus not be described any further.

A schematic of the DL used for cooling, detection, and also optical pumping is displayed in fig. 4.7. After it's polarisation got purified by two subsequent identical optical isolators[3], a small fraction of the laser light is coupled into an optical cavity for locking the laser. The simplified path to the cavity consists of multiple mirrors, polarising beam splitters, etc. Afterwards, a second pair of rotatable $\lambda/2$-wave plate and PBS allows for sending some of the light to the (WM) wavemeter to determine it's frequency precisely.

[1] TOPTICA Photonics DL pro, Grating Stabilized Tunable Single-Mode Diode Laser, ID-No.: DL pro_018037

[2] TOPTICA Photonics, TA-SHG pro, High Power Frequency-Doubled Tunable Diode Laser System, ID-No.: TA-SHG pro_14143

[3] Thorlabs IO-3-375-GLB

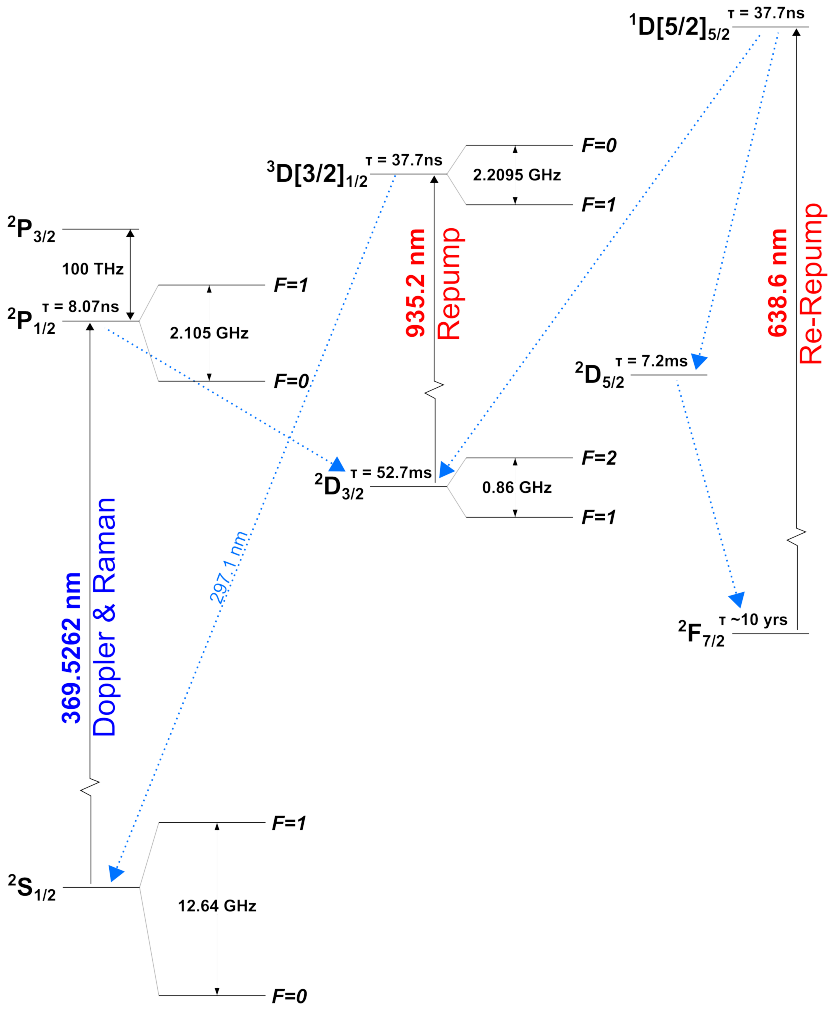

Figure 4.6.: Energy level scheme of $^{171}Yb^+$ with wavelengths of electronic transitions and tasks of the individual lasers indicated. [31, 90, 118–121]

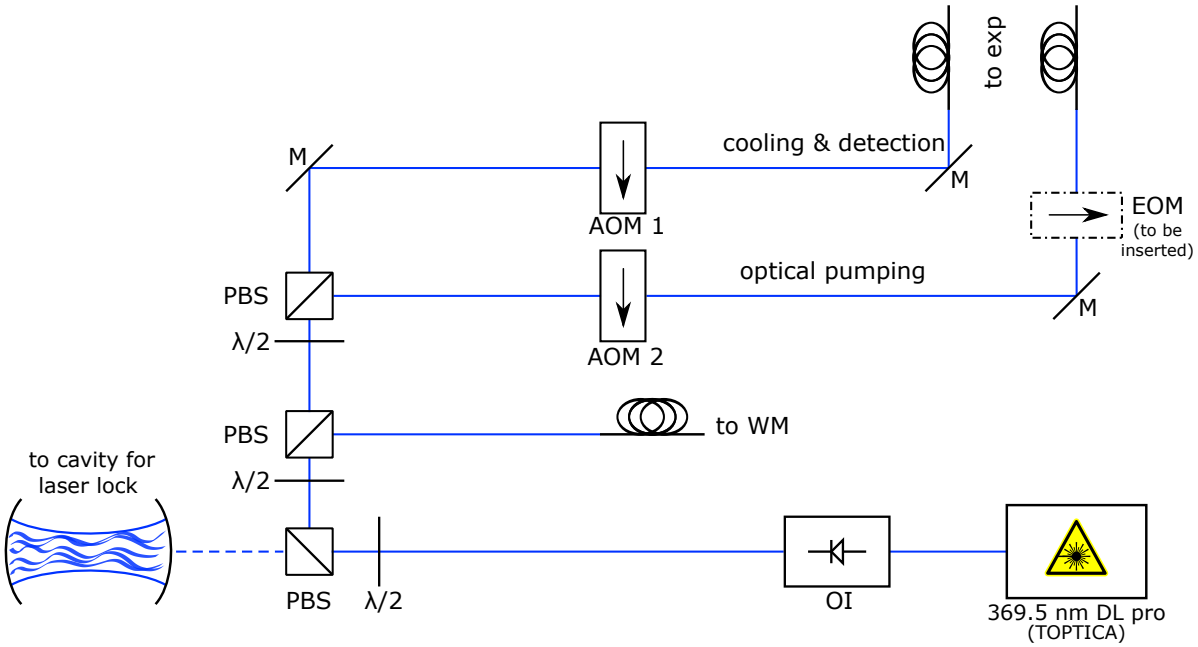

Figure 4.7.: Schematic of the optical setup of the diode laser for cooling, detection and optical pumping of $^{171}Yb^+$.

Most of the power is fed to AOM 1[1], which detunes the beam's frequency to match it with the cooling transition. Both AOMs are adjusted to diffract as much power into the $+1^{\text{st}}$ order as possible. In order to bridge the hyperfine structure splitting of the P-state of 2.1 GHz, an EOM will have to be inserted. This enables optical pumping into the lowest state, $|^2S_{1/2}, F = 0\rangle$, as can be seen in fig. 4.8. Only spontaneous emission from the upper $^2P_{1/2}$ hyperfine state can populate the lowest $^2S_{1/2}$ hyperfine state, because dipole transitions from $F = 0$ to $F' = 0$ are forbidden, as marked with a red cross. This is also important for state detection, since it takes long for the ions to populate the dark state unintentionally.

4.4.1. Doppler Cooling of Yb^+ Ions

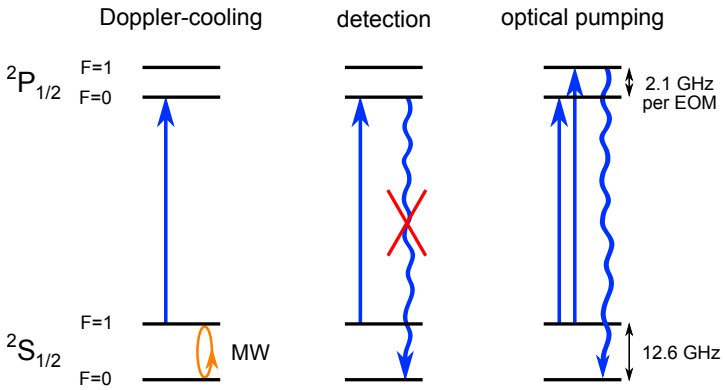

Figure 4.8.: Level schemes and transitions of Doppler-cooling, detection and optical pumping of $^{171}Yb^+$. All absorptive processes are indicated by straight, solid and blue arrows, while spontaneous emission is displayed as oscillating blue arrow. The red cross marks the forbidden transition. The schematic of the optical setup of the diode laser, 370 nm DL pro, used for all these processes is shown in fig. 4.7.

The light for Doppler cooling is slightly red-detuned from the cooling transition, $^2S_{1/2}$–$^2P_{1/2}$, about 10 MHz. This is needed to extract momentum from the ions on average by making them absorb photons of lower energy than they afterwards emit. Since the intake of momentum by absorption is directive, but the release of momentum by spontaneous emission is isotropic, the ions get cooled over multiple excitation and de-excitation cycles. [92, 119, 122]

As can be seen in fig. 4.8, microwaves are to be shot onto the ions to drive Rabi oscillations between the two hyperfine states of the ground state [119]. A signal generator[2] is able to bridge the 12.6 GHz with the help of a subsequent amplifier[3].

The ions' photon scattering rate Γ_{scat} is obtained by solving the optical Bloch equations of the two-level system [23, 78, 123]:

$$\Gamma_{\text{scat}} = \frac{s \cdot \frac{\Gamma}{2}}{1 + s + \left(2\frac{\Delta}{\Gamma}\right)^2} \,. \tag{4.2}$$

It depends on the cooling laser in two ways, namely on its detuning $\Delta := \omega - \omega_0$ from the atomic resonance ω_0, and intensity I —to be more precise, the squared Rabi frequency $\Omega := -\boldsymbol{d}\cdot\boldsymbol{E}_0/\hbar$, where $\boldsymbol{d}$ is the atomic dipole moment and $\boldsymbol{E}_0$ the electric field amplitude of the laser. Thus, the Rabi frequency Ω is a measure for the coupling strength between the light field and the ionic or atomic two-level system. Moreover, the photon scattering rate Γ_{scat} depends on the spontaneous emission rate $\Gamma = \frac{1}{\tau}$ of the cooling transition with lifetime τ. The saturation of

[1] both are of type AOMO 3200-1210 by Gooch & Housego

[2] Rohde & Schwarz SMB 100A Signal Generator 100 kHZ ... 12.75 GHz

[3] Minicircuits ZVA-183-S+, Super Ultra Wideband Amplifier, 700 MHz ... 18 GHz

the transition is expressed by the saturation parameter s and saturation intensity I_{sat} [123]:

$$s := \frac{I}{I_{\text{sat}}} = 2\left(\frac{\Omega}{\Gamma}\right)^2 . \tag{4.3}$$

Here, the saturation intensity, which yields equal population in the lower and upper level of the cooling transition, is given by $I_{\text{sat}} = \frac{c\varepsilon_0\Gamma^2\hbar^2}{4|\hat{e}\cdot\boldsymbol{d}|^2}$, with the unit polarisation vector of the light field $\hat{e}$. The saturation intensity of the cooling transition $^2\text{S}_{1/2}$–$^2\text{P}_{1/2}$ amounts to $I_{\text{sat}} = 0.508\,\text{mW}\,\text{mm}^{-2}$ [124].

Due to the probabilistic nature and isotropy of spontaneous emission, any scattering event can heat the ion. Thus, the width of the cooling transition limits the lowest temperature, which is named Doppler temperature, $T_{\text{D}} = \frac{\hbar\Gamma}{2k_{\text{B}}}$. This minimal temperature can be achieved with a red-detuning of $\Delta = \Gamma/2$ of the cooling laser. For the selected cooling transition of $^{171}\text{Yb}^+$, the Doppler cooling limit amounts to approximately $470\,\mu\text{K}$.

4.4.2. State Detection of Yb^+ Ions with Fluorescence Imaging

The two hyperfine states of the ground state form a two-level system and can be mapped onto an effective spin-$\frac{1}{2}$ system [64]: Say $|^2\text{S}_{1/2}, F = 1\rangle$ is defined to be spin up, $|\uparrow\rangle$, and $|^2\text{S}_{1/2}, F = 0\rangle$ spin down, $|\downarrow\rangle$, then state-selective detection can be interpreted as spin-dependent resonant fluorescence cycle. In order to perform state preparation, optical pumping into the lowest state $|^2\text{S}_{1/2}, F = 0\rangle$ realigns the effective spins of the ions.

As depicted in fig. 4.8, detection of Yb^+ ions will be performed on the closed $^2\text{S}_{1/2}$–$^2\text{P}_{1/2}$ transition. It's a resonant excitation process followed by spontaneous emission, and a little stimulated, too. Thus, the fluorescence light is nearly completely isotropic and only a small fraction can be detected. It's state-selective detection, because there exist a bright $|^2\text{S}_{1/2}, F = 1\rangle = |\uparrow\rangle$ and a dark state $|^2\text{S}_{1/2}, F = 0\rangle = |\downarrow\rangle$. There is no spontaneous emission from one of the two states of the cooling transition into the dark state, cf. fig. 4.8.

To conduct an estimation of the measurement time, one has to estimate the photon scattering rate, the rate of ions decaying into a dark state, the photon collection efficiency of the objective as well as the detector's quantum efficiency. The alongside schematic fig. 4.9 shows the geometrical aperture of the lens, giving the distance to the fluorescent ions, $d \approx 4$ cm, and the radius of the lens, $r = 2.5$ cm. The photon collection efficiency is then defined as the relative solid angle covered by the lens. It's the ratio of the effective lens area to the surface of a sphere with radius d. Assuming small-angle approximation in this rough estimation, it amounts to $\Omega_{\sphericalangle\text{-rel}} \approx \frac{A_{\text{lens}}}{A_{\text{sphere}}} = \frac{\pi r^2}{4\pi d^2} = \frac{6.25}{4\cdot 16} \lesssim 0.1$. The overall efficiency of the detector η, including its quantum efficiency QE are conservatively estimated to be on the order of 30 %. Put together, this means that as few as approximately 3 % of all scattered photons get detected by the EMCCD chip.

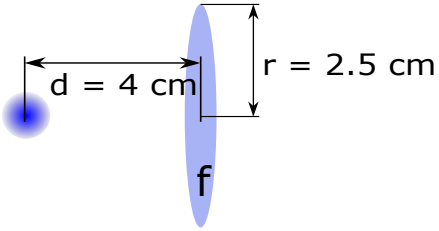

Figure 4.9.: Geometrical aperture of imaging lens. The distance between the objective and the ions is planned to be $d = 4$ cm, while the radius of the lens is $r = 2.5$ cm.

When driving the cooling transition with saturation intensity, $I = I_{\text{sat}}$, and being close enough to the resonant transition, i.e. $\frac{\Delta}{\Gamma} \ll 1$, the photon scattering rate (4.2) simplifies to $\Gamma_{\text{scat}} = \frac{\Gamma}{4}$. This results in an average time for one photon to be scattered of roughly $\tau_{\text{scat}} \approx 32\,\text{ns}$.

Naturally, the ions may turn dark by leaving the fluorescence cycle, but only via off-resonant

excitation to the $^2P_{1/2}(F = 1)$-triplet, cf. fig. 4.8. In this case, the detuning to the detection laser is equal to the hyperfine structure splitting of the $^2P_{1/2}$ state, amounting to $\Delta_{\text{dark}} = \Delta_{\text{HFS}} = 2.1\,\text{GHz}$. This upper level has a spontaneous emission rate of $\Gamma = 20\,\text{MHz}$, thus populating the dark state. According to (4.2), the off-resonant scattering rate is about $\Gamma_{\text{dark}} \approx 227\,\text{Hz}$ which corresponds to an average time before one ion turns dark of $\tau_{\text{dark}} \approx 4.41\,\text{ms}$.

Acting on the assumption of a tolerance threshold of a $\mathfrak{t}_{\text{thr}} = 5\,\%$ chance before an ion turns dark, the maximal number of fluoresced photons is circa $N_{\text{scat}} = \mathfrak{t}_{\text{thr}} \cdot \frac{\tau_{\text{dark}}}{\tau_{\text{scat}}} \lesssim 6890$. This yields maximally $N_{\text{det}} = \eta \cdot \Omega_{\sphericalangle\text{-rel}} \cdot N_{\text{scat}} \lesssim 206$ detected photons. Besides, we should be able to focus the light emitted by one ion onto at least less than 10 pixels of the EMCCD chip, resulting in roughly 20 photons per pixel. Therefore, the measurement time is limited to approximately $t_{\text{meas}} \lesssim 220\,\mu\text{s}$ under the assumed dark-falling tolerance threshold $\mathfrak{t}_{\text{thr}}$. This scenario should entail a proper signal-to-noise ratio. It's worth noticing, that the measurement time can be shortened by lowering the laser intensity below saturation.

Moreover, it is important to note, that there are closed transitions only for vanishing or low magnetic fields, whereas for the fields typically employed for Li, 500…850 G, one of the two levels of the detection transition enters the Paschen-Back regime while the other one is still in the Zeeman regime. Thus, no good common quantum numbers can be found and there is no closed transition at these high magnetic fields that could be used for state-selective detection. Consequently, the Feshbach and MOT coils would have to get switched off for this.

4.5. Yb^+ Repumper @ 935.2 nm

When driving the cooling transition $S_{1/2}$–$P_{1/2}$ of Yb^+ ions for Doppler cooling, a fraction of the population in the P-state decays into a lower-lying D state $^2D_{1/2}$ [114], cf. fig. 4.6. This subtlety of the arrangement of P and D states is a characteristic of rare earth elements which also occurs for alkaline earth metals heavier than Mg. The lifetime of the $^2D_{1/2}$ state is 52.7 ms. To avoid further decay and to recycle the affected ions into the cooling-cycle, a repumper at 935.2 nm is employed which pumps to the hybridised $^3D[3/2]_{1/2}$ state. The repumper is a grating stabilised tunable diode laser[1]. It is pre-set to a wavelength of $\lambda = 935.2$ nm and has a output power of 100 mW. The ions re-enter the cooling transition by emitting UV light of $\lambda = 297.1$ nm.[2]

Nevertheless, the ions may also decay into the even lower-lying $^2F_{1/2}$ state which has a lifetime of roughly 10 years, cf. fig. 4.6. In order to recycle those ions, an additional re-repumper at 638.6 nm is employed. This re-repumper is the second laser that has been built up in the context of this thesis, and it will be shortly described in the following section.

The basic optical setup of the Yb^+ repumper is sketched in fig. 4.10. Here, one can see that a small fraction of the beam can be separated and coupled into an optical glass fibre to be sent to the wavemeter. The main part of the beam's flux passes an AOM[3] which shifts the frequency by +80 MHz, and an EOM which still has to be inserted. The repumper beam will be fed to the ion trap via an optical glass fibre.

[1] TOPTICA PHOTONICS, DL pro Grating Stabilized Tunable Single-Mode Diode Laser, ID-No.: DL pro_018083

[2] For references of given values, please cf. fig. 4.6.

[3] Gooch & Housego AOMO 3080-122 http://goochandhousego.com/product/aomo-3080-122/

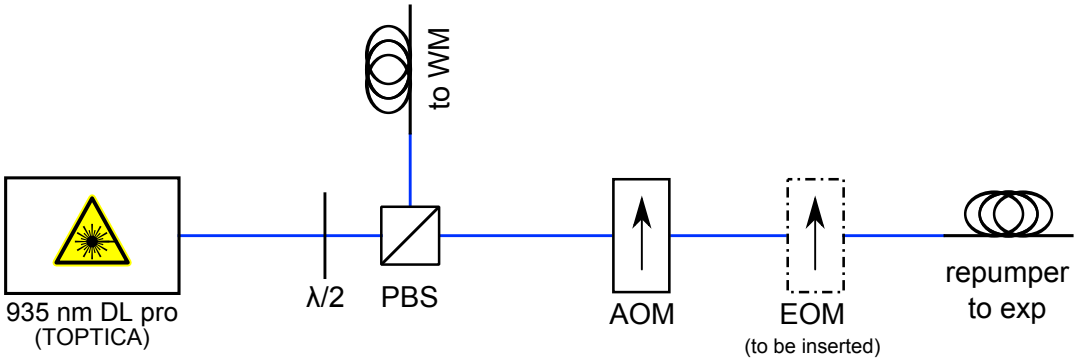

Figure 4.10.: Schematic of the optical setup of the diose laser for repumping $^{171}Yb^+$. A small fraction of the beam can be sent to the wavemeter, while the main part passes an AOM imposing a frequency shift of +80 MHz, and an EOM which still has to be inserted. The repumper beam will be fed to the ion trap via an optical glass fibre.

4.6. Yb^+ Re-Repumper @ 638.6 nm

As already mentioned in the previous section of the Yb^+ repumper, an additional re-repumper is required, which drives the $^2F_{7/2}$–$^1D[5/2]_{5/2}$ transition [121]. As can be seen in the level scheme of $^{171}Yb^+$ fig. 4.6, the upper state may decay back and then the ion has to get re-repumped again—or it falls into the repumping cycle from where it can get recycled into the cooling transition.

A schematic of the re-repumper's optical setup is shown in fig. 4.5, together with the other home-made diode laser that has been built up in the context of this thesis. All information on the laser's components, installation, control and adjustment may be found in sec. 4.1, Home-Made Laser Systems. When driven with the specified operational current of $I = 20\,\mathrm{mA}$, the wavelength can be tuned from 637.5994(1) nm at a temperature of 22 °C, to 639.5610(1) nm at 30 °C. The re-repumper's mode-hop-free range amounts to 0.0022(1) nm at a central wavelength of $\lambda = 638.6032(1)\,\mathrm{nm}$. Consequently, tuning the temperature of the LD within this range enables a much wider range of selectable wavelengths than the fine-tuning of the resonator length via the piezo element. Due to the optimisation of the optical feedback, the lasing threshold current is lowered from 15.5 mA, when free-running, to $I_{\mathrm{thr}} = 13.5\,\mathrm{mA}$.

4.7. Li Cooling & Detection on D2 line

This section and the following one deal with the lasers required for the lithium atom-part of the experiment, except for the high-power IR fibre laser forming the cODT as described in subsec. 3.2.4. Both, the Zeeman slower as described in subsec. 3.2.2 and the mMOT in subsec. 3.2.3, have to be supplied with laser light for Doppler cooling. The basics of Doppler cooling are described in the corresponding section of Yb, subsec. 4.4.1. This is performed on the D2 transition of ^{6}Li, as shown in the level scheme of ^{6}Li fig. 4.11. So does the detection of lithium. It's realised via absorption imaging which will be described in subsec. 4.7.2. Furthermore, the sub-Doppler grey-molasses laser cooling scheme is performed on the D1 line with another laser, described in the next section, sec. 4.8.

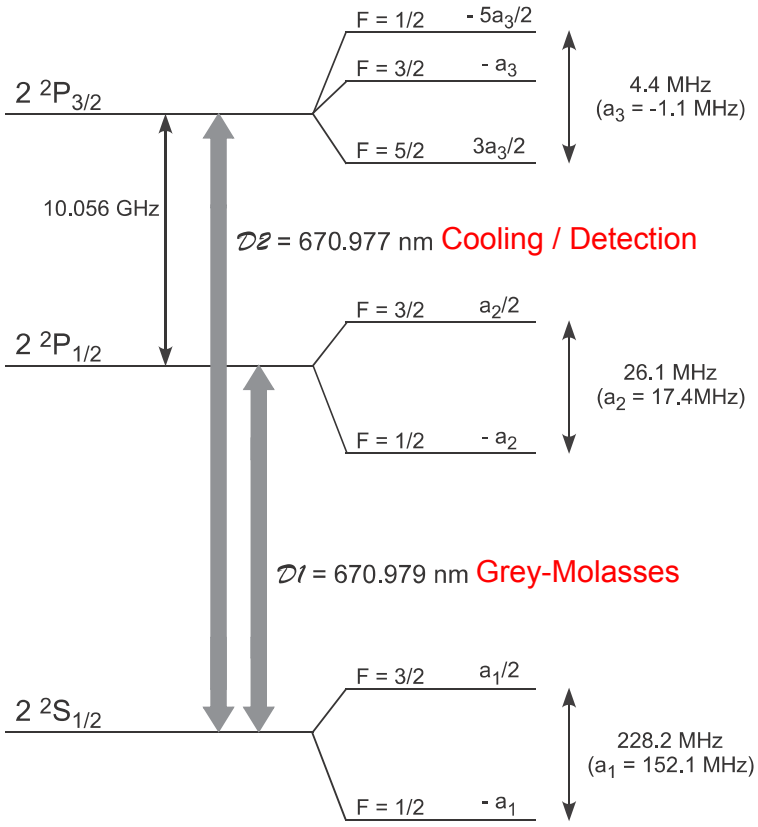

Figure 4.11.: Energy level scheme of ^{6}Li with wavelengths and tasks of the dipole transitions D1 and D2. The D2 transition is used for Doppler cooling in the mMOT and Zeeman slower, while the D1 transition is used for sub-Doppler grey-molasses cooling. The two D-lines are separated by a fine structure splitting of 10.056 GHz, corresponding to a difference in wavelength of approximately 0.002 nm. Energy splittings are not to scale and the diagram originated from [125, 126]. Please note the inconsistency of the values given in the diagram and tables in [125]. Moreover, the values in the NIST Atomic Spectra Database [127] differ, too. This discrepancy will have to get resolved.

4.7.1. Light Supply for Zeeman Slower, mMOT and Imaging

Sufficient laser light near the D2 transition of ^{6}Li for the pre-cooling of the atoms inside the Zeeman slower, the Doppler cooling in the mMOT and the absorption imaging inside the cODT is supplied by a high-power tapered amplifier diode laser[1]. The wavelength of the integrated LD is pre-stabilised to 670.8 nm and the tapered amplifier enables an output power of 500 mW. It's optical setup is sketched in fig. 4.12.

[1] TOPTICA Photonics, TA pro, Amplified Tunable Single-Mode Laser System, ID-No.: TA pro-2V0_13245

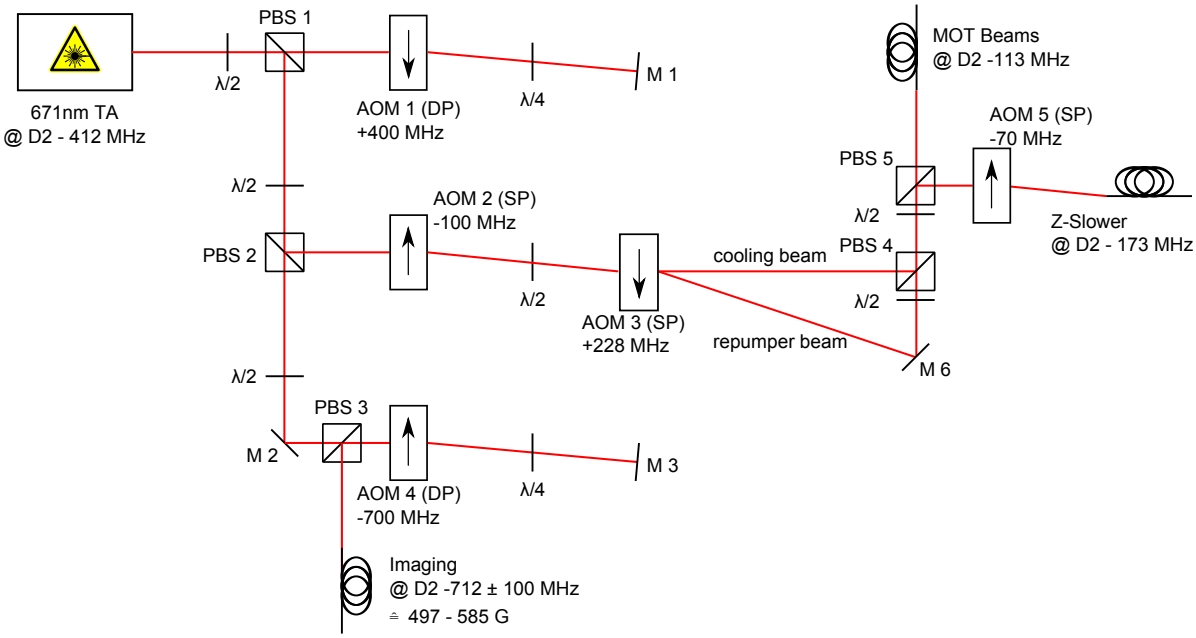

Figure 4.12.: Schematic of the optical setup of the tapered amplifier laser for cooling, detection and repumping of ^{6}Li. It supplies the mMOT and Zeeman slower with appropriately frequency shifted cooling and repumping light near the D2 transition. At the same time, light for absorption imaging of Li is provided.

The TA laser gets locked to the D2 line, detuned by -412 MHz. Using AOM 1 in double-pass configuration gives rise to a frequency shift of +400 MHz and the possibility to modulate this shift by ±50 MHz. With PBS 2 a large amount of the power is sent to AOM 2 in single-pass configuration. Here, the frequency gets shifted down by 100 MHz to match it with the desired frequency for the MOT light. It's detuning to the D2 line amounts to $\delta_{\text{MOT-D2}} = -113$ MHz. Moreover, AOM 2 enables fast switching of all MOT and Zeeman slower laser beams.

AOM 3 diffracts a small desired fraction of the intensity into the 1^{st} order, creating the repumper branch. It's frequency shift of +228 MHz corresponds to the hyperfine splitting of the ground state. On PBS 4 both, the 0^{th} order cooling and $+1^{\text{st}}$ order Bragg-diffracted repumper beam get overlapped again while their polarisations have to be perpendicular. By rotating the next $\lambda/2$-wave plate, the ratio between the intensities split at PBS 5 and sent to the Zeeman slower and the mMOT can be selected. The light for the Zeeman slower needs to be more red-detuned than the light for the MOT, since the atoms' Doppler shift is larger at thermal velocities. Therefore, AOM 5 lowers its frequency by 70 MHz to achieve a detuning of $\delta_{\text{Zeeman-D2}} = -173$ MHz.

The weaker transmission branch of PBS 2 is sent through AOM 4 in double-pass configuration to shift the frequency by (-700 ± 50) MHz. Regarding imaging, the system is able to perform scans in frequency over a range of 200 MHz, two times ±50. This enables detection of the states $|2^2\text{S}_{1/2}, m_J = -1/2, m_I = 1\rangle$ and $|2^2\text{S}_{1/2}, m_J = -1/2, m_I = 0\rangle$ at magnetic fields of 497 to 585 G using the closed transition to the non-resolved magnetic sub-levels of the lowest hyperfine state $|2^2\text{P}_{3/2}, m_J = -3/2\rangle$. Please note, that this is the Paschen-Back regime. Such intense magnetic fields prevent the electron and nuclear spin from flipping, which is stated by selection rules.

4.7.2. Absorption Imaging

The underlying principle of absorption imaging is the recording of the shadow casted by a resonantly illuminated probe. As a consequence of the resonant excitation, the atomic cloud gets heated by the imaging light pulse [128]. Therefore, the ultracold sample gets destroyed during each imaging process which becomes most evident in time-of-flight (TOF) experiments that record the cloud's expansion [83, 85]. This is why a new cloud has to be prepared after an absorption image has been shot.

Aiming at the determination of the atomic cloud's density or absolute particle number, its absorption or transmission, containing similar information, has to be measured. The physical quantity exhibiting this information is the transmittance defined as the ratio of transmitted and incident light intensities $\mathcal{T} := \frac{I}{I_0}$. In accordance with the Lambert-Beer law, it's related to the cloud's optical depth τ through $\mathcal{T} = e^{-\tau}$. In other words, the optical depth which is equal to the optical thickness can be defined as the negative natural logarithm of the light's fraction that is not scattered nor absorbed on its path. From this, information on the particle density n can be retrieved. The reduction of the imaging beam's intensity while passing through the ensemble of cold atoms can macroscopically be described by the Lambert-Beer law [128]:

$$\frac{\mathrm{d}I}{I} = -n(z)\sigma(z, I)\mathrm{d}z \,, \tag{4.4}$$

with the particle density $n(z)$ and the absorption cross section $\sigma(z, I)$ along the coordinate of the imaging axis z. In general, the absorption cross section depends on the imaging beam's intensity which itself depends on the position inside the atomic cloud, $I = I(z)$:

$$\sigma(z, I) = \frac{\sigma_0}{1 + \frac{I(z)}{I_{\mathrm{sat}}} + \left(2\frac{\Delta}{\Gamma}\right)^2} \,. \tag{4.5}$$

This relation corresponds to the one of the photon scattering rate (4.2). Here, σ_0 is the on-resonance absorption cross section and given by:

$$\sigma_0 = \frac{\hbar\omega\Gamma}{2I_{\mathrm{sat}}} \,, \tag{4.6}$$

where Δ is the detuning of the laser field at ω from the closed atomic transition at ω_0, Γ the natural decay rate of the exited state and I_{sat} the saturation intensity. A representative value for the saturation intensity of the D2 transition is $I_{\mathrm{sat}}(\mathrm{D2}) \approx 2.54\,\mathrm{mW\,cm^{-2}}$, cf. tab. A.4.

To measure the actual optical depth with an EMCCD camera, one has to take the background light into account. Thus, in each experimental cycle, three pictures have to be taken. Naturally, one with the atomic cloud present, i.e. the actual absorption image resulting in I_{abs}, a second one as a reference image without atoms, I_{ref}, and a third background image for compensation of straylight without atoms and the imaging laser turned off, I_{dark}. With the help of those three pictures one can determine the transmittance $\mathcal{T}$, which obviously depends on the coordinates perpendicular to the optical axis z, namely x and y. The two-dimensional optical density ρ_{od} is given by it's negative logarithm [39, 40]:

$$\rho_{\mathrm{od}} = -\ln \mathcal{T}(x, y) = -\ln \frac{I_{\mathrm{abs}}(x, y) - I_{\mathrm{dark}}(x, y)}{I_{\mathrm{ref}}(x, y) - I_{\mathrm{dark}}(x, y)} \,. \tag{4.7}$$

By dividing the dark-current corrected absorption image by the reference image, one suppresses the inhomogeneities of the imaging beam, e.g. interference fringes. To prevent the atomic motion from disturbing the imaging process, short exposure times have to be chosen. Typical

pulse durations are shorter than 10 μs [40].

The number of atoms imaged onto one pixel of the EMCCD can be calculated knowing the area of one pixel A and the magnification of the imaging system M [40]:

$$N_{\mathrm{pix}}(x,y) = \frac{A}{\sigma_0 M^2}\rho_{\mathrm{od}}(x,y)\,. \tag{4.8}$$

Here, not only information about the atom number, but also spatial information on the cloud will be extractable, if only the camera resolution is high enough.

4.8. Li Grey-Molasses Cooling on D1 line

D1 grey-molasses cooling is an advanced sub-Doppler laser cooling technique [91, 129]. It's employed to reduce the atom cloud's phase space density, as described in sec. 3.1. In [91] 10^9 ^{6}Li atoms are cooled from 500 μK—achieved by a conventional MOT—to 40 μK. Furthermore, the shrinking of the cloud's extension allows for better and more efficient loading of the crossed optical dipole trap.

Grey-molasses cooling is based on the creation of an artificially narrow atomic resonance by strong atom-photon interaction [91, 129]. High laser intensities cause an AC-Stark effect that shifts and narrows the atomic resonance, which can also be explained by the dressed-atom modell [23, 129]. Thus, not only a strong coupling laser, referred to as cooling laser, but also a repumper are needed. Their transitions and detunings are indicated in the energy level scheme of ^{6}Li, fig. 4.13. Both of them emerge from the same master-slave diode lasers system and are manipulated with acousto-optic modulators. Their absolute detunings to the upper state $|2\,^2\mathrm{P}_{1/2}, \mathrm{F} = 3/2\rangle$ of the D1 line, δ_{cool} and δ_{repump}, respectively, as well as their relative detuning δ_{rel} can be set and tuned this way. In [91] the relative intensities are $I_{\mathrm{repump}} \simeq 0.2 I_{\mathrm{cool}}$. As already mentioned, the magnetic sublevels of the involved hyperfine states have to be degenerate for grey-molasses cooling to work [91, 129].

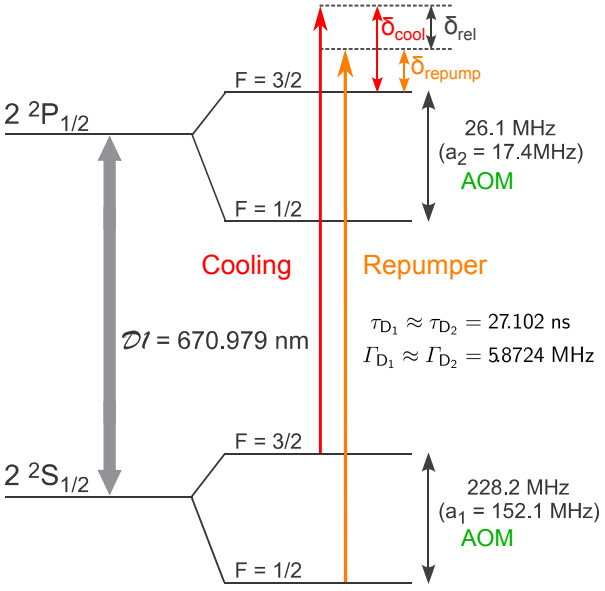

Figure 4.13.: Grey-molasses cooling level scheme of ^{6}Li. (red) Cooling laser and corresponding detuning δ_{cool} to the upper state of the D1 line, (orange) repumper transition with detuning δ_{repump}, and (grey) relative detuning of both lasers δ_{rel}. Energy splittings are not to scale and diagram is in the style of [91], but originated from [125, 126].

A schematic of the master-slave diode lasers system's optical setup for D1 grey-molasses cooling and repumping of ^{6}Li is displayed in fig. 4.14. The AOMs[1] are in a special double-pass configuration, namely two cat's eye (DP) double-pass AOM systems [78, 112]. These cat's eye double-pass configurations will compensate the angular drift of the diffracted 1$^{\mathrm{st}}$ order beam if the AOMs' frequency shift is changed. They consist of two lenses of equal focal length, symmetrically arranged around an AOM in their joint focal point [112]. Passing the

[1] Gooch & Housego AOMO 3100-125 http:// goochandhousego.com/product/aomo-3100-125/

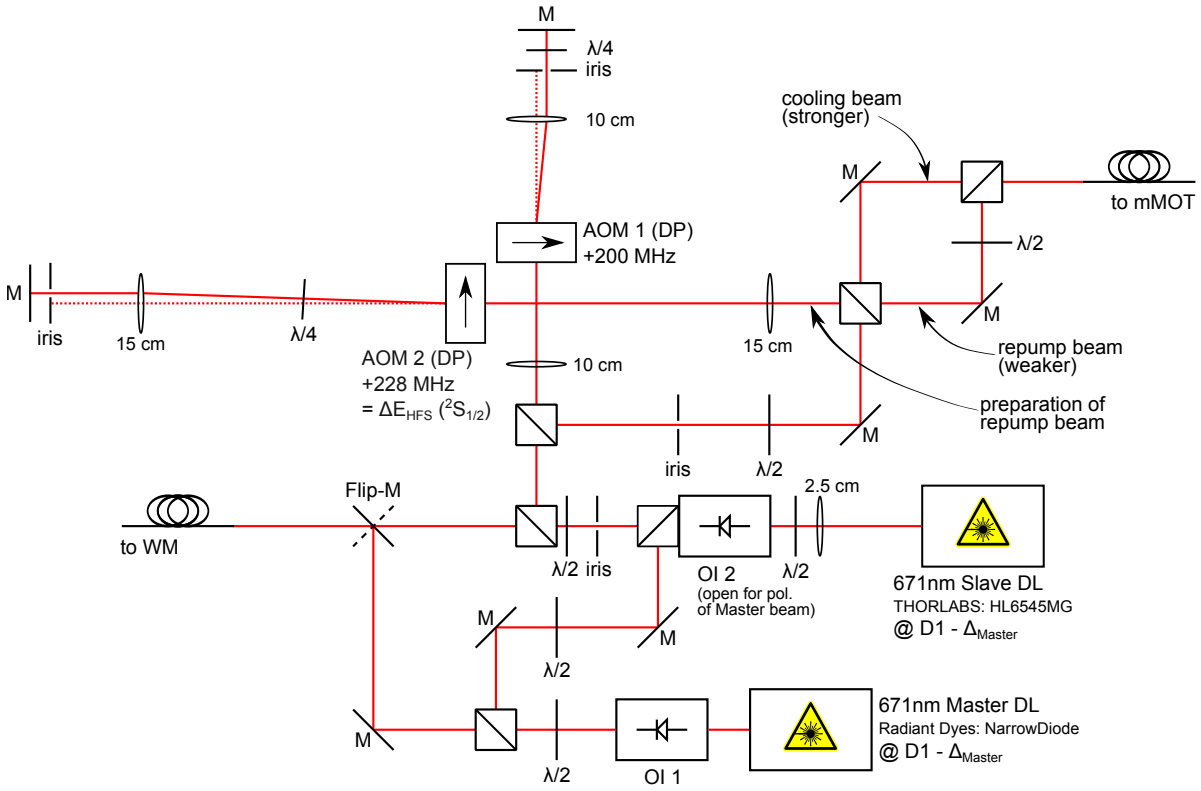

Figure 4.14.: Schematic of the optical setup of the master-slave diode lasers system for D1 grey-molasses cooling and repumping of ^{6}Li. The master laser's frequency is by Δ_{Master} below the D1 line. Two cat's eye (DP) double-pass AOM systems [112] serve for shifting and also tuning the cooling and repumping beam's absolute frequency detuning to the D1 transition, AOM 1, as well as their relative detuning, AOM 2. The frequency difference between the cooling beam and the weaker repump beam consists of the hyperfine structure splitting of the Li atom groundstate, $^2S_{1/2}$, and their detuning at the upper joint level of the D1 line, $^2P_{1/2}$. All beam splitters are polarising ones. The (Flip-M) flip-mirror is used to send either the slave or the master laser to the (WM) wavemeter.

quarter-wave plate twice changes the beam's polarisation by 90° which is important for beam separation on polarising beam splitters.

The master laser's[1] frequency is by Δ_{Master} below the D1 line, which will have to be determined precisely. It is optically isolated by an optical faraday isolator[2], OI 1. Via two pairs of a rotatable $\lambda/2$-wave plate and a PBS each, the slave laser[3] gets seeded by the master laser. For OI 2, which is of the same type, to be open for the master laser's polarisation, it has to be set perpendicular to the slave laser's polarisation.

When free-running, the slave diode laser emits laser light at a wavelength of $\lambda_{\text{free}} = 660.3$ nm with a power of $P = 54$ mW, if supplied with a current of $I = 160$ mA at a temperature of $T = 25\,°\text{C}$. In contrast, the seeding leads to a wavelength of $\lambda_{\text{seed}} = 670.99$ nm: Operation with a current of $I = 141.7$ mA, and an injected seed-power coming from the the master laser of $P_{\text{seed}} = 5$ mW, results in a slave laser power of $P = 24$ mW at $T = 70\,°\text{C}$. A (Flip-M) flip-mirror is used to send either the slave or the master laser to the (WM) wavemeter by coupling it into an optical glass fibre.

[1] Radiant Dyes NarrowDiode 671 nm
[2] LINOS FI-680-55V
[3] LD: HL6545MG (660 nm, 120 mW) https://www.thorlabs.com/thorcat/19400/HL6545MG-MFGSpec.pdf. Temperature controlled mount: TCLDM9 (TE-Cooled Mount for Ø5.6 mm and Ø9 mm Lasers) https://www.thorlabs.com/thorproduct.cfm?partnumber=TCLDM9

The slave laser's amplified light is now focussed through the cat's eye configuration of AOM 1, yielding an increase in frequency of +200 MHz. Moreover, AOM 1 can be used for fast switching of all grey-molasses lasers. Afterwards, it's polarisation is such that the light can get split into two arms—one direct path for the stronger cooling beam and one manipulative path for the preparation of the repumper. The latter is sent trough the second double-pass configuration with AOM 2: On the one hand, it bridges the hyperfine structure splitting of the Li atom groundstate, $^2S_{1/2}$, by increasing the cooling beam's frequency by $\Delta E_{\mathrm{HFS}} = 228$ MHz, and on the other hand, it's tuneability enables a relative frequency detuning between the two beams at the upper joint level of the D1 line, $^2P_{1/2}$.

Both, cooling and repumper beam are overlapped again, get coupled into an optical single-mode fibre and therein propagate to the mMOT region where they should create a grey-molasses.

Chapter 5

Investigations on Atom-Ion Interactions

This chapter is dedicated to theoretical investigations on atom-ion interactions. We want to study the collisional behaviour of hybrid systems and the possibility of sympathetically cooling ions with atoms. Moreover, a model for detection is introduced—the two-ion detector. Here, a co-trapped ion besides the atom cloud would be used to sympathetically read out the effect of collisions between an ion and an atom of the cloud it's immersed in. The stability as well as the cooling and heating of such two-ion crystals undergoing atom-ion collisions will be investigated, pointing out the differences to a single trapped ion.

First, one-dimensional elastic collisions will be investigated with focus on the sympathetically coolable atom-ion mass ratio $\mathfrak{M}_{\mathrm{ai}}$. The influence of the micromotion and ion trap voltages, i.e. Mathieu parameters q and a, and different temporal average determinations will be discussed. Secondly, the stability of a single ion and a two-ion crystal undergoing elastic collisions with atoms will be studied. This is crucial for the proposal of the sympathetic two-ion detector. For this purpose, the relevant time scales will be introduced. The critical energy above which the two-ion detector should work is determined by the competing impacts of momentum transfers by scattering events with either atoms or detection photons. Moreover, the creation of narrow fluorescence spectra through dark resonances will be discussed. These should allow for cooling the ions and detecting the hybrid interactions for temperatures below the Doppler temperature.

It will be shown that the individual constituents of the model should allow for sympathetic atom-ion detection using the two-ion detector. Due to the complexity of the model, the simulations on the combination of all constituents could not have been finished within the context of this thesis.

All analytical and numerical simulations are performed using Wolfram Mathematica.

5.1. 1D Newtonian Elastic Collisions

The simplest model for atom-ion collisions is a classical one-dimensional description based on elastic Newtonian hardcore collisions. This classical picture holds for sufficiently high temperatures compared to the trapping frequencies. All inelastic processes such as chemical reactions described in sec. 2.3 are consequently omitted. The scatterers internal degrees of freedom do not change. The further 1D description of collisions relies on the quasi-one-dimensional scenario in the ion trap—without spatial mode-coupling. Here, the ions' oscillations in spatial degrees of freedom are independent of each other. Furthermore, the scattering events themselves have to conserve the ions' direction of oscillation. i.e. be predominantly forward. The justification of this simplification will be studied below.

Since the radial modes of the ion crystal are assumed to be degenerate, we choose only one of them w.l.o.g., and start with a 2D description. The atom is assumed to rest while being hit

by the ion. From conservation of energy E, i.e. kinetic energy T, and momentum $\boldsymbol{p}$:

$$T_{\mathrm{tot}} = T_{\mathrm{i}} = T'_{\mathrm{i}} + T'_{\mathrm{a}} \quad \text{and} \quad \boldsymbol{p}_{\mathrm{i}} = \boldsymbol{p}'_{\mathrm{i}} + \boldsymbol{p}'_{\mathrm{a}} \,, \tag{5.1}$$

it follows in a standard classical two-dimensional elastic scattering process for the ion's momentum after collision, $\boldsymbol{p}'_{\mathrm{i}}$:

$$p'_{i(1/2)} = \Xi(\mathfrak{M}_{\mathfrak{ai}}, \theta) \cdot p_i := \frac{\cos(\theta) \pm \sqrt{\cos^2(\theta) - \left(1 - {\mathfrak{M}_{\mathfrak{ai}}}^2\right)}}{1 + \mathfrak{M}_{\mathfrak{ai}}} \cdot p_i \,. \tag{5.2}$$

Here, θ is the scattering angle, defined as the normalised projection of the scatterer's post-collisional momentum $\boldsymbol{p}'_i$ w.r.t. its pre-collisional momentum $\boldsymbol{p}_i$. The positivity of the radicand in (5.2) demands $\cos^2(\theta) \geq 1 - {\mathfrak{M}_{\mathfrak{ai}}}^2$, which results in a boundary condition for the scattering angle in its first restricted domain $0 < \theta < \pi$, as a function of the mass ratio:

$$|\theta| \leq -\arccos\left(-\sqrt{1 - {\mathfrak{M}_{\mathfrak{ai}}}^2}\right) \,. \tag{5.3}$$

Thus, for the combinations relevant in this context—Li/Yb^+ & Rb/Yb^+—the scattering angle is limited to:

$$|\theta_{\mathrm{Li/Yb^+}}| \lesssim 0.0112\pi \approx 2.02\,^\circ \,, \qquad |\theta_{\mathrm{Rb/Yb^+}}| \lesssim 0.1698\pi \approx 30.56\,^\circ \,. \tag{5.4}$$

This simple result corresponds with the fact found in [130], where the probability distributions $I(\theta, E_{\mathrm{col}})$ for the scattering angle θ in elastic collisions of energy E_{col} between $^{174}\mathrm{Yb}^+$ and $^{87}\mathrm{Rb}$ are numerically computed. In [130, Figure 4], the forward scattering peak at small θ becomes more pronounced for higher energies, and has decreased by at least one order of magnitude at an angle of about $0.5\,\mathrm{rad} \approx 0.16\pi \approx 28.6\,^\circ$, as in the case of $10\,\mu\mathrm{K}$, or even by four orders of magnitude as in the case of $10\,\mathrm{K}$.

In the following, a 1D model will be used to describe the elastic collisions, neglecting non-forward scattering. This simplified model will allow us to gain insight into the problem, while it will likely catch the relevant physics as well. We postpone a 3D calculation to the future. Typical and experimentally feasible trapping parameters which are used throughout the simulations unless noted otherwise, are listed in tab. 5.1.

parameter	value
$q := q_\rho$	0.1
$a := a_\rho$	0
$\Omega \equiv \Omega_{\mathrm{RF}}$	$2\pi \cdot 1$ MHz
$\omega := \omega_\rho$	$\sqrt{a_\rho + \frac{q_\rho^2}{2}\frac{\Omega}{2}} \approx 2\pi \cdot 35\,\mathrm{kHz}$

Table 5.1.: Typical and experimentally feasible trapping parameters used throughout the simulations, unless noted otherwise.

5.2. Sympathetically Coolable Mass Ratio $\mathfrak{M}_{\mathfrak{ai}}$

As described in the previous section, we are interested in classical, one-dimensional elastic hardcore collisions of ions with atoms. Only radial modes transverse to the ion trap axis are considered, because the axial mode doesn't feature micromotion, cf. (2.14) and subsec. 2.1.2.

For this purpose, the general form of a solution to the Mathieu equation (2.6) in harmonic approximation (2.18) is rewritten:

$$x(t) = x_\mathrm{C} \cos(\omega t) \left(1 + \frac{q}{2} \cos(\Omega t)\right) + x_\mathrm{S} \sin(\omega t) \left(1 + \frac{q}{2} \cos(\Omega t)\right) , \tag{5.5}$$

$$v(t) = \dot{x}(t) , \tag{5.6}$$

cf. (2.19). Here, x_C and x_S are the real-valued amplitudes of the cosine and sine oscillations, respectively. The superposition accounts for possible phase shifts between the oscillation of an ion and the trap driving frequency that result from atom-ion collisions. Due to one-dimensionality, indices for spatial direction are left out and w.l.o.g. x is chosen as radial direction of oscillation. The velocity of the ion is just the time derivative of its trajectory.

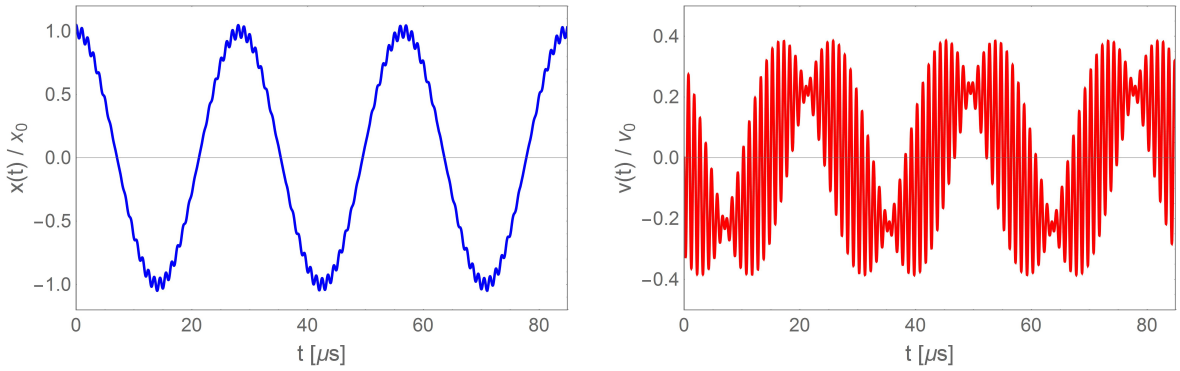

Figure 5.1.: Example of an ion trajectory and velocity in an ion crystal. [*left*] The normalised displacement $x(t)$ of the central ion is plotted for three periods of the slow secular motion. It's a harmonic oscillation, neglecting the fast micromotion. It exhibits that the superimposed micromotion vanishes at the trap centre. [*right*] The corresponding velocity $v(t)$ has a way more irritating temporal evolution. It's nearly periodic, but a possible phase between the trap driving RF $\Omega = 2\pi\,1\,\mathrm{MHz}$, i.e. micromotion, and the secular oscillation results in deviations.

In this scenario, the atom is assumed to be stationary. Thus, to implement the elastic atom-ion collisions into the simulation, the ion's position and velocity right before and after an individual collision at time t_col have to be linked:

$$x'(t_\mathrm{col}) = x(t_\mathrm{col}) \tag{5.7}$$

$$v'(t_\mathrm{col}) = \Xi \cdot v(t_\mathrm{col}) . \tag{5.8}$$

Here, Ξ is the momentum transfer coefficient of the ion which describes the possible change in momentum from $v(t_\mathrm{col})$ to $v'(t_\mathrm{col})$. The ion's position does not change, since the collision happens instantaneously. Momentum and energy conservation gives:

$$m_\mathrm{i} v_\mathrm{i}' + m_\mathrm{a} v_\mathrm{a}' = m_\mathrm{i} v_\mathrm{i} , \qquad \frac{1}{2} m_\mathrm{i} v_\mathrm{i}'^2 + \frac{1}{2} m_\mathrm{a} v_\mathrm{a}'^2 = \frac{1}{2} m_\mathrm{i} v_\mathrm{i}^2 \tag{5.9}$$

$$\Rightarrow \quad \Xi := \frac{m_\mathrm{i} - m_\mathrm{a}}{m_\mathrm{i} + m_\mathrm{a}} = \frac{1 - \frac{m_\mathrm{a}}{m_\mathrm{i}}}{1 + \frac{m_\mathrm{a}}{m_\mathrm{i}}} =: \frac{1 - \mathfrak{M}_\mathrm{ai}}{1 + \mathfrak{M}_\mathrm{ai}} , \tag{5.10}$$

since the atom is initially assumed to be at rest, $v_\mathrm{a} = 0$. It's worth noticing that the momentum transfer coefficient Ξ only depends on the atom-ion mass ratio $\mathfrak{M}_\mathrm{ai}$ of the selected species.

As starting boundary condition for the ion, w.l.o.g. pure cosine oscillation is assumed, i.e.

$x_C = x_0$ and $x_S = 0$. By solving the transfer equations (5.7) and (5.8) analytically, one obtains the oscillation amplitudes x'_C and x'_S after the hardcore collision.

Since we are interested in sympathetic collisional cooling, it's now interesting to look at the ratio of the ion's energy before and after the collision as a function of the collision phase ϕ_{col}:

$$\frac{E'_i}{E_i}(\phi_{col}) = \frac{x'^2_C(\phi_{col}) + x'^2_S(\phi_{col})}{x_0^2(\phi_{col})} \,. \tag{5.11}$$

This calculation is performed for one secular period $T_{sec} = \frac{2\pi}{\omega} \approx \frac{4\pi}{\beta\Omega}$, and several characteristic atom-ion element combinations, from the smallest feasible mass ratio to the case of atoms being more than two times heavier than the ionic species. The radio frequency is set to $\Omega = 2\pi \cdot 1$ MHz, while $q = 0.1$ and $a = 0$. The result is plotted in fig. 5.2, revealing both a strong dependence on the phase at the collision time ϕ_{col} and on the mass ratio $\mathfrak{M}_{ai} = m_a/m_i$.

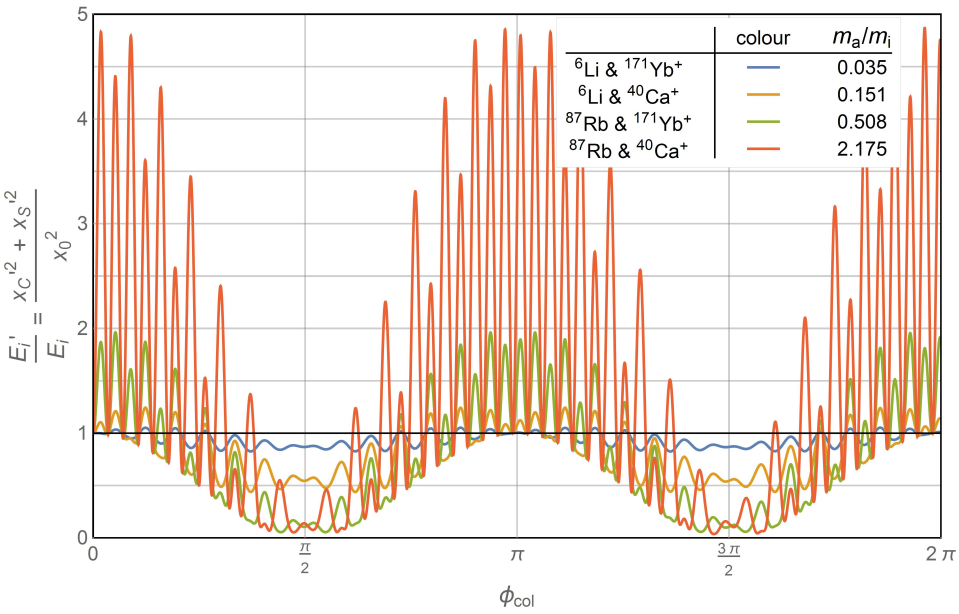

Figure 5.2.: Relative energy change of an ion due to atom-ion hardcore collisions as a function of the collision phase ϕ_{col}. The plot extends over the duration of one secular period. Several characteristic atom-ion combinations are chosen, i.e. from small to large mass ratios $\mathfrak{M}_{ai} = m_a/m_i$.

As can be seen, the overall shape of the relative change in the energy of an ion due atom-ion hardcore collisions, follows the fast micromotion, cf. fig. 5.1. Moreover, the disturbance of a heavy ion by a light atom, such as (blue) ^{171}Yb$^+$ and ^{6}Li, is way smaller than the change in energy of a light ion hitting a heavy atom (red). Naturally, both the maximal energy gain and loss increase with increasing mass ratio $\mathfrak{M}_{ai}$.

Clearly, the average change in energy is an important quantity for describing multiple collisions in the long run. The most simple and reasonable averaging is the time averaging over one secular period $T_{sec} = \frac{2\pi}{\omega} \approx \frac{4\pi}{\beta\Omega}$. Since the denominator of the time-varying relative energy change contains fast oscillating terms with prefactors up to the order of q^2, it poses problems to the computation. To circumvent this issue, a Taylor series expansion in q around 0 is performed, keeping terms up to the second order. The other terms in the numerator of (5.11) are not affected. This is justified, because $q^2 \ll 1$ has to be fulfilled, cf. subsec. 2.1.2. Afterwards,

the relative change in energy gets time-averaged for one slow secular period:

$$\gamma := \left\langle T_2\left[\frac{E_\mathrm{i}'}{E_\mathrm{i}}(q;0)\right]\right\rangle_{T_\mathrm{sec}} = \frac{2\pi}{\omega}\int_0^{\frac{2\pi}{\omega}} T_2\left[\frac{E_\mathrm{i}'}{E_\mathrm{i}}(q;0)\right] . \tag{5.12}$$

The series-expanded and time-averaged relative energy change γ, can now be computed for different Mathieu parameters q as a function of the mass ratio. The analytical result in shown in fig. 5.3. At first glance, one recognises that there is hardly any q-dependence, since the curves overlap. On average over one secular period, the colliding ion will heat up for values of $\gamma > 1$, while it will cool for values of $\gamma < 1$. Our atom-ion combination, ^{6}Li & ^{171}Yb$^+$ with a mass ratio of roughly $\mathfrak{M}_\mathrm{ai} \approx 0.035$, will thus experience energy decrease on average. In contrast, hybrid systems with heavier atoms compared to ions will on average heat up the colliding ion.

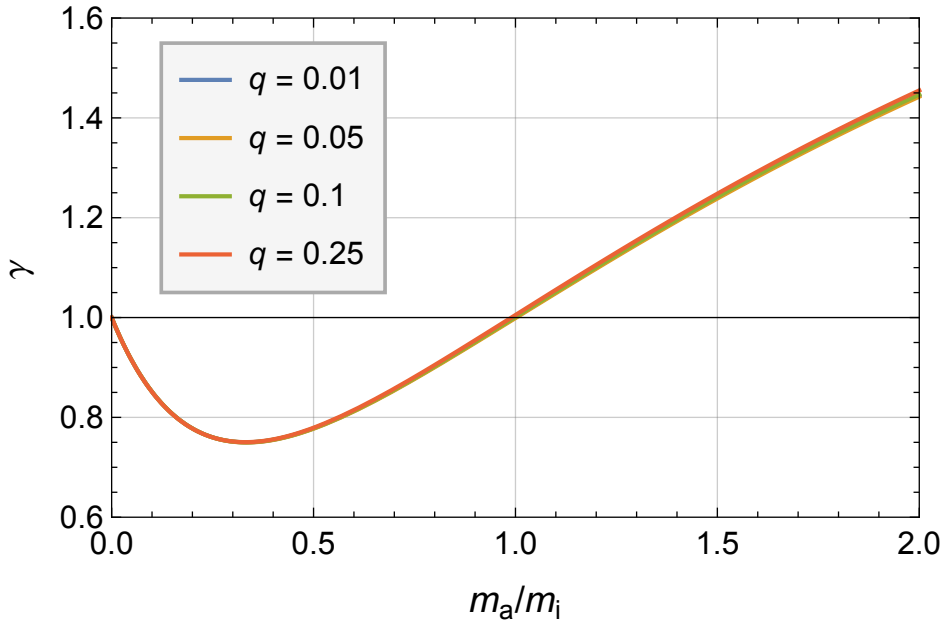

Figure 5.3.: Time-averaged relative energy change due to atom-ion collisions as a function of the mass ratio. For analytical computation, a Taylor series expansion in q around 0 has to be performed to second order. The time averaging extends over one secular period T_sec.

By limiting $q \to 0$ after the time averaging and Taylor series expansion, one obtains an approximate analytical expression for the relative change in the ion's energy in relation to the mass ratio:

$$\lim_{q\to 0}\gamma = \frac{1+3\mathfrak{M}_\mathrm{ai}{}^2}{(1+\mathfrak{M}_\mathrm{ai})^2} = \frac{m_\mathrm{i}^2+3m_\mathrm{a}^2}{(m_\mathrm{i}+m_\mathrm{a})^2} . \tag{5.13}$$

Additionally, numerical simulations have been performed to check the influence of the approximations in the analytical simulation. Here, the non-approximated relative energy change gets averaged over 10 secular periods and values for the mass ratio in steps of 0.1 are used:

$$\gamma_\mathrm{num} = \left\langle\frac{E_\mathrm{i}'}{E_\mathrm{i}}\right\rangle_{10T_\mathrm{sec}} = \left\langle\frac{x_\mathrm{C}'^2(\phi_\mathrm{col})+x_\mathrm{S}'^2(\phi_\mathrm{col})}{x_0^2(\phi_\mathrm{col})}\right\rangle_{10T_\mathrm{sec}} . \tag{5.14}$$

In fig. 5.4, the different methods used to compute the time-averaged relative energy change

γ are compared. The numerical simulation confirms the approximated analytical solution for $q = 0.1$, and the limiting case of $q \to 0$.

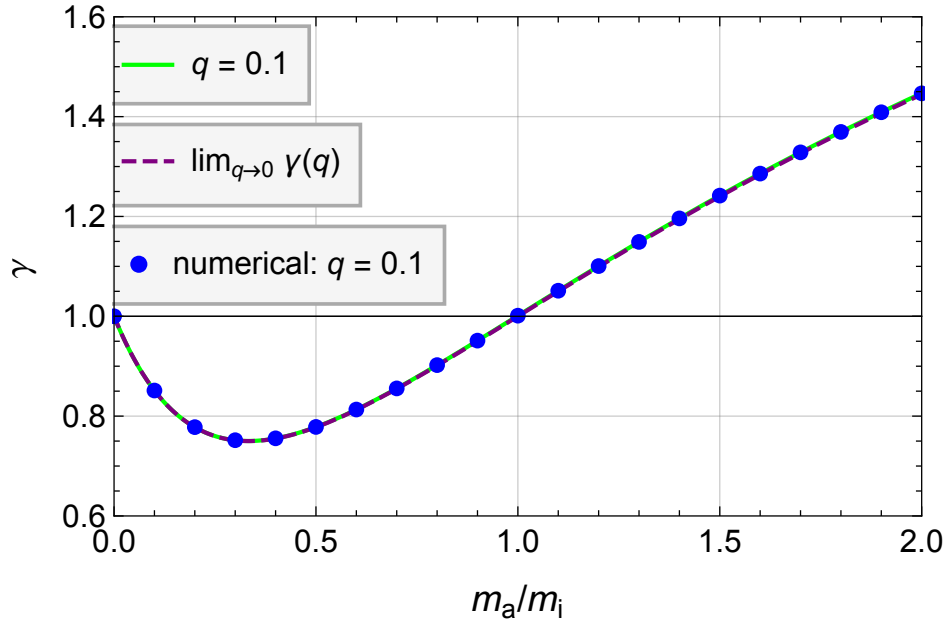

Figure 5.4.: Comparison of the different methods used to obtain the time-averaged relative change in the ion's energy due to hardcore collision as a function of the mass ratio. (green) Approximate analytical solution, (purple dashed) limiting case of q approaching 0, and (blue dots) non-approximated numerical simulation.

Within the above simulations, several assumptions have been made besides the harmonic approximation, e.g. a vanishing static Mathieu parameter $a = 0$, initially resting atoms $v_\mathrm{a} = 0$, and a scattering rate which is independent of the ion velocity. To be more realistic, the scattering rate has to be proportional to the absolute value of the ion's velocity:

$$\Gamma = n_\mathrm{a}(x)|v_\mathrm{i}(t)|\sigma \,. \tag{5.15}$$

Moreover, it depends on the density of atoms $n_\mathrm{a}(x)$ which we assume to be homogeneous in the presents study, and the scattering cross section σ. Now, the velocity dependence will be introduced. The uniformly distributed atoms are still assumed to be at rest and thus emerge spontaneously at the ion's position.

The problem occuring here is that the absolute value of the ion's velocity $|v_\mathrm{i}(t)|$ is not analytically integrable. Thus, the weighting function $|v_\mathrm{i}(t)|$ causes us to only do a numeric simulation. The concept is to numerically integrate the velocity weighted relative change in energy over 10 secular periods:

$$\gamma_\mathrm{num}^\mathrm{vel} = \frac{\left\langle |v(t)| \frac{E_\mathrm{i}'}{E_\mathrm{i}} \right\rangle_{10T_\mathrm{sec}}}{\langle |v_\mathrm{i}(t)| \rangle_{10T_\mathrm{sec}}} \tag{5.16}$$

$$= \frac{\int_0^{10T_\mathrm{sec}} \mathrm{d}t |v_\mathrm{i}(t)| \frac{x_\mathrm{C}^2 + x_\mathrm{S}^2}{x_0^2}}{\int_0^{10T_\mathrm{sec}} \mathrm{d}t |v_\mathrm{i}(t)|} \,. \tag{5.17}$$

An example of the probability distribution used for introducing velocity dependent scattering rate can be seen in fig. 5.5. It corresponds to the graphs of the ion trajectory and velocity in fig. 5.1. The absolute value of the ion velocity $|v_\mathrm{i}(t)|$ is used as weighting function for the temporal averaging of the relative energy change due to atom-ion collisions, $\gamma_\mathrm{num}^\mathrm{vel}$. The weighting function is plotted for one secular period, within which an event is forced to happen in this specific simulation. This has no impact on the time-averaged results, but would be important for multiple consecutive collisions. Here, the probability for an event to happen within one secular period would have to be less than 1, in order to allow for multiple secular oscillations of the ion before it collides with the atom. This probability would depend on the density of atoms $n_\mathrm{a}(x)$ and the scattering cross section σ, as indicated in the general relation for the scattering rate (5.15).

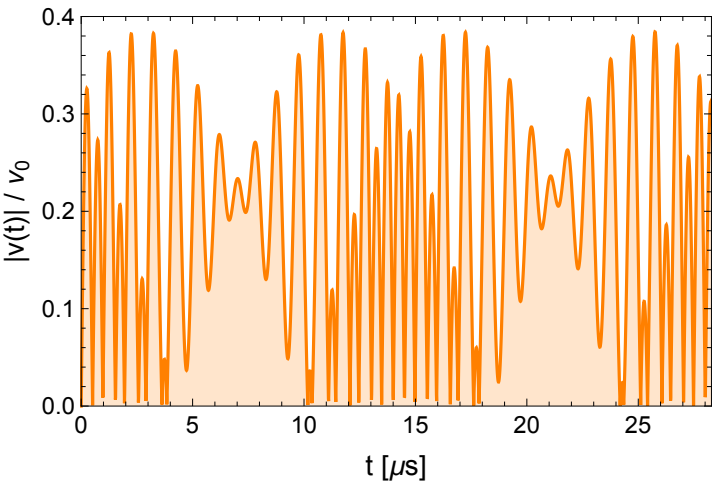

Figure 5.5.: Example of the velocity-weighting function for introducing a velocity dependent scattering rate. The absolute value of the ion velocity $|v_\mathrm{i}(t)|$ is plotted normalised for a secular period. It corresponds to the graphs of the ion trajectory and velocity in fig. 5.1.

In the plot of the simulation result fig. 5.6, the time-averaged and velocity-weighted $\gamma_\mathrm{num}^\mathrm{vel}$ is compared to the non-weighted case, both for $q = 0.1$. It can be seen that the overall shape of the dependence on the mass ratio is roughly the same. However, two features differ: The critical value $\gamma = 1$ is shifted to smaller mass ratios than $m_\mathrm{a}/m_\mathrm{i} = 1$, which results in a smaller range of mass ratios still enabling cooling. Moreover, the cooling (heating) effect is more pronounced for smaller (larger) mass ratios than the critical one as compared to the non-weighted case.

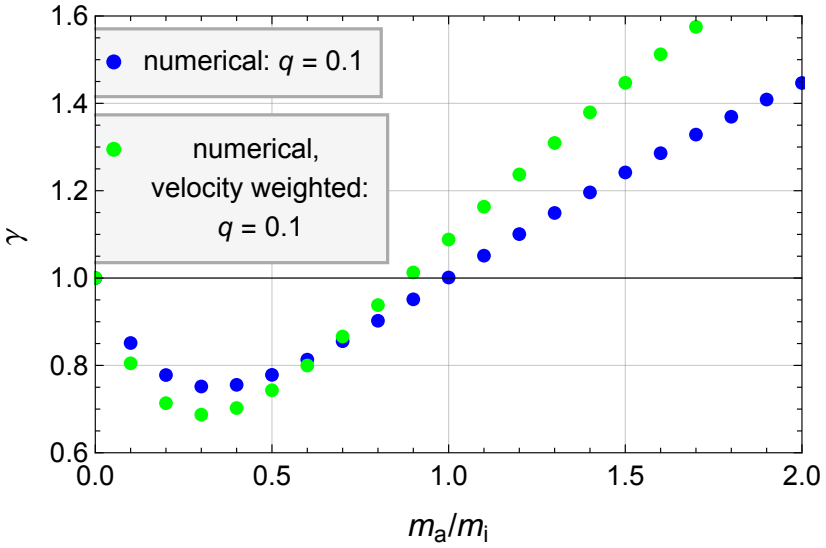

Figure 5.6.: Comparison of velocity-weighted and non-weighted time-averaged relative energy change in dependence of the mass ratio.

It's important to note that although, for the case of $\gamma > 1$ with an increase of energy on average, it can happen that in the long run the ion gets cooled sympathetically. Multiple collisions may raise the energy stepwise, but a single or few collisions may suffice to extract nearly all momentum from the ion, such that it has practically no velocity anymore.

A look at the distributions of non-averaged γ's for different mass ratios may clarify this subtlety. For this purpose, 20001 individual collisions are simulated numerically. The relative energy change gets calculated like in the previous numerical simulations, but without time averaging over the secular period.

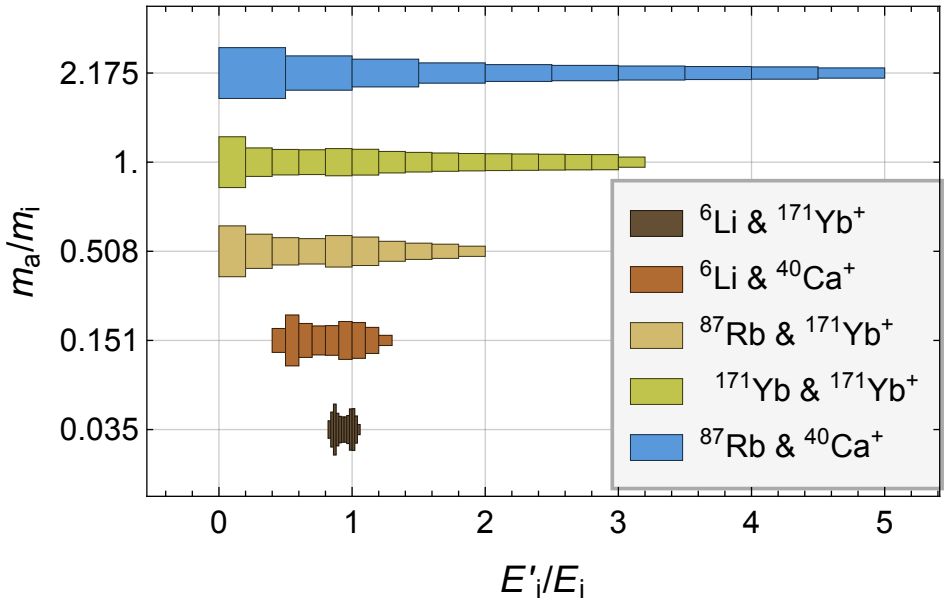

Figure 5.7.: Distributions of the relative energy changes due to elastic collisions for different atom-ion combinations. It's a histogramm-like plot, showing the accumulated binned number of collisions for five characteristic mass ratios. For each mass ratio, 20001 events are simulated. Thus, the absolute height of a bin can not be compared to bins of other atom-ion combinations.

The distribution of the combination with the largest mass ratio of roughly 2.175, ^{87}Rb & ^{40}Ca$^+$, has the widest spread. One collision can increase the energy of the comparatively light ion upto fivefold. Although the time-averaged relative energy changes for this mass ratio lead to a heating on average, cf. fig. 5.3, single collisions may extract nearly all the momentum from the ion corresponding to $\frac{E'_i}{E_i} \approx 0$. Consequently, it may happen that mass ratios larger than 1 result in cooling of the ion.

All other atom-ion combinations exhibit a striking double-peak structure that gets more pronounced for smaller mass ratios. In the case of equal atom and ion species, i.e. $\mathfrak{M}_{ai} = 1$,[1] the fraction of those collisions removing nearly all energy from the ion is the largest. The second peak is around $\frac{E'_i}{E_i} = 1$, corresponding to events that leave the ion's energy unchanged.

Comparing the two combinations with an ^{171}Yb$^+$ ion, it becomes evident that far less energy can be removed from or added to the ion by a light atom. Our combination possesses the narrowest distribution of relative energy changes. Maximally, the ^{171}Yb$^+$ ion can end up with 1.07 times it's pre-collisional energy. The major part of the distribution has values below 1. Consequently, nearly all collisions with ^{6}Li atoms cool the ion.

[1] The excess electron's mass of the neutral ^{171}Yb atom is neglected.

Numerical simulations of sympathetic cooling including the velocity-weighting have been performed. To circumvent the previously mentioned issue of the velocity-weighting, the evolution of the absolute value of the ion's velocity $|v_i(t)|$, has been turned into a probability density function. It samples collision times, taking the velocity dependence of the scattering rate into account. In fig. 5.8, the collisional sympathetic cooling of $^{171}Yb^+$ ions with ^6Li atoms for more than 2 ms is displayed. Each blue dot corresponds to one collision event. It can be seen that there are certain collisons which increase the ion's energy slightly. In the long run, the effect of the small atom-ion mass ratio dominates and cooling can be observed. Another example is displayed in fig. 5.9 for ^{87}Rb & $^{40}Ca^+$, demonstrating the accidental occurance of collisions that heat the ion quite much in combination with cooling collisions.

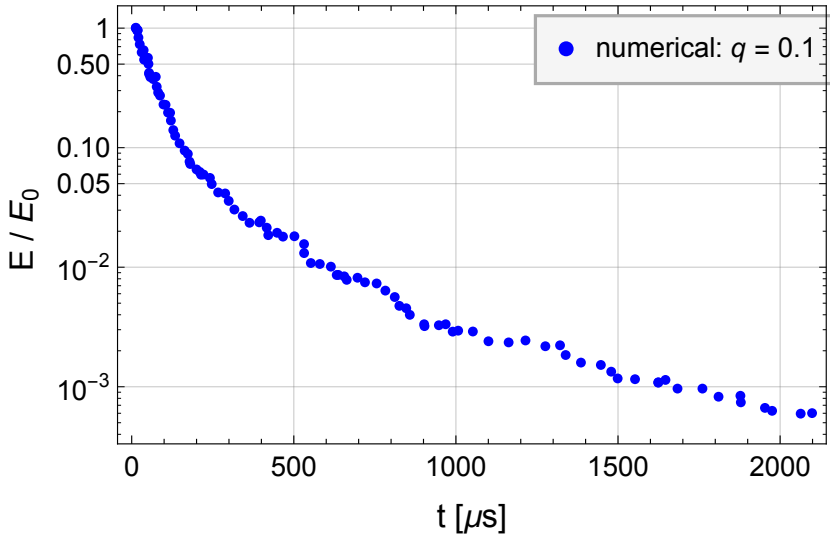

Figure 5.8.: Numerical simulation of sympathetic cooling of $^{171}Yb^+$ with ^6Li. Each blue dot represents an individual event. The ordinate displays the relative energy change and is plotted logarithmically since there is no absolute energy scale in the classical description.

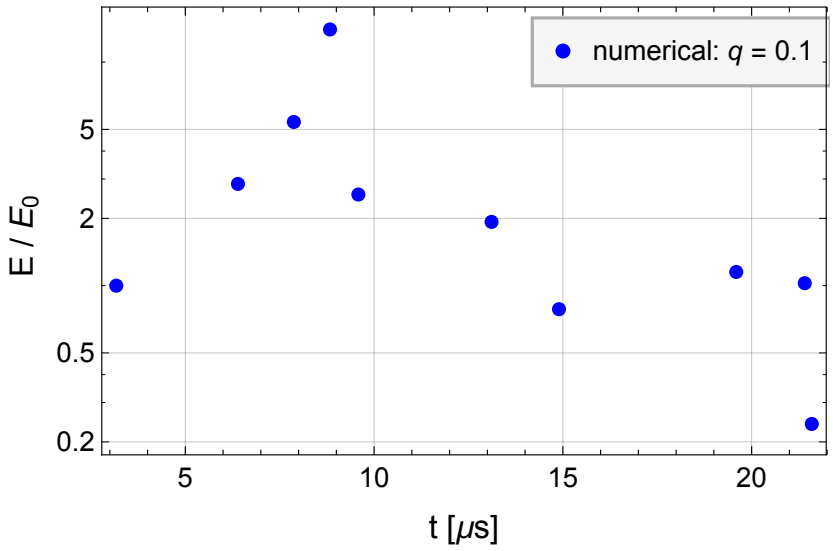

Figure 5.9.: Numerical simulation of collisions of $^{40}Ca^+$ with ^{87}Rb. This example illustrates the jumps in energy due to single collisional events. Besides the mass ratio, the energy change drastically depends on the collision phase of the micromotion.

So far, the static Mathieu parameter has been set to $a = 0$. Now, an a dependence will be introduced, resulting in different secular trap frequencies ω. As stated in subsec. 2.1.2, a non-vanishing a results in general from a DC voltage applied to the endcaps of the ion trap. In addition, it may originate from any additional constant trapping potential, e.g. a superimposed optical dipole trap for the ions. Since we are only interested in stable solutions with real-valued secular frequencies $\omega \approx \sqrt{a + \frac{q^2}{2}}\frac{\Omega}{2}$ in the harmonic approximation, a lower limit can be determined for a. The radicand's positivity demands:

$$a > -\frac{q^2}{2} \,. \tag{5.18}$$

For the case of $q = 0.1$, this boundary amounts to $a > -0.005$, so that the ionic oscillations are stable. The same procedure as in the case of the analytical solution for different q values is applied, i.e. Taylor series expansion of the relative energy change in q around 0, and subsequent time averaging over one period of the secular motion T_{sec}. The q Mathieu parameter is fixed to $q = 0.1$ and the a parameter is varied.

The impact of the Mathieu a parameter on the time-averaged relative energy change due to atom-ion collisions is shown in fig. 5.10. Generally, $a > 0$ results from an additional constant trapping potential of any kind, whereas $a < 0$ can be interpreted as an additional anti-trapping potential for the respective spatial mode. Evidently, the influence of a on the heating or cooling effect is way larger than the one of q, cf. fig. 5.3. Positive a allows for the cooling of larger mass ratios on average, while negative values shrink the range of coolable mass ratios and amplify the average energy gain γ drastically.

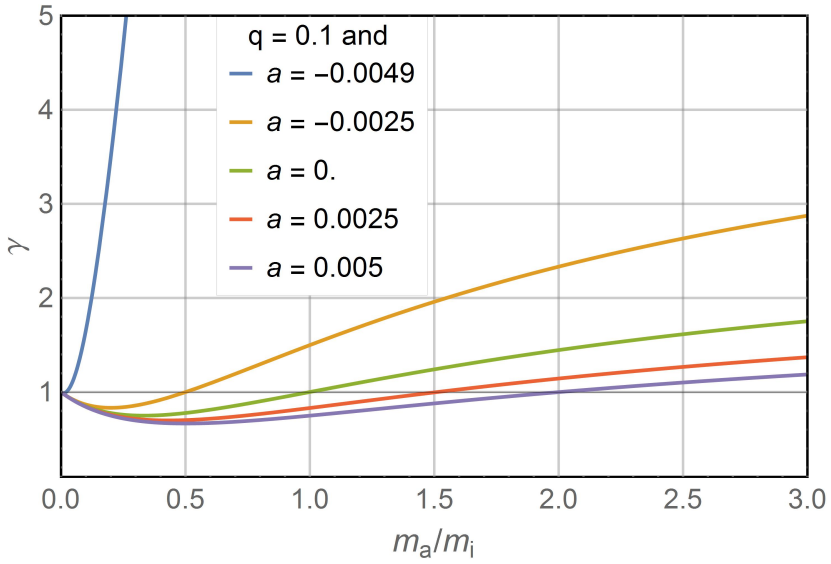

Figure 5.10.: Impact of the Mathieu a parameter on the time-averaged relative energy change due to atom-ion collisions. For analytical computation, a Taylor series expansion in q around 0 has to be performed to second order. The time averaging extends over one secular period T_{sec}. The q Mathieu parameter is fixed to $q = 0.1$ and the a parameter is varied. $a > 0$ results from an additional constant trapping potential of any kind, whereas $a < 0$ can be interpreted as an additional anti-trapping potential.

5.3. Stability of a Two-Ion Crystal

Regarding the immersion of individual ions into an ultracold atom cloud, the stability of the ion crystal will be investigated. In the model of the two-ion detector, one ion is immersed into the atom cloud where it undergoes collisions. The influence of a second ion which is used for detection on the stability of the ion crystal will be studied.

We are interested in the displacement of the immersed ion 1 in one of the two degenerate radial directions caused by elastic atom-ion collisions. Here, we chose w.l.o.g.[1] the spatial mode along $\hat{\boldsymbol{x}}$, namely $x_1(t)$. The transformation of oscillations of two ions between the particle and eigenmode description is given by:

$$\begin{aligned} x_\mathrm{c}(t) &= x_1(t) + x_2(t) & \qquad x_1(t) &= \tfrac{1}{2}\left(x_\mathrm{c}(t) + x_\mathrm{s}(t)\right) \\ x_\mathrm{s}(t) &= x_1(t) - x_2(t) & \qquad x_2(t) &= \tfrac{1}{2}(x_\mathrm{c}(t) - x_\mathrm{s}(t)) \,. \end{aligned} \tag{5.19}$$

Since both, COM and stretch mode become excited when a collision occurs, the most general ansatz for the oscillation of ion 1 is a superposition of both:

$$x_1(t) = \frac{1}{2}(A_\mathrm{c}\cos(\omega_\mathrm{c}t) + B_\mathrm{c}\sin(\omega_\mathrm{c}t) + A_\mathrm{s}\cos(\omega_\mathrm{s}t) + B_\mathrm{s}\sin(\omega_\mathrm{s}t))\left(1 + \frac{q}{2}\cos(\Omega t)\right) \,. \tag{5.20}$$

Here, the amplitudes indexed "c" correspond to the COM mode, and "s" to the stretch mode, while A and B are used for cosine and sine terms, respectively, to account for a phase between the two modes. As shown in subsec. 2.1.3, the secular COM and stretch frequencies are given by:

$$\begin{aligned} \omega_\mathrm{c} &= \frac{\Omega}{2}\beta_\mathrm{c} \approx \frac{\Omega}{2}\sqrt{a_x + \frac{q_x}{2}} = \frac{\Omega}{2}\sqrt{-\frac{a_z}{2} + \frac{q}{2}} \,, \\ \omega_\mathrm{s} &= \sqrt{\omega_\mathrm{c}^2 - \omega_z^2} = \frac{\Omega}{2}\beta_\mathrm{s} \approx \frac{\Omega}{2}\sqrt{-\frac{3a_z}{4} + \frac{q^2}{2}} \,. \end{aligned} \qquad \text{with} \quad \omega_z = \sqrt{a_z}\frac{\Omega}{2} \,, \tag{5.21}$$

It's worth noticing, that in contrast to the axial direction, in the radial directions, the COM mode frequency is not the smallest eigenfrequency, but higher than the stretch mode frequency, $\omega_\mathrm{c} > \omega_\mathrm{s}$.

A collision of an atom with ion 1 immersed in the atom cloud at time t_col, where nothing happens to the detection ion 2, looks as follows:

$$\begin{pmatrix} x_1 \\ x_2 \\ v_1 \\ v_2 \end{pmatrix}'(t_\mathrm{col}) = \mathrm{diag}(1, 1, \Xi, 1)\begin{pmatrix} x_1 \\ x_2 \\ v_1 \\ v_2 \end{pmatrix}(t_\mathrm{col}) \,. \tag{5.22}$$

In the eigenmode basis, the collisions can be rewritten as:

$$\begin{aligned} x_\mathrm{c}'(t_\mathrm{col}) &= x_\mathrm{c}(t_\mathrm{col}) & \qquad v_\mathrm{c}'(t_\mathrm{col}) &= \tfrac{\Xi-1}{2} \cdot v_\mathrm{c}(t_\mathrm{col}) \\ x_\mathrm{s}'(t_\mathrm{col}) &= x_\mathrm{s}(t_\mathrm{col}) & \qquad v_\mathrm{s}'(t_\mathrm{col}) &= \tfrac{\Xi+1}{2} \cdot v_\mathrm{s}(t_\mathrm{col}) \,. \end{aligned} \tag{5.23}$$

The simulations are performed numerically. One important assumption is the distribution of energy into the eigenmodes of the ion crystal. Here, equipartition of energy in COM and stretch mode is assumed at the start of the simulation:

$$x_\mathrm{s} \cdot \omega_\mathrm{s} = x_\mathrm{c} \cdot \omega_\mathrm{c} \,. \tag{5.24}$$

[1] without loss of generality

From this, it follows that the relative change in energy due to a collision can be expressed as:

$$\frac{E_\mathrm{i}'}{E_\mathrm{i}} = \frac{\omega_\mathrm{c}^2\left(A_\mathrm{c}'^2 + B_\mathrm{c}'^2\right) + \omega_\mathrm{s}^2\left(A_\mathrm{s}'^2 + B_\mathrm{s}'^2\right)}{\omega_\mathrm{c}^2\left(A_\mathrm{c}^2 + B_\mathrm{c}^2\right) + \omega_\mathrm{s}^2\left(A_\mathrm{s}^2 + B_\mathrm{s}^2\right)} \,. \tag{5.25}$$

For a stability diagram to be calculated, one obviously needs a criterion for stability. Again, just as in the general case described in subsec. 2.1.3, the stability criterion is the demand for real-valued secular frequencies. This is equal to the demand of real-valued positive "β's", and thus the positivity of the radicand in β. Since $\beta_\mathrm{s} < \beta_\mathrm{c}$, β_s imposes a higher requirement and consequently suffices as stability criterion. Since there is no stretch mode for the one-ion case, but only the COM mode, the criterion for the stability is here the positivity of the radicand of β_c. The stability criterion is thus $q^2/2 - a_z/2 > 0$, instead of $q^2/2 - 3a_z/2 > 0$ as in the two-ion case.

In order to compute the stability diagram numerically, the Mathieu parameters are varied stepwise, q from 0.001 to 0.26 in steps of 0.002, and a from 0 to 0.03 in steps of 0.0003. For each combination of parameters 4000 collisions are sampled at randomised collision times, which get averaged afterwards. The resulting stability diagram of a two-ion crystal with one immersed ion colliding with atoms is displayed in fig. 5.11. As species, two $^{171}\mathrm{Yb}^+$ ions and $^{87}\mathrm{Rb}$ atoms are used instead of $^{6}\mathrm{Li}$ atoms. The reason for this will become clear in the context of the energy scales of the two-ion detector, presented in sec. 5.4.

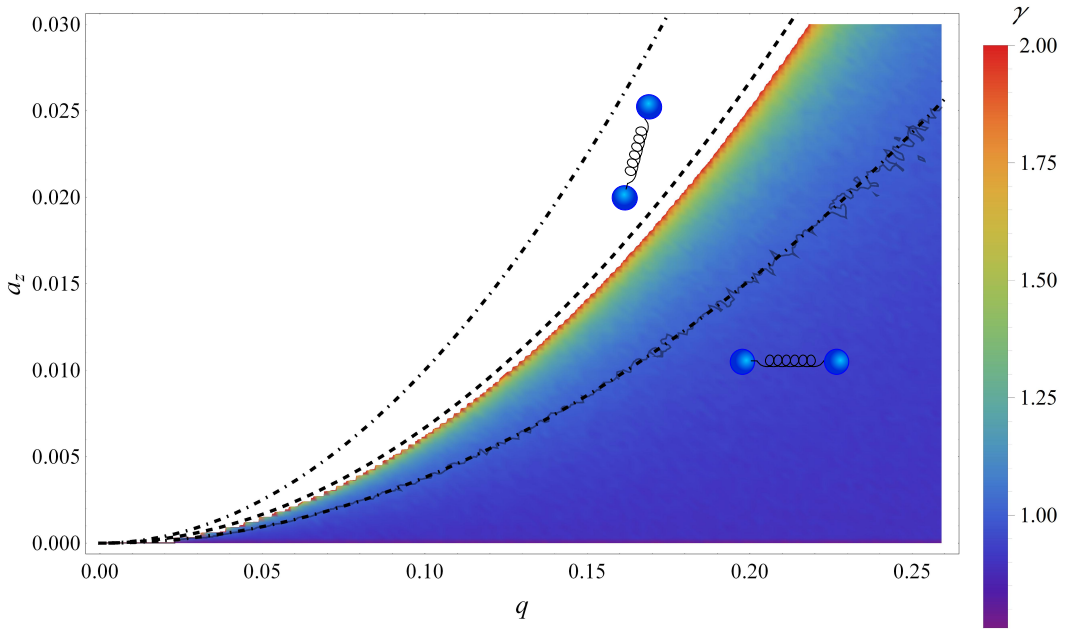

Figure 5.11.: Two-ion stability diagram of sympathetic atom-ion cooling. One of the two $^{171}\mathrm{Yb}^+$ ions undergoes collisions with $^{87}\mathrm{Rb}$ atoms.

Four characteristic regions are indicated, separated by the black dashed and dotdashed curves: The boundary between stability and instability of the two-ion crystal is indicated by the black dashed line next to the coloured region. The tilted two-ion schematic illustrates the instability. Here, the two ions change their arrangement from lying on the trap axis z to an instable configuration. To large values of a compress the the ion crystal axially, until its orientation flips. It's worth noticing that within this region, a "one-ion crystal" colliding with atoms is still stable. On the left-hand side of the left black dotdashed curve, a single ion cannot be trapped stably, too.

The other two regions are stable and coloured according to the heating or cooling effect of the atom-ion collisions. The critical border of $\gamma = 1$ separating the cooling from the heating region is interpolated and has a quadratic behaviour, indicated by the superimposed dotdashed black curve. Dark blue and violet means cooling on average, while values of $\gamma > 1$ correspond to heating on average. Close to the stability border, the heating is the most (red). Here, values larger than $\gamma = 2$ are not plotted for better scaling. In the outermost right-hand region (dark blue), collisions of the immersed ion with atoms sympathetically cool the crystal.

For comparison, the single-ion case has been simulated analogously and is shown in fig. 5.12. Here, three regions can be identified: First, the uncoloured left region, where the single-ion crystal is instable. It's separated by the black dotdashed curve. Secondly, the intermediate region, where the ion is trapped stably, but experiences heating on average. The third region lies below the right black curve ($\gamma = 1$), where the ion gets sympathetically cooled on average. Looking at the coloured stability regions, one notes that red and violet is more pronounced than in the two-ion case: Close to the stability border, larger energy gains can be observed (red), while the ion gets cooled more intensely for small values of a_z (violet). Thus, one can conclude that the impact of atoms colliding with a single ion is larger than in the two-ion case, which is to be expected since more degrees of freedom need to be cooled. Consequently, cooling a two-ion crystal via atom collisions is harder than cooling a single ion. Moreover, the two-ion crystal experiences less heating close to the stability border. One should benefit from this when trying to sympathetically cool a two-ion crystal via elastic atom-ion collisions.

The larger instability region for the two-ion case can be interpreted as a kind of additional static trapping potential for the colliding ion which originates from the second ion. It can be expressed in a shift of the static Mathieu parameter form the one-ion case with a_c to two-ions with a_s:

$$a_\mathrm{s} = a_\mathrm{c} - \left(2\frac{\omega_z}{\Omega}\right)^2 = -\frac{3}{2}a_z \,. \tag{5.26}$$

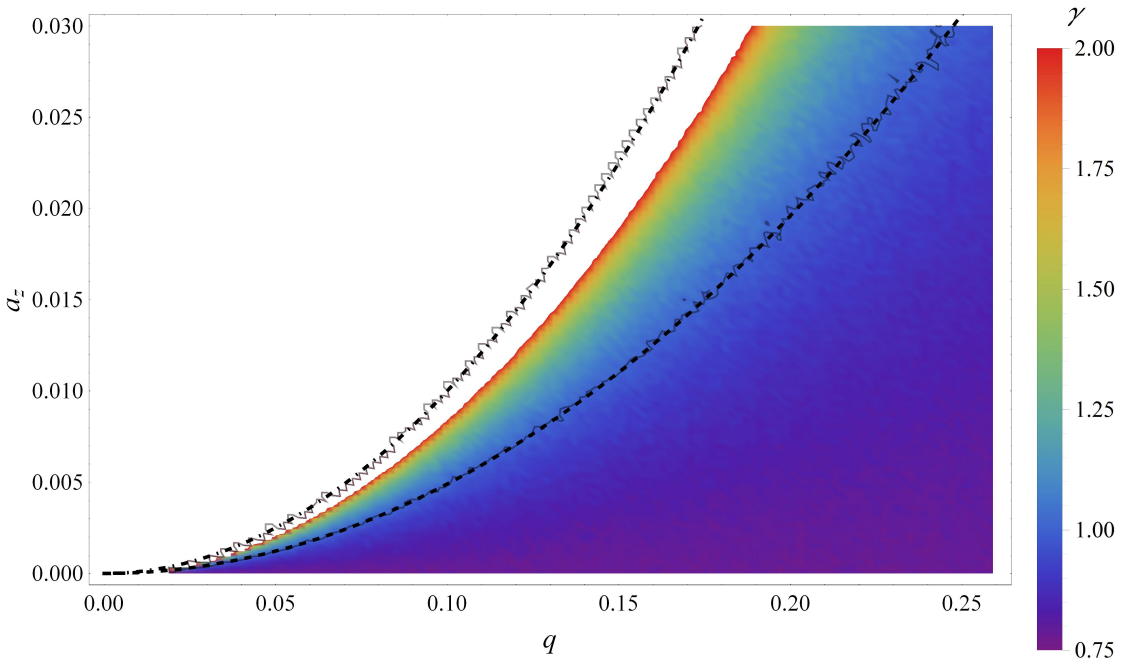

Figure 5.12.: One-ion stability diagram of sympathetic atom-ion cooling. One $^{171}Yb^{+}$ ion undergoes collisions with ^{87}Rb atoms.

The questions remains, what impact the effect of seemingly decreasing cooling capability has on a crystal of more than two ions. This is important for the investigation of the interaction of a larger ion crystal with the ultracold atoms. One attempt to a solution is the usage of small axial confinement, i.e. small a_z. On the other hand, it's unclear what would happen, when more than one ion of a crystal of more than two ions is immersed into the atom cloud. This will have to be investigated further in the near future.

5.4. Two-Ion Detector

This section will address the question to what extend the detection on an auxiliary ion allows for gain of information on the collisions between another ion and atoms of an ultracold atomic cloud it's immersed in. We want to analyse whether this detection scheme enables to observe the ion string's decrease in temperature due to sympathetic cooling in real-time, and whether individual scattering events may be detected by, e.g. a change in fluorescence.

5.4.1. Concept & Energy and Time Scales

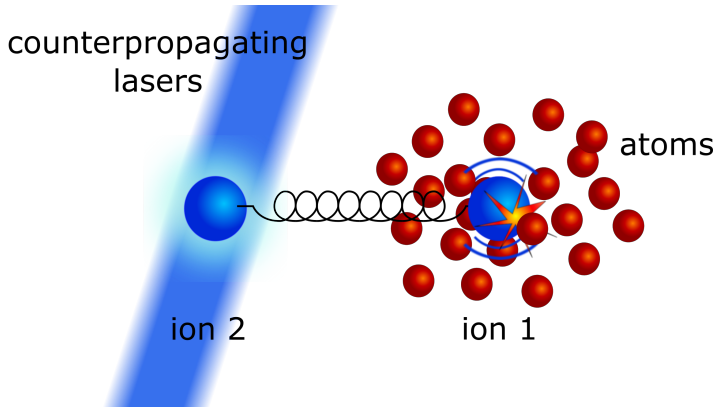

Figure 5.13.: Illustration of the two-ion detector. Ion 1 is immersed in an atom cloud, undergoing collisions. Coupling to ion 2 is indicated by a spring. This auxiliary detection ion is illuminated by two counterpropagating detuned laser beams which create the dark resonance fluorescence spectrum.

The situation, depicted in fig. 5.13, is as follows: Ion 1 is immersed inside an ultracold atom cloud. Next to it in the string is ion 2, whose motional state is being read out by lasers. Due to the inter-ionic coupling via the Coulomb force, motional energy distributes in the string and the auxiliary ion's motion gets excited. Depending on the lasers' wave vectors orientation, their intensities and detunings to the detection transition and relative to each other, different photon-scattering regimes can be entered. Tailoring the fluorescence spectrum used for cooling yields tunable and velocity-dependent scattering rates. Moreover, tailoring a narrow spectrum should allow for cooling to lower temperatures than the Doppler temperature.

Naturally, the two-ion case can be treated in the string's eigenbasis as described in subsec. 2.1.3. Here, we are interested in the radial ionic motion, transversal to the string's elongation. We choose $\hat{\boldsymbol{x}}$ as direction w.l.o.g., and are thus left with two crystal eigenmodes, namely radial COM and stretch mode, cf. tab. 2.2. The stability of this two-ion crystal with regard to trapping stability, and heating due to atom-ion collisions is analysed in sec. 5.3.

In this scenario, three time scales and rates can be introduced, respectively: Firstly, the collision rate between atoms and ion 1, γ_{col}; secondly, the *swapping time* t_{swap} it takes the motional excitation, or to be more precise its change, of ion 1 to be perceptibly transferred to the auxiliary ion 2; thirdly, the time scale for readout τ_{scat} of previously transferred motion, which is determined by the photon scattering rate Γ_{scat} on the detection ion 2:

$$\begin{aligned} \gamma_{\mathrm{col}} &= n\sigma|v_{\mathrm{i}}(t)|\,, \\ \omega_{\mathrm{swap}} := \frac{2\pi}{t_{\mathrm{swap}}} &= \omega_{\mathrm{COM}} - \omega_{\mathrm{s}}\,, \end{aligned} \qquad \Gamma_{\mathrm{scat}} \equiv \Gamma_{\mathrm{scat}}\Big(\{\Gamma_e\},\{\Omega\},\{\delta\},\{v_{\mathrm{i}}\},\{\boldsymbol{k}_{\mathrm{L}}\cdot\boldsymbol{v}_{\text{i-detect}}\}\Big)\,. \tag{5.27}$$

Here, the diverse dependencies of the photon scattering rate on the ion's properties and the employed lasers' charateristics are indicated: The natural width of the involved dipole transitions' excited states, $\{\Gamma_{\mathrm{e}}\}$; the lasers' Rabi frequencies and thus intensities, $\{\Omega\}$; the lasers' detunings relative to each other and to the dipole transition, $\{\delta\}$; the velocities of the immersed and detection ion, $\{v_{\mathrm{i}}\}$, respectively; and last but not least, the orientation of the employed lasers w.r.t. the oscillation direction of the detection ion, $\{\boldsymbol{k}_{\mathrm{L}}\cdot\boldsymbol{v}_{\text{i-detect}}\}$.

Towards informative detection, the photon scattering rate has be to much larger than the atom-ion collision rate. Moreover, if one aims at a single-collision resolution, the time needed for motional transfer has to be much shorter than the average time between two collisions.

$$\Gamma_{\mathrm{scat}} \gg \omega_{\mathrm{swap}} \gg \gamma_{\mathrm{col}} \tag{5.28}$$

Deep in the quantum regime, there is only very little ionic motion. Thus it is of interest to compare the momentum kick by an atom on collision-ion 1 to a momentum kick by a photon on detection-ion 2. Having regard to the statistical determination of the change in motion, i.e. cooling or heating, multiple photons have to scatter from the detection ion. Therefore, their total momentum transfer onto ion 2 has to be small compared to the atomic momentum transfer in consideration of motional perturbation. The momentum kick experienced by ion 2 due to one detection photon is labelled Δp_γ, whereas the one due to a colliding atom is named Δp_a:

$$\Delta p_\gamma = \hbar k \qquad\qquad |\Delta p_{\mathrm{a}}| = (1-\Xi)\cdot p_{\mathrm{i}} \propto p_{\mathrm{i}}\,. \tag{5.29}$$

Here, Δp_γ is independent on the momentum of ion 1, p_i, whereas $|\Delta p_a|$ depends linearly on the latter. Thus, there has to be a crossing of the two momentum transfers as a function of p_i. This is where the ion is so slow that one single scattered photon changes the ionic momentum by more than the initial momentum. Obviously, real-time detection of the atoms cooling ion 1 sympathetically will remain inexecutable then, or even no determination of the motion can be performed at all. The change of the immersed ion's momentum can be written as:

$$\Delta p_{\mathrm{i}} = p_{\mathrm{i}}' - p_{\mathrm{i}} = (\Xi-1)\cdot p_{\mathrm{i}}(t_{\mathrm{col}}) = -2\mu\cdot v_{\mathrm{i}}(t_{\mathrm{col}})\,, \tag{5.30}$$

with momentum transfer factor $\Xi = \frac{m_{\mathrm{i}}-m_{\mathrm{a}}}{m_{\mathrm{i}}+m_{\mathrm{a}}}$ and reduced mass $\mu = \frac{m_{\mathrm{i}}m_{\mathrm{a}}}{m_{\mathrm{i}}+m_{\mathrm{a}}}$. Thus, Ξ is positive and smaller than one for atoms being lighter than ions, $\Xi(m_{\mathrm{a}} \le m_{\mathrm{i}}) \in [0,1[$, where equality to 0 holds for equal masses, $m_{\mathrm{a}} = m_{\mathrm{i}}$.

The quantity of interest is the ion momentum at which the momentum kicks become effectively comparable, which can be extracted by equating the average momentum changes due to atomic collision and photon scattering:

$$\Delta p_\gamma = \Delta p_{\mathrm{a}} \qquad \Rightarrow \qquad p_{\mathrm{i,crit}} = \frac{\hbar k}{1-\Xi}\,. \tag{5.31}$$

This critical ion momentum $p_{\mathrm{i,crit}}$ is the turning point of the impacts' intenseness: Ion momenta exceeding this critical momentum, $p_\mathrm{i} > p_{\mathrm{i,crit}}$, are desirable, since here the detection photon's impact on ion 2 is smaller than the atom's impact on the colliding ion 1, and vice versa. Although the ion string consists of a few particles only and no thermodynamic description is underlying, temperatures are associated with the energies for conception, since it's common practise in physics of ultracold atoms. The critical temperature associated with the critical momentum is given by:

$$T_\mathrm{crit} = \frac{p_\mathrm{crit}^2}{2m_\mathrm{i}k_\mathrm{B}} = T_{\gamma\text{-rec}} \left(\frac{m_\mathrm{i}}{2\mu}\right)^2 = \frac{T_{\gamma\text{-rec}}}{(1-\Xi)^2} \,, \tag{5.32}$$

with $T_{\gamma\text{-rec}} = \frac{\hbar^2 k^2}{2m_\mathrm{i}k_\mathrm{B}}$ being the so-called photon recoil temperature. Alternatively, one can look at the maximal energy changes due to collisions:

$$\Delta E_\mathrm{a} = \frac{(p_\mathrm{i}')^2 - p_\mathrm{i}^2}{2m_\mathrm{i}} = \frac{(\Xi^2-1)p_\mathrm{i}^2}{2m_\mathrm{i}} = -E_\mathrm{i}(1-\Xi^2) \,, \tag{5.33}$$

$$\Delta E_\gamma = \frac{(p_\mathrm{i}+\hbar k)^2 - p_\mathrm{i}^2}{2m_\mathrm{i}} = \frac{(\hbar k)^2}{2m_\mathrm{i}} + 2\frac{\hbar k p_\mathrm{i}}{2m_\mathrm{i}} = k_\mathrm{B}T_{\gamma\text{-rec}} + 2\sqrt{k_\mathrm{B}T_{\gamma\text{-rec}}E_\mathrm{i}} \,. \tag{5.34}$$

This yields the same critical ion energy or temperature, as in (5.32).

For $^{171}\mathrm{Yb}^+$ with a mass of $m_\mathrm{i} = 170.936323\,\mathrm{u}$ and a wavelength of the detection transition $^2\mathrm{S}_{1/2}$–$^2\mathrm{P}_{1/2}$ of 369.419 nm, the photon recoil temperature accounts for $T_{\gamma\text{-rec}} \approx 410.5\,\mathrm{nK}$, cf. tab. A.16. This results in critical temperatures for the Li–Yb^+ and Rb–Yb^+ mixtures, at which the atomic recoil temperature equals the photon recoil temperature: For ^{6}Li & $^{171}\mathrm{Yb}^+$, it amounts to $T_\mathrm{crit} \approx 88.8\,\mu\mathrm{K}$, where $m_{^6\mathrm{Li}} = 6.015121\,\mathrm{u}$, whereas for ^{87}Rb & $^{171}\mathrm{Yb}^+$ it's $T_\mathrm{crit} \approx 903\,\mathrm{nK}$, with $m_{^{87}\mathrm{Rb}} = 86.909180527(13)\,\mathrm{u}$.

Below this critical ion temperature, the disturbing effect of a detection photon is bigger than the quantity one wants to measure, namely the effect of an atom. For higher and higher temperatures above this temperature, more and more photons can be scattered before their influence disturbs the measurement significantly. The lower the critical temperature T_crit, the colder the ions can sympathetically become while still allowing one to observe the cooling process with only little disturbance from the detection photons.

One notices that for the Li–Yb^+-mixture, T_crit is on the order of ytterbium's D1-line Doppler temperature $T_\mathrm{D}(^{171}\mathrm{Yb}^+, \mathrm{D1}) = \frac{\hbar\Gamma}{2k_\mathrm{B}} = 473.2\,\mu\mathrm{K}$, roughly 1/5 (with $\Gamma^{-1} = \tau = 8.07\,\mathrm{ns}$, cf. fig. A.3). For Rb–$\mathrm{Yb}^+$, the critical temperature is far below the Doppler temperature, roughly 1/500. Therefore, multiple photons can scatter the detection ion before the change in its energy becomes comparable to the impact of an Rb atom colliding with the Yb^+ ion immersed in an atomic Rb cloud. Consequently, the Rb–Yb^+-mixture could in principle enable real-time detection of sympathetic cooling down to way lower ion temperatures compared to the Li–Yb^+-mixture. This is why the stability diagrams have been simulated for Rb and not Li as atom species. In the interest of observing the impact of individual colliding lithium atoms onto Yb^+ ions in the interesting regime below the Doppler temperature, one has to think of another method than this two-ion detector scheme. Here, e.g. methods based on quantum logic may be employed [131].

5.4.2. Exploit Dark Resonance

As mentioned previously, the linewidth of the used resonance sets a limit to the laser cooling capability, mainly due to residual photon scattering. The Doppler cooling limit is set by the compensation of a velocity dependent cooling rate by a heating rate. Thus, the line

shape of the cooling transition sets the limit. Consequently, the aim is a narrow fluorescence spectrum to achieve low temperatures. For this purpose, a narrow dark resonance can be employed. The fluorescence spectrum of the dark resonance will be obtained as published by Johannes Roßnagel *et al.* in [132]. This fluorescence spectrum can get tailored to ones needs.

For creating a dark resonance, at least a three-level system is required, in contrast to two levels for Doppler cooling. This can be interpreted as a Λ-scheme with two transitions labelled a and b. Determining the dark resonance fluorescence spectrum implies the determination of the temporal evolution of the density matrix. For this purpose, the Lindblad formalism is utilised, since it's capable of handling dissipative processes. The master equation in Lindblad formalism describes the temporal evolution of the density operator $\hat{\rho}$. It incorporates dissipation in terms of the Lindblad operator $\mathcal{L}(\hat{\rho})$ and the off-diagonal matrix elements in the density operator $\hat{\rho}$ represent quantum coherences [23, 132].

$$\frac{\mathrm{d}\hat{\rho}}{\mathrm{d}t} = -\frac{i}{\hbar}\left[\hat{\mathcal{H}}, \hat{\rho}\right] + \mathcal{L}(\hat{\rho})\,. \tag{5.35}$$

The dissipative Lindblad operator accounts for spontaneous decay:

$$\mathcal{L}(\hat{\rho}) = \sum_i \left(C_i \hat{\rho} C_i^\dagger - \frac{1}{2}\left(C_i^\dagger C_i \hat{\rho} + \hat{\rho} C_i^\dagger C_i \right) \right)\,, \tag{5.36}$$

with the transition operators for dissipation along dipole transitions $p \to q$, containing the decay rates Γ_{pq}:

$$C_i = \sqrt{\Gamma_{pq}}\,|q\rangle\,\langle p|\,. \tag{5.37}$$

Additionally, the lasers' linewidths Γ_a and Γ_b and phase fluctuations between atomic state and laser are introduced by an additional broadening of the corresponding atomic level $|q\rangle$:

$$C_\mathrm{a,b} = \sqrt{\Gamma_\mathrm{a,b}}\,|q\rangle\,\langle q|\,. \tag{5.38}$$

where $\Gamma_\mathrm{a,b}$ are the linewidths of the laser used for transition a or b, respectively.

One obtains the fluorescence spectrum from the steady state solution $\dot{\hat{\rho}} = 0$. The density matrix $\hat{\rho}$ has $N \times N$ entries where N is the number of atomic levels involved, here $N = 3$. The Lindblad operator can then be written in matrix form:

$$\frac{\mathrm{d}\rho_i}{\mathrm{d}t} = \sum_{i=1}^{N^2} L_{ik}\rho_k = 0\,, i \in \left\{1 \ldots N^2\right\}\,. \tag{5.39}$$

Normalisation of $\hat{\rho}$ gives an additional condition, $\mathrm{Tr}(\hat{\rho}) = 1$. The steady state solution is then obtained by solving (5.39) using numerical matrix inversion.

In [132], 8 atomic levels are taken into account which result from lifted degeneracy of the three levels of the Λ-scheme. In contrast, the degeneracy of the magnetic sub-levels will not be lifted here. Consequently, only three levels are involved and no magnetic field has to be applied. Thus, when arranging the Hamiltonian one does not have to be concerned about Zeeman shifts of the magnetic sub-levels:

$$\hat{\mathcal{H}} = \begin{pmatrix} \Delta_\mathrm{a} & \Omega_\mathrm{a} & 0 \\ \Omega_\mathrm{a} & 0 & \Omega_\mathrm{b} \\ 0 & \Omega_\mathrm{b} & \Delta_\mathrm{b} \end{pmatrix}\,, \tag{5.40}$$

with the laser detunings from the corresponding transition $\Delta_a = \omega_{1-2} - \omega_a$ and $\Delta_b = \omega_{3-2} - \omega_b$, from states 1 to 2 and 3 to 2, and the corresponding Rabi frequencies $\Omega_{a,b}$.

We assume the two lasers to be counterpropagating, since in this alignment the fluorescence rate has the strongest sensitivity on the ion's temperature [132]. In contrast to [132], the steady state solution is obtained by fixing both laser detunings as well as their relative detuning and varying the detuning that originates from the opposing Doppler shifts. For this, the Rabi frequencies of the two transitions have to be fixed. Their value is determined by the saturation parameter of the respective transition.

An example of the simulated dark resonance fluorescence spectrum is displayed in fig. 5.14. The most important difference to a common fluorescence spectrum of a two-level system is the dip. Here, the two-photon transition is resonant resulting in no fluorescent light. The ion's Doppler shift has to lie within this dip to benefit from the dark resonance being so narrow.

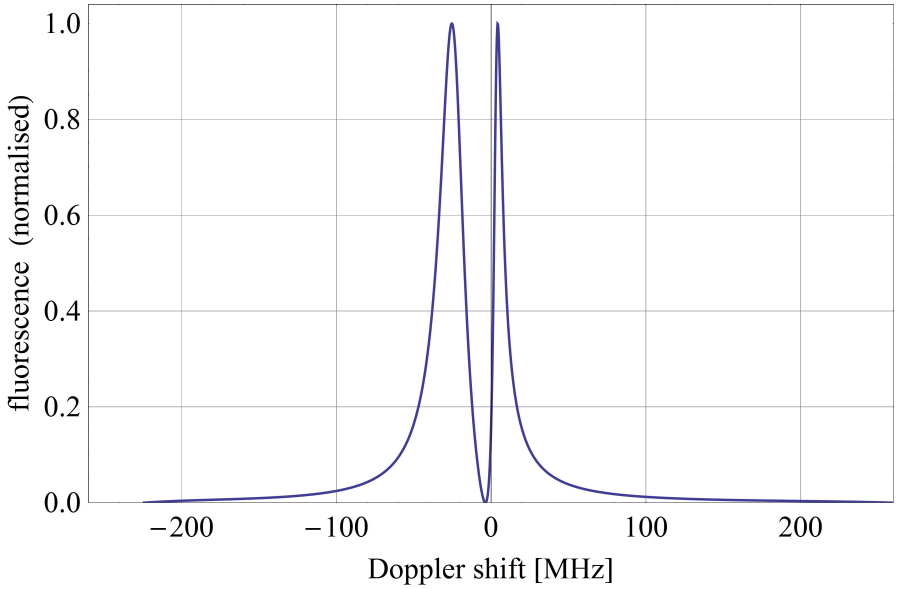

Figure 5.14.: Exemplary dark resonance fluorescence spectrum. The Doppler shift of the illuminated ion has to lie within the dip to benefit from the dark resonance being narrow compared to a two-level fluorescence spectrum.

For a single Yb^+ ion, the energy dependence of the dark resonance fluorescence rate is determined in a similar fashion as described in [133]. In contrast to the Lorentzian emission profile of a two-level system used in [133] to investigate fluorescence during Doppler cooling of a single trapped ion, we employ the dark resonance fluorescence spectrum. The result is shown in fig. 5.15. In the interesting temperature range around and especially below the Doppler temperature of $^{171}Yb^+$, $T_D = 473.2\,\mu K$, the scattering rate exhibits its strongest dependence on the energy. Moreover, the dark resonance fluorescence rate depends much stronger on the temperature than the fluorescence rate of a common Lorentzian emission profile, cf. [133].

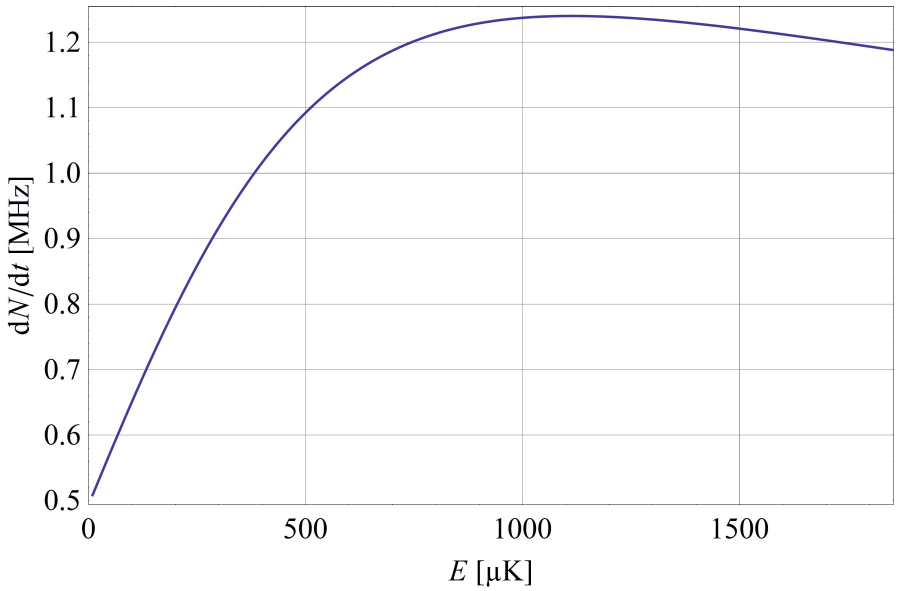

Figure 5.15.: Energy dependence of the photon scattering rate for a single-ion dark resonance.

Consequently, it looks promising that we will be able to measure the ion's temperature with the help of the dark resonance. Additionally, first simulations suppose that the narrow fluorescence spectrum of a dark resonance should enable cooling of the ion crystal. It remains to be analysed whether the sympathetic atom-ion detection benefits from the exploitation of a dark resonance.

Chapter 6

Outlook

As for now, the experiment has reached the following status: The vacuum system containing the installed hard-ware trap components is being baked out. All lasers, except for the Raman and dipole trap laser, have been installed. As soon as the ion trap is ready for operation, my home-made photoionisation laser will be tested thoroughly. Its tuneability by means of current, temperature and cavity length should enable efficient isotope-selective ionisation. Similarly, the effectiveness of the re-repumper has to be investigated. The home-made lasers exhibit some space for improvement, e.g., the usage of an achromatic prism pair to round the beam profile and the choice of another feedback grating for the re-repumper. Here, a grating for optimal Littrow configuration—and thus mode-locking—should have a grating constant of $g = 2214$ mm^{-1}, instead of the currently built-in $g = 2400$ mm^{-1}. The deviation for the photoionisation laser is comparatively small.

Regarding the atomic part of the experiment, the next step consists of completing the Zeeman slower. Previsionally, the number of windings of the coils is made flexible so that last-minute adjustments may be done. Afterwards, the high-power ytterbium fibre laser creating the cODT will have to be installed. For proper imaging, a high-resolution objective has to be designed. Most probably, a simple aspheric lens with a large numerical aperture will be employed. Moreover, an auxiliary optical path with a higher effective magnification is needed to image the ions and atoms alternatively on the EMCCD camera. Furthermore, the cameras are to be tested, and data aquisition and analysis have to be implemented into the Master-Control-Program.

Concerning simulations on hybrid atom-ion interactions, a quantum model of micromotion [60] may get implemented. Moreover, a two- or three-dimensional description might change the picture slightly. The proposed two-ion detector, i.e. the immersion of an ion into the ultracold atom cloud and sympathetic detection of the latter via an auxiliary ion, will be one of the first realisable hybrid experiments on our apparatus. It remains to be analysed thoroughly, whether the usage of the tailored narrow dark resonance fluorescence spectrum allows for real-time detection of the neutral-ion sympathetic cooling. In general, my simulations confirm the benefits of the large mass difference of our species. Experimentally feasible trapping parameters should enable hybrid trapping and also neutral-ion sympathetic cooling.

One idea is to replace the quadrupole ion trap by a higher-order multipole, e.g. octupole trap, to reduce the impact of the micromotion [58, 60, 62, 134, 135]. The shape of the potential would drastically reduce the excess kinetic energy within the micromotion that causes heating to the atoms. Another suggestion is to make use of the high interaction strength, $\propto n^7$, of Rydberg atoms. In this situation, the interaction between the atoms and ions could be more long-range, preventing collisions that may cause heating of the hybrid atom-ion quantum system.

Appendix

Properties of Atomic and Ionic Species to be Used and Akin Ones

A.1. Properties of Lithium

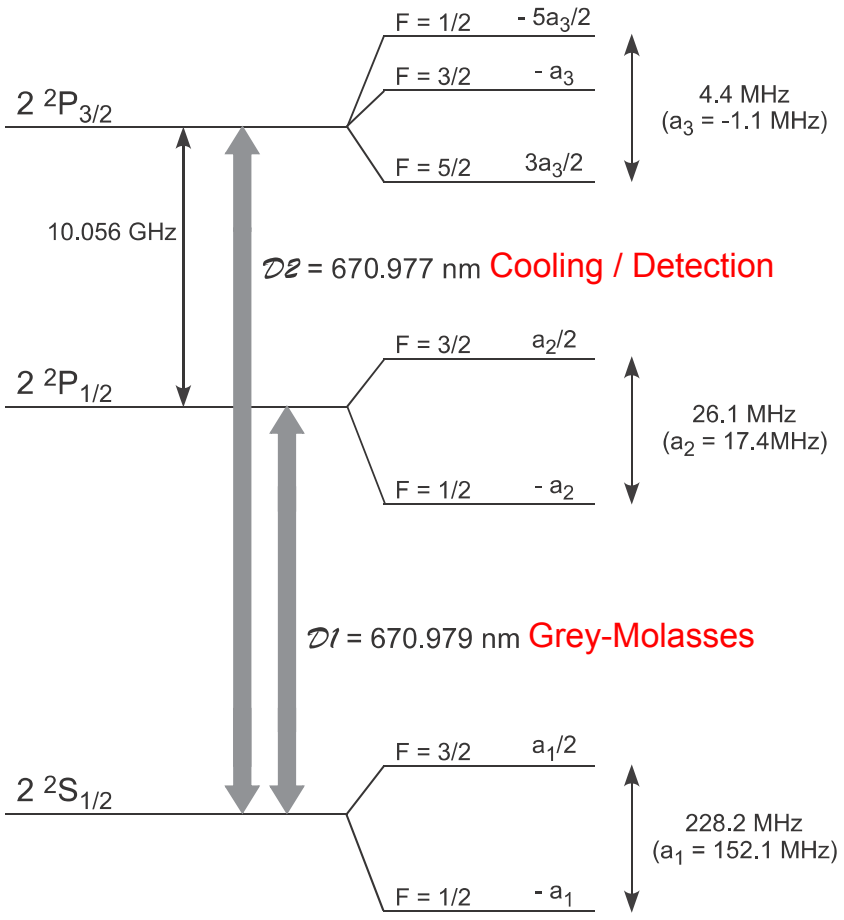

Figure A.1.: Energy level scheme of ^{6}Li with wavelengths and tasks of the dipole transitions D1 and D2. The D2 transition is used for Doppler-cooling in the mMOT and Zeeman slower, while the D1 transition is used for sub-Doppler grey-molasses cooling. The two D-lines are separated by a fine structure splitting of 10.056 GHz, corresponding to a difference in wavelength of approximately 0.002 nm. Energy splittings are not to scale and the diagram originated from [125, 126].

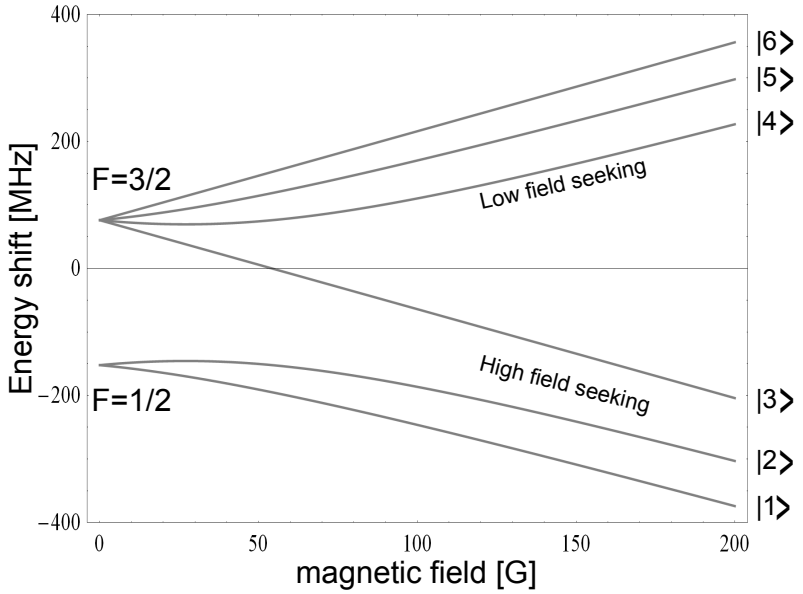

Figure A.2.: Energy shifts of ^{6}Li's magnetic hyperfine sub-levels due an to external magnetic field in the Zeeman and Paschen-Back regime. State $|6\rangle$ is populated for magnetic levitation from the mMOT to the cODT, whereas a $|1\rangle$–$|2\rangle$-mixture is used for evaporative cooling.

Property	Symbol	Quantity for ^{6}Li	Quantity for ^{7}Li	Ref.
atomic number	Z	3	3	
nucleons	A	6	7	
natural abundance	η	7.5(1)%	92.5(1) %	[136, 137]
nuclear lifetime	$t_{1/2}$	stable	stable	[136, 137]
atomic mass	m	6.015121 u $= 9.98834 \cdot 10^{-27}$ kg	7.016003 u $= 1.165035 \cdot 10^{-26}$ kg	[136]
total electronic spin	S	$\frac{1}{2}$	$\frac{1}{2}$	[136]
total nuclear spin	I	1	$\frac{3}{2}$	[136]
magnetic moment	μ	+0.822056	+3.25644	[136]

Table A.1.: Physical properties of atomic ^{6}Li and ^{7}Li.

Property	Symbol	Value	Ref.
density (@ 300 K)	ρ	0.534 g cm^{-3}	[137]
crystal structure		bcc	[137]
melting point	T_M	453.69 K	[137]
heat of fusion	Q_F	2.99 kJ mol^{-1}	[137]
boiling point	T_B	1615 K	[137]
heat of vaporisation	Q_V	134.7 kJ mol^{-1}	[137]

Table A.2.: Physical properties of bulk lithium, $_3$Li.

Property	Symbol	Value	Ref.
wavelength (vac.)	λ_0	670.992421 nm	deduced from [138]
wavelength (air)	λ	670.796548 nm	deduced from [138]
wavenumber (vac.)	$\frac{k}{2\pi}$	14903.298(1) cm^{-1}	[138]
frequency	ν	446.789635(20) THz	[138]
energy	E	1.847773 eV	deduced from [138]
lifetime	τ	27.102(7) ns	[139]
spont. emission rate	$\Gamma = \frac{1}{\tau}$	$36.898 \cdot 10^6\,\mathrm{s}^{-1}$ $2\pi \times 5.8724$ MHz	deduced from [139]
atomic recoil velocity	$v_{\mathrm{rec}} = \frac{p_{\mathrm{rec}}}{m} = \frac{\hbar k}{m}$	9.886554 cm s^{-1}	deduced from [125, 138]
recoil temperature	$T_{\mathrm{rec}} = \frac{m v_{\mathrm{rec}}^2}{2k_B}$	3.53565256 μK	deduced from [125, 138]
saturation intensity	I_{sat}	7.59 mW cm^{-2}	representative [125]

Table A.3.: Optical properties of the D1 transition of atomic ^{6}Li.

Property	Symbol	Value	Ref.
wavelength (vac.)	λ_0	670.977326 nm	deduced from [138]
wavelength (air)	λ	670.781457 nm	deduced from [138]
wavenumber (vac.)	$\frac{k}{2\pi}$	14903.633(1) cm^{-1}	[138]
frequency	ν	446.799685(20) THz	[138]
energy	E	1.847815 eV	deduced from [138]
lifetime	τ	27.102(7) ns $= \tau_{D1}$	[139]
spont. emission rate	$\Gamma = \frac{1}{\tau}$	$36.898 \cdot 10^6\,\mathrm{s}^{-1}$ $2\pi \times 5.8724$ MHz	deduced from [139]
atomic recoil velocity	$v_{\mathrm{rec}} = \frac{p_{\mathrm{rec}}}{m} = \frac{\hbar k}{m}$	9.886776 cm s^{-1}	deduced from [125, 138]
recoil temperature	$T_{\mathrm{rec}} = \frac{m v_{\mathrm{rec}}^2}{2k_B}$	3.53581152 μK	deduced from [125, 138]
saturation intensity	I_{sat}	2.54 mW cm^{-2}	representative [125]

Table A.4.: Optical properties of the D2 transition of atomic ^{6}Li.

Property	Symbol	Value	Ref.
D1 wavelength (vac.)	λ_0	670.976608 nm	deduced from [138]
D1 wavenumber (vac.)	$\frac{k}{2\pi}$	14903.649(1) cm^{-1}	[138]
D1 frequency	ν	446.800163(20) THz	[138]
D1 energy	E	1.847817 eV	deduced from [138]
D2 wavelength (vac.)	λ_0	670.961528 nm	deduced from [138]
D2 wavenumber (vac.)	$\frac{k}{2\pi}$	14903.984(1) cm^{-1}	[138]
D2 frequency	ν	446.810205(20) THz	[138]
D2 energy	E	1.847858 eV	deduced from [138]

Table A.5.: Transition wavelengths, wavenumbers, frequencies and energies of the D1 and D2 fine structure transitions of ^{7}Li.

Property	Symbol	Value	Ref.
electron spin g-factor	g_S	2.0023193043737	[140]
electron orbital g-factor $L = 1$	g_L	0.99999587	[140]
electronic g-factors	$g_J(2^2\mathrm{S}_{1/2})$	2.0023010(7)	[141]
	$g_J(2^2\mathrm{P}_{1/2})$	0.6668(20)	[141]
	$g_J(2^2\mathrm{P}_{3/2})$	1.335(10)	[141]
total nuclear gyromagnetic ratio	$\gamma_I(^6\mathrm{Li}) = g_I(^6\mathrm{Li})\frac{\mu_\mathrm{N}}{\hbar}$	−0.0004476540(3)	[141]
	$\gamma_I(^7\mathrm{Li}) = g_I(^7\mathrm{Li})\frac{\mu_\mathrm{N}}{\hbar}$	−0.0011822130(6)	[141]
2P fine structure splitting	ΔE_FS	10.053044(91) GHZ	[142]

Table A.6.: Total electronic gyromagnetic g-factors, g_S, g_L, and g_J, nuclear gyromagnetic ratios $\gamma_I = g_I\frac{\mu_\mathrm{N}}{\hbar}$, and 2P fine structure splitting for lithium. Here, $\mu_\mathrm{N} := \frac{e\hbar}{2m_\mathrm{p}}$ is the nuclear magneton, and m_p the proton rest mass.

Property	Symbol	Value	Ref.
$2^2\mathrm{S}_{1/2}$ magnetic dipole constant	$A_{\mathrm{S}_{1/2}}$	152.1368407(20) MHz	[141, 143]
$2^2\mathrm{P}_{1/2}$ magnetic dipole constant	$A_{\mathrm{P}_{1/2}}$	17.386(31) MHz	[142]
$2^2\mathrm{P}_{3/2}$ magnetic dipole constant	$A_{\mathrm{P}_{3/2}}$	−1.155(8) MHz	[141]
$2^2\mathrm{P}_{3/2}$ electric quadrupole constant	$B_{\mathrm{P}_{3/2}}$	−0.10(14) MHz	[141]
$3^2\mathrm{P}_{3/2}$ magnetic dipole constant	$A_{3^2\mathrm{P}_{3/2}}$	−0.41(2) MHz	[141]

Table A.7.: Hyperfine splitting constants for 2S, 2P and $3^2\mathrm{P}_{3/2}$ levels of ^{6}Li.

Property	Symbol	Value	Ref.
$2^2\mathrm{S}_{1/2}$ magnetic dipole constant	$A_{\mathrm{S}_{1/2}}$	401.7520433(5) MHz	[141, 143]
$2^2\mathrm{P}_{1/2}$ magnetic dipole constant	$A_{\mathrm{P}_{1/2}}$	45.914(25) MHz	[142]
$2^2\mathrm{P}_{3/2}$ magnetic dipole constant	$A_{\mathrm{P}_{3/2}}$	−3.055(14) MHz	[141]
$2^2\mathrm{P}_{3/2}$ electric quadrupole constant	$B_{\mathrm{P}_{3/2}}$	−0.221(29) MHz	[141]
$3^2\mathrm{P}_{1/2}$ magnetic dipole constant	$A_{3^2\mathrm{P}_{1/2}}$	13.5(2) MHz	[141]
$3^2\mathrm{P}_{3/2}$ magnetic dipole constant	$A_{3^2\mathrm{P}_{3/2}}$	−0.965(20) MHz	[141]
$3^2\mathrm{P}_{3/2}$ electric quadrupole constant	$B_{3^2\mathrm{P}_{3/2}}$	−0.019(22) MHz	[141]

Table A.8.: Hyperfine splitting constants for 2S, 2P and 3P levels of ^{7}Li.

Property	Symbol	Value	Ref.
^{6}Li $2^2\mathrm{S}_{1/2}$ HFS	$\Delta E_\mathrm{HFS}(2^2\mathrm{S}_{1/2})$	228.164(64) MHZ	[142]
^{6}Li 2P FS	$\Delta E_\mathrm{FS}(^2\mathrm{P}_{1/2}{}^{-2}\mathrm{P}_{3/2})$	10.053044(91) GHZ	[142]
^{7}Li $2^2\mathrm{S}_{1/2}$ HFS	$\Delta E_\mathrm{HFS}(2^2\mathrm{S}_{1/2})$	803.534(77) MHZ	[142]
^{7}Li 2P FS	$\Delta E_\mathrm{FS}(^2\mathrm{P}_{1/2}{}^{-2}P_{3/2})$	10.05237(11) GHz	[142]
isotope shift (D1)		10.53426(13) GHz	[142]

Table A.9.: Fine structure, hyperfine structure splittings and isotope shift of ^{6}Li and ^{7}Li.

Property		Symbol	Value	Ref.
$2^2S_{1/2}$	scalar polarisability	$\alpha_0(S_{1/2})$	$0.0408\,\mathrm{Hz/(V/cm)^2}$	[144]
$2^2P_{1/2}$		$\alpha_0(P_{1/2})$	$0.03156\,\mathrm{Hz/(V/cm)^2}$	[145]
$2^2P_{3/2}$		$\alpha_0(P_{3/2})$	$0.03163\,\mathrm{Hz/(V/cm)^2}$	[145]
$2^2P_{3/2}$	tensor polarisability	$\alpha_2(P_{3/2})$	$0.000406\,\mathrm{Hz/(V/cm)^2}$	[145]

Table A.10.: D transition polarisabilities of ^{6}Li.

s-wave scattering length	Symbol	Value [a_0]	Ref.
^{6}Li singlet	$a_S(^6\mathrm{Li})$	38.75	[125]
		45.5(2.5)	[146]
^{6}Li triplet	$a_T(^6\mathrm{Li})$	-2240	[125]
		$-2160(250)$	[146]
^{7}Li singlet	$a_S(^7\mathrm{Li})$	33(2)	[146]
^{7}Li triplet	$a_T(^7\mathrm{Li})$	$-27.6(0.5)$	[146]
^{6}Li & ^{7}Li singlet	$a_S(^6\mathrm{Li}$ & $^7\mathrm{Li})$	$-20(10)$	[146]
^{6}Li & ^{7}Li triplet	$a_T(^6\mathrm{Li}$ & $^7\mathrm{Li})$	40.9(0.2)	[146]

Table A.11.: Singlet and triplet s-wave scattering lengths, a_S and a_T, respectively, in units of Bohr radii a_0 for isotopically pure and mixed gases of Li.

A.2. Properties of Ytterbium

Isotope	Mass [u]	Abundance	Spin	Magnetic moment [μ_N]	Ref.
^{171}Yb	170.936323	14.3 %	$\frac{1}{2}$ (fermionic)	+0.4919	[136]
^{172}Yb	171.936378	21.9 %	0 (bosonic)		[136]
^{173}Yb	172.938208	16.12 %	$\frac{5}{2}$ (fermionic)	-0.6776	[136]
^{174}Yb	173.938859	31.8 %	0 (bosonic)	-0.6776	[136]

Table A.12.: Selected $_{70}$Yb isotopes. Masses are given in unified atomic mass unit, $1\,\mathrm{u} = 1.660538921(73)\cdot10^{27}$ kg. The natural isotope abundance, their spin and magnetic moment are given, the latter in units of the nuclear magneton μ_N.

Property	Symbol	Value	Ref.
density @ r.t.	ρ	$6.973\,\mathrm{g\,cm^{-3}}$	[136]
crystal structure		fcc	[136]
phase @ r.t.		solid	[136]
melting point	T_M	824 °C	[136]
boiling point	T_B	1196 °C	[136]
magnetic ordering		paramagnetic	[136]

Table A.13.: Phyical properties of bulk ytterbium, $_{70}$Yb.

Property	Symbol	Value	Ref.
Ground Shells	$[Xe]4f^{14}6s^2$	$(1s^22s^22p^63s^23p^63d^{10}4s^24p^64d^{10}5s^25p^6)4f^{14}6s^2$	[147]
Ground State	$^1S_0$		[147]
Ionized Level	$6s^2\ S_{1/2}$		[147]
Ionization Energy		6.254159(12) eV	[147]

Table A.14.: Atomic properties of ^{171}Yb.

A of isotopes	isotope shift [MHz]	Ref.
168–170	697.7	[148]
170–171	237.5	[148]
171–172	414.0	[149]
172–173	238.7	[149]
173–174	291.2	[149]
174–176	509.4	[149]

Table A.15.: Isotope shifts of neutral atomic ytterbium. Values are given in MHz with respect to the neighbouring isotope with increasing nucleon number A. Measurements performed on the $6s^2\ ^1S_0$–$6s6p\ ^1P_1$ transition of neutral Yb, which is used for photoionisation and has a wavelength of 398.9 nm.

Lower Level	Upper Level	λ [nm]	E [eV]	A_{ki} [$10^8\,s^{-1}$]	Ref.
$^2S_{1/2}$	$^2P_{3/2}$	328.937	3.768156	1.62	[150]
$^2S_{1/2}$	$^2P_{1/2}$	369.419	3.355238	1.23	[150]

Table A.16.: Wavelengths, energies and Einstein coefficients of the two lowest fine structure transitions of $^{171}Yb^+$.

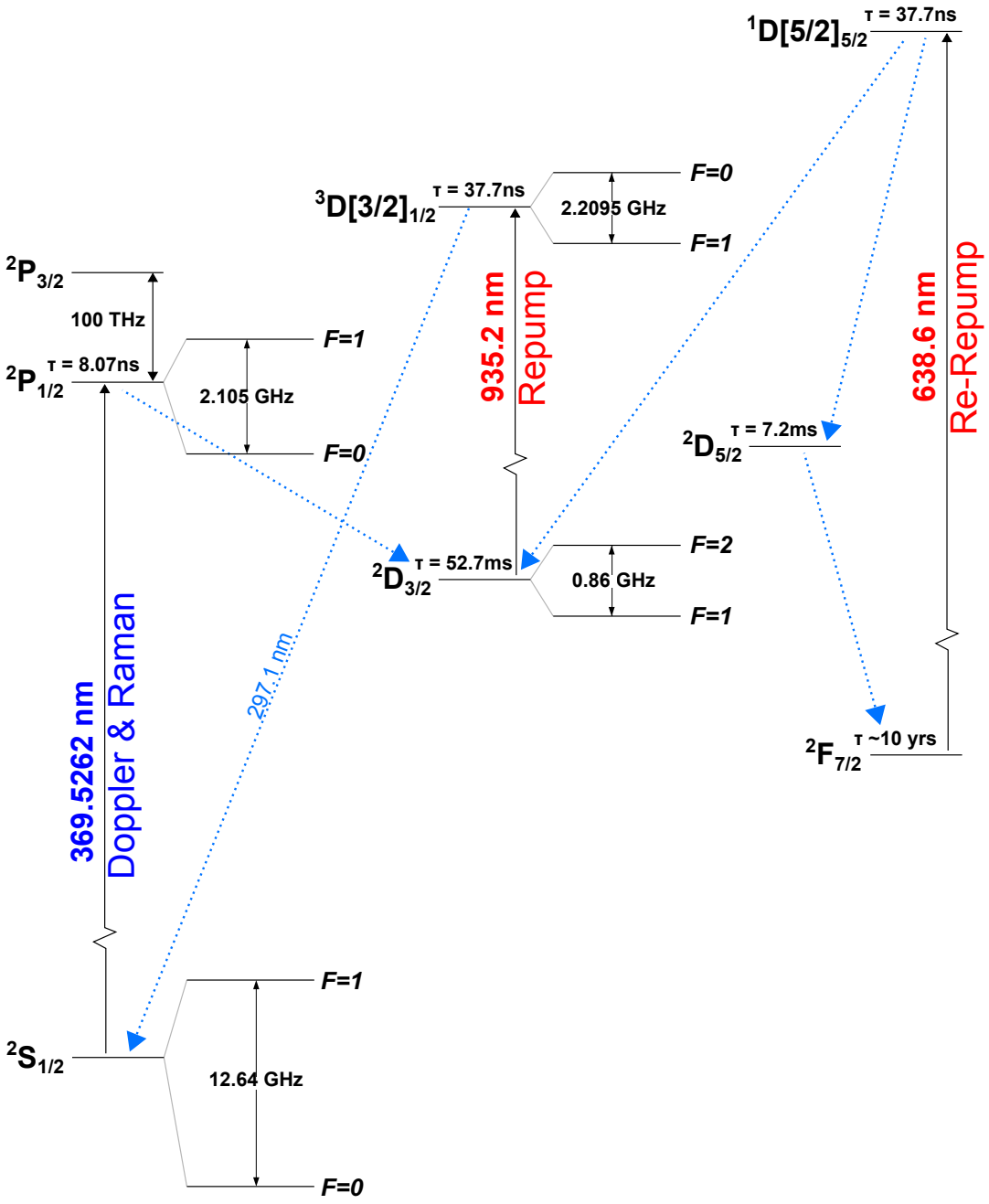

Figure A.3.: Energy level scheme of $^{171}Yb^+$ with wavelengths of electronic transitions and tasks of the individual lasers indicated. [31, 90, 118–121]

A.3. Polarisabilities and Induction Coefficients of Li–Yb-mixtures and Alkali Atoms

Property	Yb^+–Li	Li^+–Yb
C_4^{ind}	82.1	72.0
C_6^{ind}	711.7	1280
C_6^{disp}	711	6.4

Table A.17.: Induction and dispersion coefficients of the interaction potential's long-range part between an Yb^+ ion and a Li atom and between a Li^+ ion and an Yb atom, all in the ground electronic state. All values are given in atomic units (a.u.) and are taken from [59].

Property	Li	Na	K	Rb
α_1 (th.)	164.1(6)	162.4(2)	289.8(6)	318.3(6)
α_1 (th.)	164.112(1) [151]	162.9(6) [152]	289.3 [153]	315.7 [154]
α_1 (exp.)	164.2(1.1) [155]	162.1(8) [156]	290.58(1.42) [157]	318.79(1.42) [157]
C_4	82.1	81.2	144.8	159.9
α_2 (th.)	1426	1895	4947	6491
α_2 (th.)	1424 [158]	1879 [159], 1902 [160]	5000 [161]	6459 [161]
C_6	713	947	2474	3245

Table A.18.: Static dipole α_1 and quadrupole α_2 polarisabilities along with the long-range induction coefficients $C_4 = \frac{\alpha_1}{2}$ and $C_6 = \frac{\alpha_2}{2}$ for the alkali atoms Li, Na, K, and Rb. Values are given in atomic units (a.u.). For comparison, other available polarisability values than the theoretical ones from [162] are listed as theoretical calculations (th.) and experimental results (exp.). Unless noted otherwise in square brackets, all quantities are taken from [162].

A.4. Characteristic Energy and Length Scales for Various Atom-Ion Combinations

Atom	Ion	Mass ratio $\frac{m_i}{m_a}$	E^*/h (kHz)	E^*/k_B (μK)	R^* (nm)	References
^{6}Li	$^{174}Yb^+$	28.92	178.583	8.57	69.77	[163]
	$^{171}Yb^+$	28.42	178.793	8.58	69.75	
	$^{138}Ba^+$	22.93	181.716	8.72	69.46	
	$^{88}Sr^+$	14.61	190.459	9.14	68.65	
	$^{40}Ca^+$	6.64	220.851	10.60	66.16	
	$^{24}Mg^+$	3.99	261.022	12.53	63.45	
	$^{9}Be^+$	1.50	463.888	22.26	54.95	
^{7}Li	$^{174}Yb^+$	24.79	132.705	6.37	75.15	[164]
	$^{171}Yb^+$	24.36	132.885	6.38	75.12	
	$^{138}Ba^+$	19.66	135.407	6.5	74.77	
	$^{88}Sr^+$	12.53	142.967	6.86	73.76	
	$^{40}Ca^+$	5.70	169.446	8.13	70.69	
	$^{24}Mg^+$	3.42	204.838	9.83	67.41	

	$^{9}Be^{+}$	1.28	387.835	18.61	57.47	
^{23}Na	$^{174}Yb^{+}$	7.57	14.760	0.708	129.85	[156, 165]
	$^{171}Yb^{+}$	7.44	14.820	0.711	129.72	
	$^{138}Ba^{+}$	6.00	15.674	0.752	127.92	
	$^{88}Sr^{+}$	3.82	18.326	0.879	123.02	
	$^{40}Ca^{+}$	1.74	28.575	1.37	110.09	
	$^{24}Mg^{+}$	1.04	44.169	2.12	98.73	
^{39}K	$^{174}Yb^{+}$	4.46	3.327	0.160	218.46	[166]
	$^{171}Yb^{+}$	4.39	3.348	0.161	218.11	
	$^{138}Ba^{+}$	3.54	3.652	0.175	213.42	
	$^{88}Sr^{+}$	2.26	4.625	0.221	201.19	
	$^{40}Ca^{+}$	1.026	8.661	0.415	171.98	
^{40}K	$^{174}Yb^{+}$	4.35	3.235	0.155	219.24	[167]
	$^{171}Yb^{+}$	4.27	3.257	0.156	218.88	
	$^{138}Ba^{+}$	3.45	3.559	0.171	214.08	
	$^{88}Sr^{+}$	2.20	4.526	0.217	201.59	
	$^{40}Ca^{+}$	1.00	8.558	0.411	171.92	
^{87}Rb	$^{174}Yb^{+}$	2.00	0.924	0.044	307.23	[137, 165]
	$^{171}Yb^{+}$	1.97	0.935	0.045	306.33	
	$^{138}Ba^{+}$	1.59	1.092	0.052	294.67	
	$^{88}Sr^{+}$	1.01	1.624	0.078	266.80	
^{133}Cs	$^{174}Yb^{+}$	1.31	0.435	0.021	392.67	[165, 168]
	$^{171}Yb^{+}$	1.29	0.442	0.021	391.19	
	$^{138}Ba^{+}$	1.04	0.539	0.026	372.18	
^{172}Yb	$^{174}Yb^{+}$	1.01	0.917	0.044	252.49	[58]
$^{3}He^{*}$	$^{174}Yb^{+}$	57.67	357.285	17.14	69.07	[169]
	$^{171}Yb^{+}$	57.68	357.499	17.16	69.06	
	$^{138}Ba^{+}$	45.72	360.475	17.30	68.92	
	$^{88}Sr^{+}$	29.14	369.304	17.72	68.51	
	$^{40}Ca^{+}$	13.25	399.283	19.16	67.18	
	$^{24}Mg^{+}$	7.95	437.486	21.00	65.66	
	$^{9}Be^{+}$	2.99	614.929	29.51	60.31	
$^{4}He^{*}$	$^{174}Yb^{+}$	43.46	205.130	9.84	79.35	[169]
	$^{171}Yb^{+}$	42.71	205.293	9.85	79.34	
	$^{138}Ba^{+}$	34.45	207.549	9.96	79.12	
	$^{88}Sr^{+}$	21.96	214.262	10.28	78.49	
	$^{40}Ca^{+}$	9.98	237.236	11.39	76.52	
	$^{24}Mg^{+}$	5.99	266.883	12.81	74.30	
	$^{9}Be^{+}$	2.25	408.774	19.61	66.79	
^{24}Mg	$^{174}Yb^{+}$	7.25	31.284	1.50	87.54	[170]
	$^{171}Yb^{+}$	7.13	31.417	1.51	87.45	
	$^{138}Ba^{+}$	5.75	33.297	1.60	86.19	
	$^{88}Sr^{+}$	3.67	39.145	1.88	82.77	
	$^{40}Ca^{+}$	1.66	61.868	2.97	73.82	

	$^{24}Mg^+$	1.00	96.645	4.64	66.03	
^{40}**Ca**	$^{174}Yb^+$	4.35	5.553	0.267	167.35	[171]
	$^{171}Yb^+$	4.28	5.590	0.268	167.08	
	$^{138}Ba^+$	3.45	6.108	0.293	163.41	
	$^{88}Sr^+$	2.20	7.769	0.373	153.87	
	$^{40}Ca^+$	1.00	14.687	0.705	131.23	
^{52}**Cr**	$^{174}Yb^+$	3.35	7.912	0.380	126.37	[137]
	$^{171}Yb^+$	3.29	7.976	0.383	126.12	
	$^{138}Ba^+$	2.66	8.891	0.427	122.74	
	$^{88}Sr^+$	1.69	11.874	0.570	114.18	
^{88}**Sr**	$^{174}Yb^+$	1.98	1.563	0.075	235.35	[137]
	$^{171}Yb^+$	1.94	1.581	0.076	234.65	
	$^{138}Ba^+$	1.57	1.849	0.089	225.66	
	$^{88}Sr^+$	1.00	2.758	0.132	204.18	

Table A.19.: Characteristic energy scales E^* and length scales R^* for various atom-ion combinations with mass ratio $m_\mathrm{i}/m_\mathrm{a} \geq 1$. This table originates from [90].

Appendix

B

Electronics and Circuit Diagrams

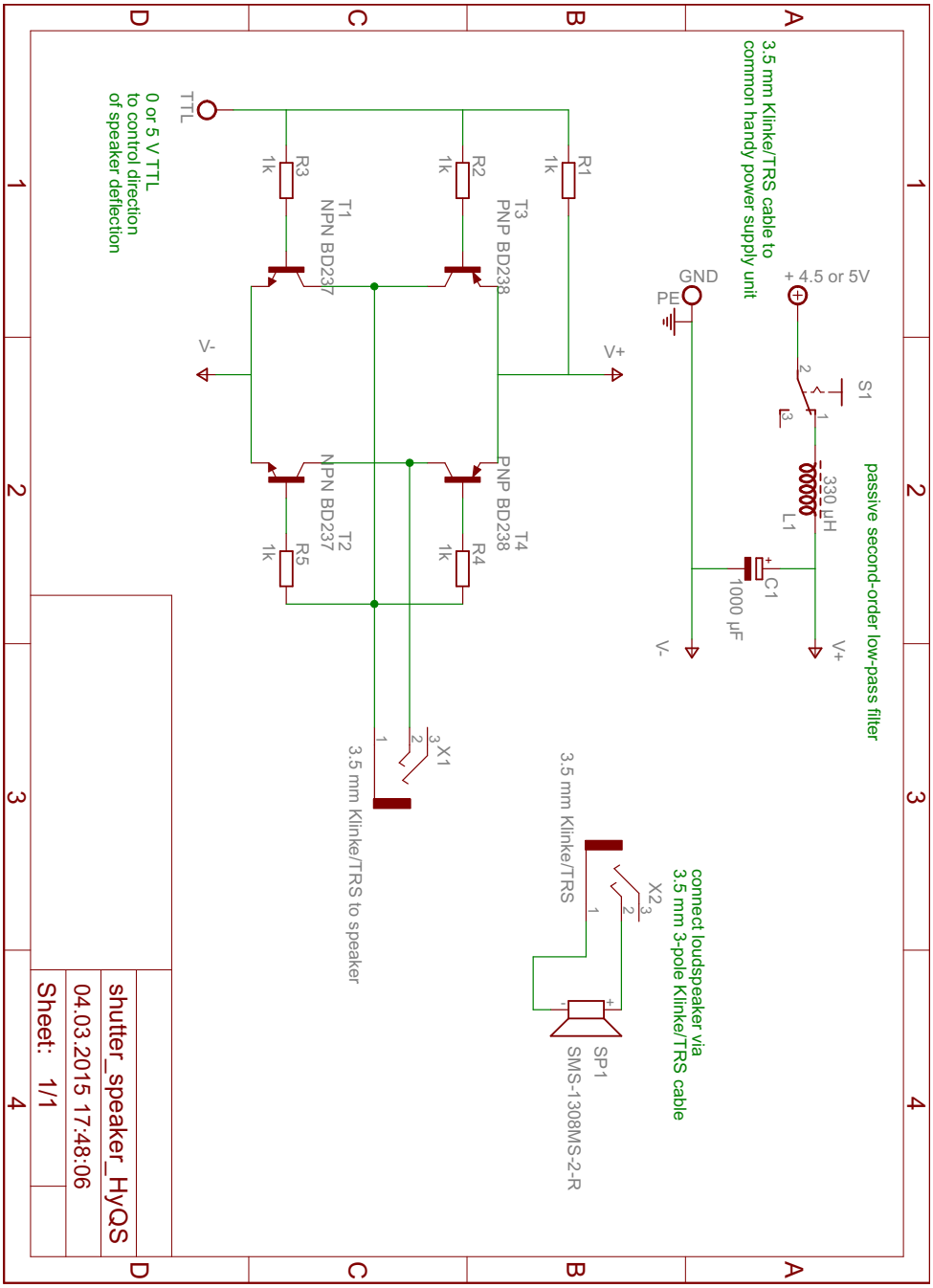

Figure B.1.: Circuit diagram of the optical shutters based on a loudspeaker. The principal control electronics is according to [109] and expanded by a passive 2nd order low-pass filter.

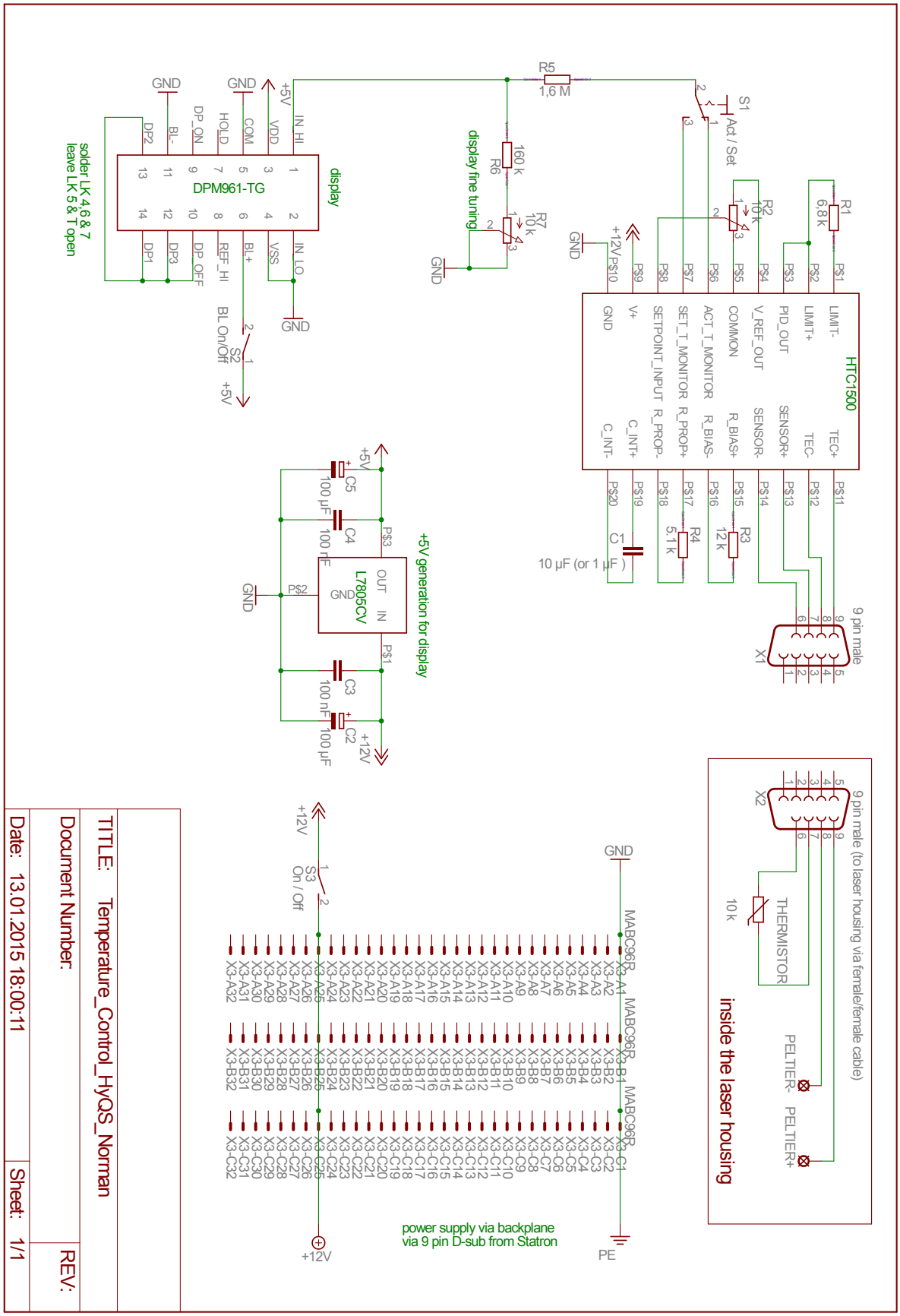

Figure B.3.: Circuit diagram of the home-made diode lasers' temperature stabilisation closed-loop control units.

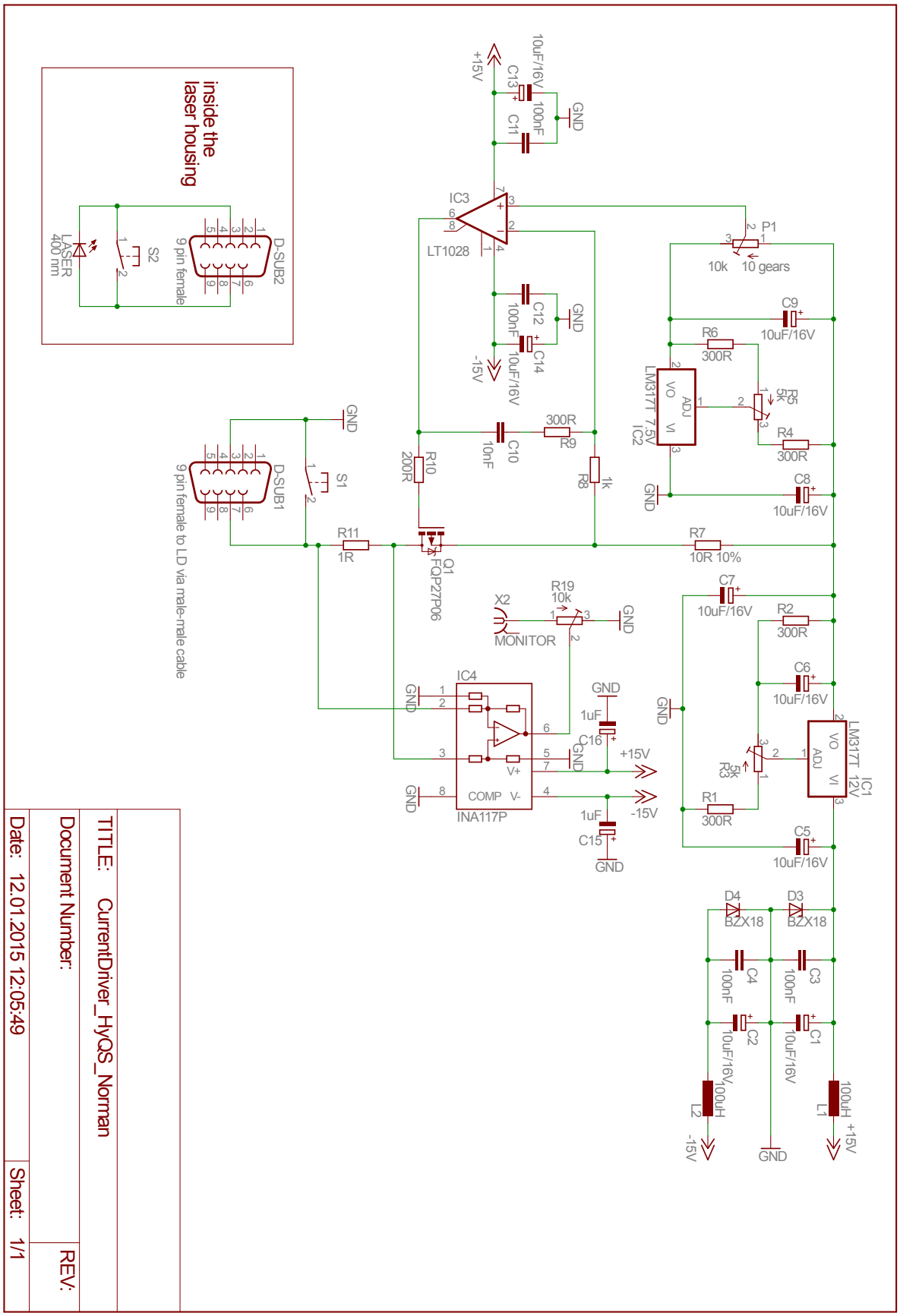

Figure B.2.: Circuit diagram of the home-made diode lasers' current control driver units.

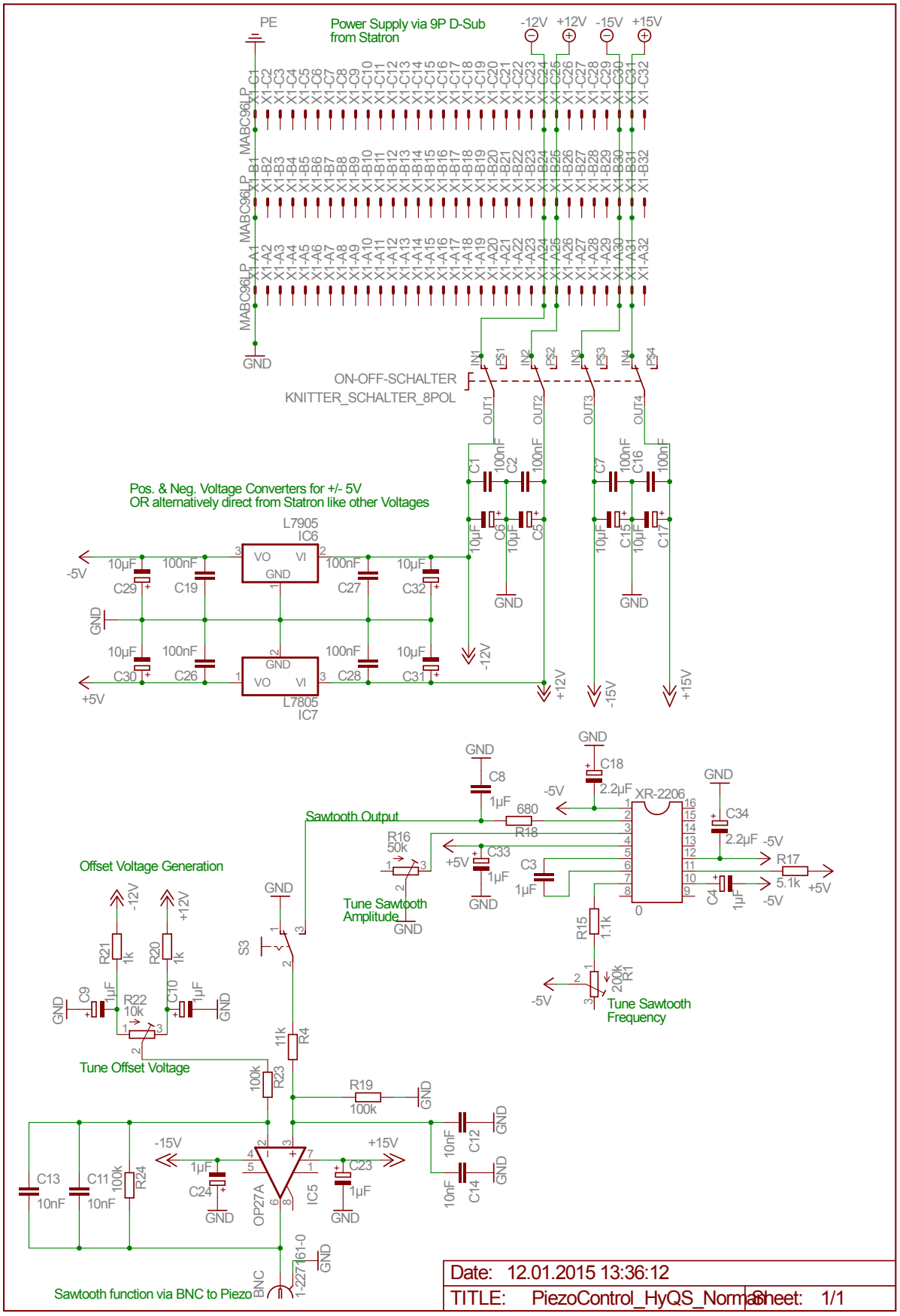

Figure B.4.: Circuit diagram of the home-made diode lasers' piezo element control units.

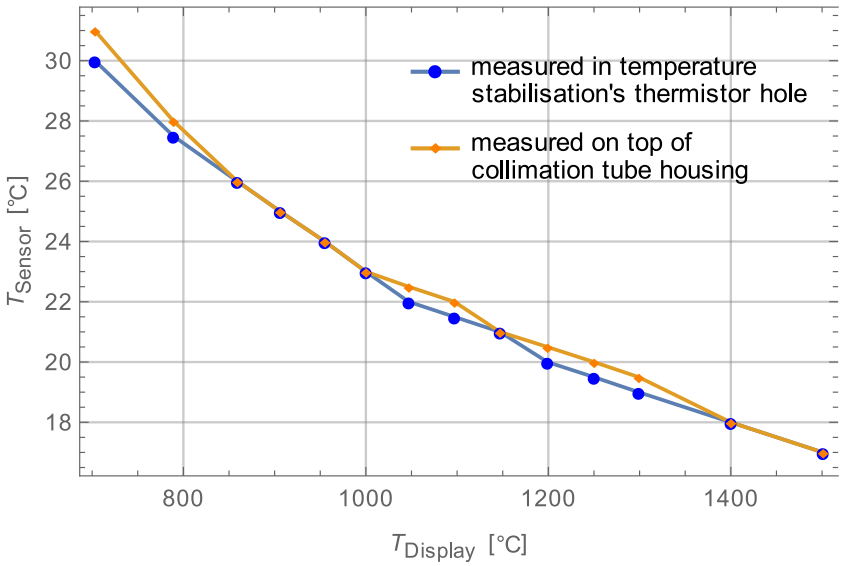

Figure B.5.: Measurements for scaling the displayed temperature T_{Display} of the home-made temperature stabilisations into real temperature T_{Sensor}. Both measurements are performed simultaneously with a digital thermometer, one sensor each inside the hole for the thermistor of the temperature stabilisation, and one on top of the collimation tube mount housing the LD. The ambient temperature was $T_{\text{ambient}} = 21.5\,^{\circ}\text{C}$ according to the air conditioning unit. Digitalisation round-off errors are $\Delta T_{\text{Sensor}} = \pm 0.5\,^{\circ}\text{C}$. For better readability, the error bars are not plotted and the data points are linearly interpolated. Within this statistical measurement error, both sensor spots exhibit the same temperature. Therefore, good thermal equilibration within the diode laser housing can be expected, since the measurement intervals were less than 10 min. Please note, that the deviation of the displayed from the ambient temperature is due to some erroneous connection which results in a different reference voltage for the display, but has no further consequences for the proper functioning of the temperature stabilisation.

Appendix

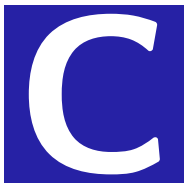

Variables, Constants, Parameters

Quantity	Explanation	Definition
m_i	ionic mass	
m_a	atomic mass	
$\mathfrak{M}_\mathrm{ai}$	atom-ion mass ratio	$\frac{m_\mathrm{a}}{m_\mathrm{i}}$
M	total mass of atom and ion	$M = m_\mathrm{i} + m_\mathrm{a}$
μ	reduced mass	$\mu = \frac{m_\mathrm{i} m_\mathrm{a}}{m_\mathrm{i}+m_\mathrm{a}}$
a	static/DC Mathieu parameter	
q	RF Mathieu parameter	
$\Omega \equiv \Omega_\mathrm{rf}$	ion trap driving radio frequency	
ω_i	ionic secular trap frequencies (for $i \in \{x, y, z\}$)	$\omega_i \approx \frac{\Omega}{2}\sqrt{a_i + \frac{1}{2}q_i^2}$
$\Xi \equiv \Xi(\mathfrak{M}_\mathrm{ai})$	momentum transfer coefficient	$\frac{1-\mathfrak{M}_\mathrm{ai}}{1+\mathfrak{M}_\mathrm{ai}} = \frac{1-m_\mathrm{a}/m_\mathrm{i}}{1+m_\mathrm{a}/m_\mathrm{i}}$
$\Xi(\mathfrak{M}_\mathrm{ai}, \theta)$	2D momentum transfer coefficient	$\frac{\cos(\theta) \pm \sqrt{\cos^2(\theta) - \left(1-{\mathfrak{M}_\mathrm{ai}}^2\right)}}{1+\mathfrak{M}_\mathrm{ai}}$
θ	2D scattering angle	$\arccos\left(\frac{\boldsymbol{p}_\mathrm{i}' \cdot \boldsymbol{p}_\mathrm{i}}{p_\mathrm{i}' p_\mathrm{i}}\right)$
$\boldsymbol{p}_\mathrm{i}$	(pre-collisional) momentum of ion	
$\boldsymbol{p}_\mathrm{i}'$	post-collisional momentum of ion	
e	elementary charge	$1.602176565(35) \cdot 10^{-19}\,\mathrm{C}$
κ		$\frac{1}{4\pi\varepsilon_0}$
α_1	static dipole polarisalibity	
α_2	static quadrupole polarisalibity	
C_4	coefficient for charge-induced dipole interaction	$\kappa^2 e^2 \frac{\alpha_1}{2}$
C_6	coeff. for charge-induced quadrupole interaction	$\kappa^2 e^2 \frac{\alpha_2}{2}$
R^*	characteristic range of atom-ion interaction	$R^* = \sqrt{\frac{2\mu C_4}{\hbar^2}}$
E^*	energy scale of atom-ion interaction	$E^* = \frac{\hbar^2}{2\mu(R^*)^2}$

Table C.1.: Quantities, explanations and definitions of used physical and mathematical variables, constants and parameters.

Appendix D

Acronyms

AC alternating current

AF audio frequency

AOM acousto-optic modulator

BCS Bardeen-Cooper-Schrieffer

BEC Bose-Einstein condensate

cODT crossed optical dipole trap

COM centre of mass

DC direct current

DFG degenerate Fermi gas

DL diode laser

EMCCD electron-multiplying charge-coupled device

EOM electro-optic modulator

e.o.m. equation of motion

GUI graphical user interface

ICCD intensified charge-coupled device

IR infrared

LD laser diode

mBEC molecular Bose-Einstein condensate

MCP Master-Control-Program

mMOT mirror magneto-optical trap

MOSFET metal-oxide-semiconductor field-effect transistor

MOT magneto-optical trap

NDF neutral density filter

NTC thermistor negative temperature coefficient thermal resistor

ODT optical dipole trap

ONB orthonormal basis

PBS polarising beam splitter

PMT photomultiplier tube

RAM random access memory

RF radio frequency

TA tapered amplifier

TSP titanium sublimation pump

TTL transistor-transistor logic

VCO voltage-controlled oscillator

w.l.o.g. without loss of generality

w.r.t. with respect to

Bibliography

[1] A. Härter and J. Hecker Denschlag. "Cold atom-ion experiments in hybrid traps". In: *Contemporary Physics* 55.1 (2014), 33–45. URL: http://dx.doi.org/10.1080/00107514.2013.854618 (cit. on pp. 1, 3 sq., 16).

[2] C. Sias and M. Köhl. "Hybrid quantum systems of ions and atoms". In: *ArXiv e-prints* (2014). arXiv: 1401.3188 [cond-mat.quant-gas] (cit. on p. 1).

[3] A. T. Grier, M. Cetina, F. Oručević, and V. Vuletić. "Observation of Cold Collisions between Trapped Ions and Trapped Atoms". In: *Phys. Rev. Lett.* 102 (2009), 223201. URL: http://link.aps.org/doi/10.1103/PhysRevLett.102.223201 (cit. on p. 1).

[4] S. Schmid, A. Härter, and J. H. Denschlag. "Dynamics of a Cold Trapped Ion in a Bose-Einstein Condensate". In: *Phys. Rev. Lett.* 105 (2010), 133202. URL: http://link.aps.org/doi/10.1103/PhysRevLett.105.133202 (cit. on p. 1).

[5] C. Zipkes, S. Palzer, C. Sias, and M. Köhl. "A trapped single ion inside a Bose–Einstein condensate". In: *Nature* 464 (2010), 388–391. URL: http://www.nature.com/nature/journal/v464/n7287/full/nature08865.html (cit. on p. 1).

[6] S. T. Sullivan. "The MOTion trap: a hybrid atom-ion trap system for experiments in cold-chemistry and the production of cold polar molecular ions". PhD thesis. University of California, Los Angeles, 2013 (cit. on pp. 1, 26).

[7] D. S. Goodman, I. Sivarajah, J. E. Wells, F. A. Narducci, and W. W. Smith. "Ion-neutral-atom sympathetic cooling in a hybrid linear rf Paul and magneto-optical trap". In: *Phys. Rev. A* 86.3 (2012), 033408. arXiv: 1207.1810 [physics.atom-ph] (cit. on pp. 1, 4, 26).

[8] L. Ratschbacher. "Investigation of an Atom-Ion Quantum Hybrid System". PhD thesis. St Catherine's College University of Cambridge, 2013. URL: http://www.quantum.uni-bonn.de/publications/thesis-ratschbacher (cit. on p. 1).

[9] K. Ravi, S. Lee, A. Sharma, G. Werth, and S. Rangwala. "Combined ion and atom trap for low-temperature ion–atom physics". In: *Applied Physics B* 107.4 (2012), 971–981. URL: http://dx.doi.org/10.1007/s00340-011-4726-6 (cit. on p. 1).

[10] S. Jyothi, T. Ray, N. Bhargava Ram, and S. A. Rangwala. "Hybrid ion, atom and light trap". In: *ArXiv e-prints* (2013). arXiv: 1312.2715 [physics.atom-ph]. URL: http://arxiv.org/abs/1312.2715 (cit. on p. 1).

[11] K. Ravi, S. Lee, A. Sharma, G. Werth, and S. A. Rangwala. "Sympathetic and swap cooling of trapped ions by cold atoms in a MOT". In: *ArXiv e-prints* (2011). arXiv: 1112.5825 [physics.atom-ph]. URL: http://arxiv.org/abs/1112.5825 (cit. on pp. 1, 4).

[12] S. Schmid, A. Härter, A. Frisch, S. Hoinka, and J. H. Denschlag. "An apparatus for immersing trapped ions into an ultracold gas of neutral atoms". In: *Review of Scientific Instruments* 83.5 (2012). URL: http://scitation.aip.org/content/aip/journal/rsi/83/5/10.1063/1.4718356 (cit. on p. 1).

[13] S. Haze, S. Hata, M. Fujinaga, and T. Mukaiyama. "Observation of elastic collisions between lithium atoms and calcium ions". In: *Phys. Rev. A* 87.5 (2013), 052715. eprint: 1305.3346 (physics.atom-ph). URL: http://link.aps.org/doi/10.1103/PhysRevA.87.052715 (cit. on p. 1).

[14] L. Ratschbacher et al. "Decoherence of a Single-Ion Qubit Immersed in a Spin-Polarized Atomic Bath". In: *Phys. Rev. Lett.* 110 (2013), 160402. URL: http://link.aps.org/doi/10.1103/PhysRevLett.110.160402 (cit. on p. 1).

[15] A. Härter A.rter et al. "Single Ion as a Three-Body Reaction Center in an Ultracold Atomic Gas". In: *Phys. Rev. Lett.* 109 (2012), 123201. URL: http://link.aps.org/doi/10.1103/PhysRevLett.109.123201 (cit. on p. 1).

[16] J. M. Schurer, P. Schmelcher, and A. Negretti. "Ground-state properties of ultracold trapped bosons with an immersed ionic impurity". In: *Phys. Rev. A* 90 (2014), 033601. URL: http://link.aps.org/doi/10.1103/PhysRevA.90.033601 (cit. on pp. 1, 16).

[17] U. Bissbort et al. "Emulating Solid-State Physics with a Hybrid System of Ultracold Ions and Atoms". In: *Phys. Rev. Lett.* 111 (2013), 080501. URL: http://link.aps.org/doi/10.1103/PhysRevLett.111.080501 (cit. on pp. 1 sqq., 16 sq.).

[18] P. Windpassinger. "Feynmans Idee wird Realität". In: *Physik in unserer Zeit* 45.1 (2014), 26–33. URL: http://dx.doi.org/10.1002/piuz.201301345 (cit. on pp. 1 sq.).

[19] T. H. Johnson, S. R. Clark, and D. Jaksch. "What is a quantum simulator". In: *ArXiv e-prints* (2014). arXiv: 1405.2831 [quant-ph] (cit. on pp. 1 sq.).

[20] T. Schätz, C. R. Monroe, and T. Esslinger. "Focus on quantum simulation". In: *New Journal of Physics* 15.8 (2013), 085009. URL: http://stacks.iop.org/1367-2630/15/i=8/a=085009 (cit. on pp. 1 sq.).

[21] R. P. Feynman. "Simulating physics with computers". In: *International Journal of Theoretical Physics* 21.6-7 (1982), 467–488. URL: http://dx.doi.org/10.1007/BF02650179 (cit. on pp. 1 sq.).

[22] B. M. Boghosian and W. Taylor IV. "Simulating quantum mechanics on a quantum computer". In: *Physica D: Nonlinear Phenomena* 120.1–2 (1998). Proceedings of the Fourth Workshop on Physics and Consumption, 30 –42. URL: http://www.sciencedirect.com/science/article/pii/S0167278998000426 (cit. on p. 1).

[23] K. Singer. "Quantenoptik 1, 2 & Quanteninformation". script of lectures at JGU Mainz during winter term 2012/13 and summer term 2013 (cit. on pp. 1 sq., 12, 42, 49, 69).

[24] R. D. Somma. "Quantum simulations of one dimensional quantum systems". In: *ArXiv e-prints* (2015). arXiv: 1503.06319 [quant-ph] (cit. on p. 2).

[25] C. Monroe et al. "Large-scale modular quantum-computer architecture with atomic memory and photonic interconnects". In: *Phys. Rev. A* 89 (2014), 022317. URL: http://link.aps.org/doi/10.1103/PhysRevA.89.022317 (cit. on p. 2).

[26] W. Paul. *Nobel Lecture, December 8, 1989: ELECTROMAGNETIC TRAPS FOR CHARGED AND NEUTRAL PARTICLES*. Vol. 1981-1990. NOBEL LECTURES PHYSICS. 601-622. World Scientific, 1993. URL: http://www.nobelprize.org/nobel_prizes/physics/laureates/1989/paul-lecture.pdf (cit. on pp. 2 sq., 5 sq.).

[27] G. Werth, F. Schmidt-Kaler, and R. Blatt. "Topical issue Frontiers of ion trap and atomic physics: Wolfgang Paul 100". English. In: *Applied Physics B* 114.1-2 (2014), 1–1. URL: http://dx.doi.org/10.1007/s00340-013-5738-1 (cit. on p. 2).

[28] A. Bermudez et al. "Quantum magnetism of spin-ladder compounds with trapped-ion crystals". In: *New Journal of Physics* 14.9 (2012), 093042. URL: http://stacks.iop.org/1367-2630/14/i=9/a=093042 (cit. on p. 2).

[29] K. Kim et al. "Quantum simulation of frustrated Ising spins with trapped ions". In: *Nature* 465 (2010), 590–593. URL: http://www.nature.com/nature/journal/v465/n7298/full/nature09071.html (cit. on p. 2).

[30] S. Korenblit et al. "Quantum simulation of spin models on an arbitrary lattice with trapped ions". In: *New Journal of Physics* 14.9 (2012), 095024. URL: http://stacks.iop.org/1367-2630/14/i=9/a=095024 (cit. on p. 2).

[31] K. R. Islam. "Quantum Simulation of Interacting Spin Models With Trapped Ions". PhD thesis. University of Maryland, 2012 (cit. on pp. 2, 41, VII).

[32] H. Kaufmann et al. "Precise experimental investigation of eigenmodes in a planar ion crystal". In: *Physical Review Letters* 109 (2012), 263003. URL: http://prl.aps.org/abstract/PRL/v109/i26/e263003 (cit. on pp. 2, 9).

[33] H. Kaufmann. "Experimentelle und theoretische Untersuchung von Zickzack-Ionenkristallen". diploma thesis. JGU Mainz, 2012. URL: http://quantenbit.de/#/publications/phd-and-diploma-theses (cit. on pp. 2, 9).

[34] A. Bermudez, J. Almeida, F. Schmidt-Kaler, A. Retzker, and M. B. Plenio. "Frustrated Quantum Spin Models with Cold Coulomb Crystals". In: *Phys. Rev. Lett.* 107 (2011), 207209. URL: http://link.aps.org/doi/10.1103/PhysRevLett.107.207209 (cit. on p. 2).

[35] R. Nath et al. "Hexagonal Plaquette Spin-spin Interactions and Quantum Magnetism in a Two-dimensional Ion Crystal". In: *ArXiv e-prints* (2015). arXiv: 1504.01474 [cond-mat.quant-gas] (cit. on p. 2).

[36] P. A. Ivanov, D. Porras, S. S. Ivanov, and F. Schmidt-Kaler. "Simulation of the Jahn–Teller–Dicke magnetic structural phase transition with trapped ions". In: *Journal of Physics B* 46 (2013), 104003. URL: http://iopscience.iop.org/0953-4075/46/10/104003/ (cit. on p. 2).

[37] R. Grimm, M. Weidemüller, and Y. B. Ovchinnikov. "Optical Dipole Traps for Neutral Atoms". In: *Advances in Atomic Molecular and Optical Physics* 42 (2000), 95–170. eprint: physics/9902072. URL: http://arxiv.org/abs/physics/9902072 (cit. on pp. 2, 5, 11 sqq.).

[38] F. Serwane et al. "Deterministic Preparation of a Tunable Few-Fermion System". In: *Science* 332.6027 (2011), 336–338. eprint: http://www.sciencemag.org/content/332/6027/336.full.pdf. URL: http://www.sciencemag.org/content/332/6027/336.abstract (cit. on p. 2).

[39] T. Ottenstein. "Few-body physics in ultracold Fermi gases". PhD thesis. Universität Heidelberg, 2010. URL: http://ultracold.physi.uni-heidelberg.de/publications/ (cit. on pp. 2, 48).

[40] A. Wenz. "From Few to Many: Ultracold Atoms in Reduced Dimensions". PhD thesis. Universität Heidelberg, 2013. URL: http://ultracold.physi.uni-heidelberg.de/publications/ (cit. on pp. 2, 13–16, 48 sq.).

[41] M. G. Ries. "A Two-Dimensional Fermi Gas in the BEC-BCS Crossover". PhD thesis. Universität Heidelberg, 2015. URL: http://www.ub.uni-heidelberg.de/archiv/18107 (cit. on p. 2).

[42] S. Pres. "BKT - phase transition in a strongly interacting 2d Bose gas". MA thesis. Physikalisches Institut Heidelberg, 2014 (cit. on p. 2).

[43] P. Windpassinger and K. Sengstock. "Engineering novel optical lattices". In: *Reports on Progress in Physics* 76.8 (2013), 086401. URL: http://stacks.iop.org/0034-4885/76/i=8/a=086401 (cit. on p. 2).

[44] M. Burrello, M. Rizzi, M. Roncaglia, and A. Trombettoni. "Strongly correlated states of trapped ultracold fermions in deformed Landau levels". In: *Phys. Rev. B* 91 (2015), 115117. URL: http://link.aps.org/doi/10.1103/PhysRevB.91.115117 (cit. on p. 2).

[45] U.-J. Wiese. "Towards quantum simulating QCD". In: *Nuclear Physics A* 931 (2014), 246–256. arXiv: 1409.7414 [hep-th] (cit. on p. 2).

[46] U.-J. Wiese. "Ultracold quantum gases and lattice systems: quantum simulation of lattice gauge theories". In: *Annalen der Physik* 525 (2013), 777–796. arXiv: 1305.1602 [quant-ph] (cit. on p. 2).

[47] Y. Kuno, K. Kasamatsu, Y. Takahashi, I. Ichinose, and T. Matsui. "Proposal for feasible experiments of cold-atom quantum simulator of U(1) lattice gauge-Higgs model". In: *ArXiv e-prints* (2014). arXiv: 1412.7605 [cond-mat.quant-gas] (cit. on p. 2).

[48] M. Kurz and P. Schmelcher. "Ultralong-range Rydberg molecules in combined electric and magnetic fields". In: *Journal of Physics B: Atomic, Molecular and Optical Physics* 47.16 (2014), 165101. URL: http://stacks.iop.org/0953-4075/47/i=16/a=165101 (cit. on p. 3).

[49] H. Katiyar, C. S. Sudheer Kumar, and T. S. Mahesh. "Investigation of quantum contextuality in a harmonic oscillator using an NMR quantum simulator". In: *ArXiv e-prints* (2015). arXiv: 1503.05883 [quant-ph] (cit. on p. 3).

[50] Y. Salathé et al. "Digital quantum simulation of spin models with circuit quantum electrodynamics". In: *ArXiv e-prints* (2015). arXiv: 1502.06778 [quant-ph] (cit. on p. 3).

[51] R. Barends et al. "Digital quantum simulation of fermionic models with a superconducting circuit". In: *ArXiv e-prints* (2015). arXiv: 1501.07703 [quant-ph] (cit. on p. 3).

[52] X.-C. Yang, D.-W. Zhang, P. Xu, Y. Yu, and S.-L. Zhu. "Simulating the dynamical quantum Hall effect with superconducting qubits". In: *Phys. Rev. A* 91.2 (2015), 022303. arXiv: 1412.3192 [quant-ph] (cit. on p. 3).

[53] X.-s. Ma et al. "Towards photonic quantum simulation of ground states of frustrated Heisenberg spin systems". In: *Scientific Reports* 4.3583 (2014). URL: http://www.nature.com/srep/2014/140107/srep03583/full/srep03583.html (cit. on p. 3).

[54] J. C. F. Matthews et al. "Observing fermionic statistics with photons in arbitrary processes". In: *Scientific Reports* 3 (2013), 1539. arXiv: 1106.1166 [quant-ph]. URL:

http://www.nature.com/srep/2013/130327/srep01539/full/srep01539.html (cit. on p. 3).

[55] R. G. Newton. *Quantum Physics: A Text for Graduate Students*. Graduate Texts in Contemporary Physics. Springer-Verlag, 2002 (cit. on pp. 3, 13–16).

[56] A. Negretti, R. Gerritsma, Z. Idziaszek, F. Schmidt-Kaler, and T. Calarco. "Generalized Kronig-Penney model for ultracold atomic quantum systems". In: *Phys. Rev. B* 90 (2014), 155426. URL: http://link.aps.org/doi/10.1103/PhysRevB.90.155426 (cit. on p. 3).

[57] M. Rizzi. "Einführung in die Theorie der kondensierten Materie". Personal manuscript of lecture at JGU Mainz during summer term 2014 (cit. on p. 3).

[58] M. Cetina, A. T. Grier, and V. Vuletić. "Micromotion-Induced Limit to Atom-Ion Sympathetic Cooling in Paul Traps". In: *Phys. Rev. Lett.* 109 (2012), 253201. URL: http://link.aps.org/doi/10.1103/PhysRevLett.109.253201 (cit. on pp. 4 sq., 17, 73, IX).

[59] M. Tomza, C. P. Koch, and R. Moszynski. "Cold interactions between an Yb^+ ion and a Li atom: Prospects for sympathetic cooling, radiative association, and Feshbach resonances". In: *ArXiv e-prints* (2014). arXiv: 1409.1192 [physics.atom-ph] (cit. on pp. 4, 17, VIII).

[60] L. H. Nguyên, A. Kalev, M. D. Barrett, and B.-G. Englert. "Micromotion in trapped atom-ion systems". In: *Phys. Rev. A* 85 (2012), 052718. URL: http://link.aps.org/doi/10.1103/PhysRevA.85.052718 (cit. on pp. 4, 8, 73).

[61] D. Lucas and D. Leibfried. "Trapping and cooling of atomic ions". In: *IL NUOVO CIMENTO* (to be publ.). URL: http://static.sif.it/SIF/resources/public/files/va2013/Leibfried-23072.pdf (cit. on pp. 5–8).

[62] R. Wester. "TUTORIAL: Radiofrequency multipole traps: tools for spectroscopy and dynamics of cold molecular ions". In: *Journal of Physics B Atomic Molecular Physics* 42.15 (2009), 154001. arXiv: 0902.0475 [physics.atom-ph] (cit. on pp. 5, 73).

[63] C. Champenois. "About the dynamics and thermodynamics of trapped ions". In: *Journal of Physics B: Atomic, Molecular and Optical Physics* 42.15 (2009), 154002. URL: http://stacks.iop.org/0953-4075/42/i=15/a=154002 (cit. on p. 5).

[64] D. Leibfried, R. Blatt, C. Monroe, and D. Wineland. "Quantum dynamics of single trapped ions". In: *Rev. Mod. Phys.* 75 (2003), 281–324. URL: http://link.aps.org/doi/10.1103/RevModPhys.75.281 (cit. on pp. 5–8, 43).

[65] T. Huber, A. Lambrecht, J. Schmidt, L. Karpa, and T. Schätz. "A far-off-resonance optical trap for a Ba^+ ion". In: *Nature Communications* 5 (2014), 5587. arXiv: 1408.3269 [physics.atom-ph] (cit. on p. 5).

[66] C. Cormick, T. Schätz, and G. Morigi. "Trapping ions with lasers". In: *New Journal of Physics* 13.4 (2011), 043019. URL: http://stacks.iop.org/1367-2630/13/i=4/a=043019 (cit. on p. 5).

[67] D. M. Stamper-Kurn and J. H. Thywissen. "Experimental methods of ultracold atomic physics". In: *ArXiv e-prints* (2011). arXiv: 1111.6196 [cond-mat.quant-gas] (cit. on p. 5).

[68] H. J. Metcalf and P. van der Straten. "Laser cooling and trapping of atoms". In: *J. Opt. Soc. Am. B* 20.5 (2003), 887–908. URL: http://josab.osa.org/abstract.cfm?URI=josab-20-5-887 (cit. on p. 5).

[69] C. Chin, R. Grimm, P. Julienne, and E. Tiesinga. "Feshbach resonances in ultracold gases". In: *Rev. Mod. Phys.* 82 (2010), 1225–1286. URL: http://link.aps.org/doi/10.1103/RevModPhys.82.1225 (cit. on p. 5).

[70] J. C. Maxwell, ed. *A Dynamical Theory of the Electromagnetic Field*. Vol. 13. Proceedings of The Royal Society Of London 1863-1864. 531-536. The Royal Society, London. Proc. R. Soc. Lond., 1863. URL: http://rspl.royalsocietypublishing.org/content/13/531.full.pdf (cit. on p. 5).

[71] S. Earnshaw. "On the Nature of the Molecular Forces which Regulate the Constitution of the Luminiferous Ether". In: *Trans. Camb. Phil. Soc.* 7 (1842), 97–112. URL: https://archive.org/details/cbarchive_36266_onthenatureofthemoleculerforce1833 (cit. on p. 5).

[72] S. T. Gulde. "Experimental Realization of Quantum Gates and the Deutsch-Jozsa Algorithm with Trapped $^{40}Ca^{+}$ Ions". PhD thesis. Universität Innsbruck, 2003. URL: http://heart-c704.uibk.ac.at/publications/dissertation/gulde_diss.pdf (cit. on p. 8).

[73] E. Shimshoni, G. Morigi, and S. Fishman. "Quantum Zigzag Transition in Ion Chains". In: *Physical Review Letters* 106.1 (2011), 010401. arXiv: 1008.2326 [cond-mat.stat-mech] (cit. on p. 9).

[74] S. Fishman, G. De Chiara, T. Calarco, and G. Morigi. "Structural phase transitions in low-dimensional ion crystals". In: *Phys. Rev. B* 77 (2008), 064111. URL: http://link.aps.org/doi/10.1103/PhysRevB.77.064111 (cit. on p. 9).

[75] D. F. V. James. "Quantum dynamics of cold trapped ions with application to quantum computation". In: *Applied Physics B: Lasers and Optics* 66 (1998), 181–190. eprint: quant-ph/9702053 (cit. on pp. 9 sqq.).

[76] H. Landa, M. Drewsen, B. Reznik, and A. Retzker. "Modes of oscillation in radiofrequency Paul traps". In: *New Journal of Physics* 14.9 (2012), 093023. URL: http://stacks.iop.org/1367-2630/14/i=9/a=093023 (cit. on p. 9).

[77] G. Morigi and S. Fishman. "Dynamics of an ion chain in a harmonic potential". In: *Phys. Rev. E* 70 (2004), 066141. URL: http://link.aps.org/doi/10.1103/PhysRevE.70.066141 (cit. on p. 10).

[78] F. Schmidt-Kaler. "Photonik 1 und Physik des Lasers". Personal manuscript of lecture at JGU Mainz during summer term 2013 (cit. on pp. 11 sq., 31, 33, 37, 42, 49).

[79] J.-P. Delahaye. "Die Tücken des Bilderaufhängens". In: *Spektrum der Wissenschaft* 2 (2015). print media, 64–69. URL: www.spektrum.de/artikel/1323150 (cit. on p. 13).

[80] K. Hornberger, S. Gerlich, P. Haslinger, S. Nimmrichter, and M. Arndt. "*Colloquium* : Quantum interference of clusters and molecules". In: *Rev. Mod. Phys.* 84 (2012), 157–173. URL: http://link.aps.org/doi/10.1103/RevModPhys.84.157 (cit. on p. 13).

[81] F. Dalfovo, S. Giorgini, L. P. Pitaevskii, and S. Stringari. "Theory of Bose-Einstein condensation in trapped gases". In: *Rev. Mod. Phys.* 71 (1999), 463–512. URL: http://link.aps.org/doi/10.1103/RevModPhys.71.463 (cit. on p. 13).

[82] S. Giorgini, L. P. Pitaevskii, and S. Stringari. "Theory of ultracold atomic Fermi gases". In: *Rev. Mod. Phys.* 80 (2008), 1215–1274. URL: http://link.aps.org/doi/10.1103/RevModPhys.80.1215 (cit. on p. 14).

[83] M. M. Ali, D. Home, A. S. Majumdar, and A. K. Pan. "Quantum time-of-flight distribution for cold trapped atoms". In: *Phys. Rev. A* 75 (2007), 042110. URL: http://link.aps.org/doi/10.1103/PhysRevA.75.042110 (cit. on pp. 14, 48).

[84] W. Zhang and L.-M. Duan. "Tomography of correlation functions for ultracold atoms via time-of-flight images". In: *Phys. Rev. A* 80 (2009), 063614. URL: http://link.aps.org/doi/10.1103/PhysRevA.80.063614 (cit. on p. 14).

[85] A. Fuhrmanek et al. "Imaging a single atom in a time-of-flight experiment". In: *New Journal of Physics* 12.5 (2010), 053028. URL: http://stacks.iop.org/1367-2630/12/i=5/a=053028 (cit. on pp. 14, 48).

[86] T. Bourdel et al. "Experimental Study of the BEC-BCS Crossover Region in Lithium 6". In: *Phys. Rev. Lett.* 93 (2004), 050401. URL: http://link.aps.org/doi/10.1103/PhysRevLett.93.050401 (cit. on p. 17).

[87] M. Krych and Z. Idziaszek. "Description of ion motion in a Paul trap immersed in a cold atomic gas". In: *ArXiv e-prints* (2013). arXiv: 1312.0279 [cond-mat.quant-gas] (cit. on p. 17).

[88] Z. Idziaszek, T. Calarco, P. S. Julienne, and A. Simoni. "Quantum theory of ultracold atom-ion collisions". In: *Phys. Rev. A* 79 (2009), 010702. URL: http://link.aps.org/doi/10.1103/PhysRevA.79.010702 (cit. on p. 17).

[89] J. Joger. in progress and on same experiment in research group HyQS. PhD thesis (cit. on p. 19).

[90] J. Joger. "Development and characterisation of a combined atom-ion micro trap". diploma thesis. JGU Mainz, 2013. URL: http://quantenbit.de/#/publications/phd-and-diploma-theses (cit. on pp. 19, 31, 41, VII, X).

[91] A. Burchianti et al. "Efficient all-optical production of large ^{6}Li quantum gases using D_1 gray-molasses cooling". In: *ArXiv e-prints* (2014). arXiv: 1406.4788 [cond-mat.quant-gas] (cit. on pp. 20, 26 sq., 49).

[92] M. Chalony, A. Kastberg, B. Klappauf, and D. Wilkowski. "Doppler Cooling to the Quantum Limit". In: *Physical Review Letters* 107.24 (2011), 243002. arXiv: 1107.2313 [physics.atom-ph] (cit. on pp. 20, 42).

[93] T. Ruster. "Schneller Transport von kalten gefangenen Ionen". diploma thesis. JGU Mainz, 2012. URL: http://quantenbit.de/#/publications/phd-and-diploma-theses (cit. on pp. 21 sq.).

[94] F. Serwane. "Deterministic Preparation of a Tunable Few-Fermion System". PhD thesis. 2011. URL: http://ultracold.physi.uni-heidelberg.de/publications/ (cit. on pp. 24, 26).

[95] H. A. Fürst. in progress and on same experiment in research group HyQS. PhD thesis (cit. on pp. 24, 28).

[96] S. Dörscher et al. "Creation of quantum-degenerate gases of ytterbium in a compact 2D-/3D-magneto-optical trap setup". In: *Review of Scientific Instruments* 84.4 (2013), 043109. URL: http://scitation.aip.org/content/aip/journal/rsi/84/4/10.1063/1.4802682 (cit. on p. 26).

[97] T. Kuwamoto, K. Honda, Y. Takahashi, and T. Yabuzaki. "Magneto-optical trapping of Yb atoms using an intercombination transition". In: *Phys. Rev. A* 60 (1999), R745–R748. URL: http://link.aps.org/doi/10.1103/PhysRevA.60.R745 (cit. on pp. 26, 38).

[98] M. Kohnen. "Ultracold Fermi Mixtures in an Optical Dipole Trap". diploma thesis. Universität Heidelberg, 2008 (cit. on p. 28).

[99] A. C. Lee. *Ytterbium Ion Qubit State Detection on an ICCD Camera*. Senior Honors Thesis. 2012. URL: http://iontrap.umd.edu/wp-content/uploads/2013/10/Thesis_2012_AaronLee.pdf (cit. on p. 30).

[100] *EMCCD cameras and EMCCD detectors*. LOT Quantum Design. URL: http://www.lot-qd.de/de/en/home/emccd-detectors/ (cit. on p. 30).

[101] *EMCCD*. ANDOR. URL: http://www.emccd.com/what_is_emccd/ (cit. on p. 30).

[102] *Charge-coupled device*. Wikipedia. URL: http://en.wikipedia.org/wiki/Charge-coupled_device#Electron-multiplying_CCD (cit. on p. 30).

[103] L. Ricci et al. "A compact grating-stabilized diode laser system for atomic physics". In: *Optics Communications* 117.5–6 (1995), 541 –549. URL: http://www.sciencedirect.com/science/article/pii/003040189500146Y (cit. on pp. 31 sq.).

[104] J. Naber. "Aufbau und Betrieb einer Paulfalle zur Rydberganregung von Ionen". diploma thesis. JGU Mainz, 2012. URL: http://quantenbit.de/#/publications/phd-and-diploma-theses (cit. on p. 31).

[105] N. V. Ewald. "Temperaturstabilisierung eines optischen Resonators mittels elektronischer Regelungsschaltung". bachelor thesis. JGU Mainz, 2012. URL: http://www.students.uni-mainz.de/newald/Bachelorarbeit%20Norman%20Ewald.pdf (cit. on p. 34).

[106] Electropaedia. *Semiconductors Without the Quantum Physics - Seebeck and Peltier Effect Thermocouples*. http://www.mpoweruk.com/semiconductors.htm. ONLINE. 2005. URL: http://www.mpoweruk.com/semiconductors.htm (cit. on p. 34).

[107] H. Ibach and H. Lüth. *Festkörperphysik – Einführung in die Grundlagen*. 7th ed. Berlin, Heidelberg: Springer, 2009 (cit. on p. 34).

[108] Quick-Ohm Küpper & Co. GmbH. URL: http://quick-cool.de/peltierelemente/peltierelemente-basisinformation.htm (cit. on p. 35).

[109] K. Singer, S. Jochim, M. Mudrich, A. Mosk, and M. Weidemüller. "Low-cost mechanical shutter for light beams". In: *Review of Scientific Instruments* 73.12 (2002), 4402–4404. URL: http://scitation.aip.org/content/aip/journal/rsi/73/12/10.1063/1.1520728 (cit. on pp. 36 sq., XI).

[110] U. Tietze and C. Schenk. *Halbleiter-Schaltungstechnik*. 11th ed. Berlin, Heidelberg: Spinger, 1999 (cit. on p. 36).

[111] *VISATON SC 4.7 ND speaker*. URL: http://www.visaton.de/en/chassis_zubehoer/breitband/sc4_7nd_8.html (cit. on p. 36).

[112] E. A. Donley, T. P. Heavner, F. Levi, M. O. Tataw, and S. R. Jefferts. "Double-pass acousto-optic modulator system". In: *Review of Scientific Instruments* 76.6 (2005). URL: http://scitation.aip.org/content/aip/journal/rsi/76/6/10.1063/1.1930095 (cit. on pp. 37, 49 sq.).

[113] W. H. Bragg and W. L. Bragg. "The Reflection of X-rays by Crystals". In: *Proceedings of the Royal Society of London A: Mathematical, Physical and Engineering Sciences* 88.605 (1913), 428–438. URL: http://rspa.royalsocietypublishing.org/content/88/605/428 (cit. on p. 37).

[114] M. Johanning et al. "Resonance-enhanced isotope-selective photoionization of YbI for ion trap loading". In: *Applied Physics B: Lasers and Optics* 103 (2011), 327–338. arXiv: 0712.0969 [physics.atom-ph] (cit. on pp. 37 sqq., 44).

[115] P. Camus, A. Débarre, and C. Morillon. "Highly excited levels of neutral ytterbium. I. Two-photon and two-step spectroscopy of even spectra". In: *Journal of Physics B: Atomic and Molecular Physics* 13.6 (1980), 1073. URL: http://stacks.iop.org/0022-3700/13/i=6/a=015 (cit. on p. 37).

[116] J. Migdalek and W. E. Baylis. "Relativistic transition probabilities and lifetimes of low-lying levels in ytterbium". In: *Journal of Physics B: Atomic, Molecular and Optical Physics* 24.4 (1991), L99. URL: http://stacks.iop.org/0953-4075/24/i=4/a=001 (cit. on p. 38).

[117] Y. Takasu et al. "Photoassociation Spectroscopy of Laser-Cooled Ytterbium Atoms". In: *Phys. Rev. Lett.* 93 (2004), 123202. URL: http://link.aps.org/doi/10.1103/PhysRevLett.93.123202 (cit. on p. 38).

[118] S. Rahaman et al. "MW-Optical Double Resonance in $^{171}Yb^{+}$ Trapped Single Ion and its Application for Precision Experiments". In: *ArXiv e-prints* (2013). arXiv: 1304.5732 [physics.atom-ph] (cit. on pp. 41, VII).

[119] S. Olmschenk. "Quantum Teleportation between Distant Matter Qubits". PhD thesis. University of Michigan, 2009 (cit. on pp. 41 sq., VII).

[120] S. Olmschenk et al. "Quantum Teleportation Between Distant Matter Qubits". In: *Science* 323 (2009), 486–. arXiv: 0907.5240 [quant-ph] (cit. on pp. 41, VII).

[121] S. Olmschenk et al. "Manipulation and detection of a trapped Yb^{+} hyperfine qubit". In: *Phys. Rev. A* 76 (2007), 052314. URL: http://link.aps.org/doi/10.1103/PhysRevA.76.052314 (cit. on pp. 41, 45, VII).

[122] R. Chang et al. "Three-dimensional laser cooling at the Doppler limit". In: *Phys. Rev. A* 90.6 (2014), 063407. arXiv: 1409.2519 [physics.atom-ph] (cit. on p. 42).

[123] D. A. Steck. *Rubidium 87 D Line Data*. (revision 2.1.4, 23 December 2010). 2001. URL: http://steck.us/alkalidata (cit. on pp. 42 sq.).

[124] M. Cetina et al. "One-dimensional array of ion chains coupled to an optical cavity". In: *New Journal of Physics* 15.5 (2013), 053001. URL: http://stacks.iop.org/1367-2630/15/i=5/a=053001 (cit. on p. 43).

[125] M. E. Gehm. *Properties of ^{6}Li*. 2003. URL: http://www.physics.ncsu.edu/jet/techdocs/pdf/PropertiesOfLi.pdf (cit. on pp. 46, 49, I, III, V).

[126] M. E. Gehm. "Preparation of an Optically-Trapped Degenerate Fermi Gas of ^{6}Li: Finding the Route to Degeneracy". PhD thesis. Duke University, 2003. URL: http://www.physics.ncsu.edu/jet/theses/pdf/Gehm.pdf (cit. on pp. 46, 49, I).

[127] *NIST Atomic Spectra Database*. URL: http://www.nist.gov/pml/data/asd.cfm (cit. on p. 46).

[128] T. Pyragius. "Developing and building an absorption imaging system for Ultracold Atoms". In: *ArXiv e-prints* (2012). arXiv: 1209.3408 [physics.ins-det] (cit. on p. 48).

[129] A. T. Grier et al. "Λ-enhanced sub-Doppler cooling of lithium atoms in D_1 gray molasses". In: *Phys. Rev. A* 87 (2013), 063411. URL: http://link.aps.org/doi/10.1103/PhysRevA.87.063411 (cit. on p. 49).

[130] C. Zipkes, L. Ratschbacher, C. Sias, and M. Köhl. "Kinetics of a single trapped ion in an ultracold buffer gas". In: *New Journal of Physics* 13.5 (2011), 053020. URL: http://stacks.iop.org/1367-2630/13/i=5/a=053020 (cit. on p. 54).

[131] C. Hempel et al. "Entanglement-enhanced detection of single-photon scattering events". In: *Nature Photonics* 7 (2013), 630–633. URL: http://www.nature.com/nphoton/journal/v7/n8/full/nphoton.2013.172.html (cit. on p. 68).

[132] J. Roßnagel, K. N. Tolazzi, F. Schmidt-Kaler, and K. Singer. "Fast thermometry for trapped ions using dark resonances". In: *New Journal of Physics* 17.4 (2015), 045004. URL: http://stacks.iop.org/1367-2630/17/i=4/a=045004 (cit. on pp. 69 sq.).

[133] J. H. Wesenberg et al. "Fluorescence during Doppler cooling of a single trapped atom". In: *Phys. Rev. A* 76 (2007), 053416. URL: http://link.aps.org/doi/10.1103/PhysRevA.76.053416 (cit. on p. 70).

[134] F. Cartarius, C. Cormick, and G. Morigi. "Stability and dynamics of ion rings in linear multipole traps". In: *Phys. Rev. A* 87.1 (2013), 013425. arXiv: 1211.2931 [physics.atom-ph] (cit. on p. 73).

[135] M. Marciante, C. Champenois, A. Calisti, and M. Knoop. "Structural phase transitions in multipole traps". English. In: *Applied Physics B* 107.4 (2012), 1117–1123. URL: http://dx.doi.org/10.1007/s00340-012-4883-2 (cit. on p. 73).

[136] J. Emsley. *The Elements, Oxford Chemistry Guides*. Oxford Univ. Press, New York, NY, 1995 (cit. on pp. II, V).

[137] W. M. Haynes. *CRC Handbook of Chemistry and Physics*. CRC Press, Boca Raton, Florida. 64th edition. 1983 (cit. on pp. II, IX sq.).

[138] W. Scherf, O. Khait, H. Jäger, and L. Windholz. "Re-measurement of the transition frequencies, fine structure splitting and isotope shift of the resonance lines of lithium, sodium and potassium". English. In: *Zeitschrift für Physik D Atoms, Molecules and Clusters* 36.1 (1996), 31–33. URL: http://dx.doi.org/10.1007/BF01437417 (cit. on p. III).

[139] W. I. McAlexander, E. R. I. Abraham, and R. G. Hulet. "Radiative lifetime of the $2P$ state of lithium". In: *Phys. Rev. A* 54 (1996), R5–R8. URL: http://link.aps.org/doi/10.1103/PhysRevA.54.R5 (cit. on p. III).

[140] P. J. Mohr, B. N. Taylor, and D. B. Newell. "CODATA Recommended Values of the Fundamental Physical Constants: 2010a)". In: *Journal of Physical and Chemical Reference Data* 41.4 (2012). URL: http://scitation.aip.org/content/aip/journal/jpcrd/41/4/10.1063/1.4724320 (cit. on p. IV).

[141] E. Arimondo, M. Inguscio, and P. Violino. "Experimental determinations of the hyperfine structure in the alkali atoms". In: *Rev. Mod. Phys.* 49 (1977), 31–75. URL: http://link.aps.org/doi/10.1103/RevModPhys.49.31 (cit. on p. IV).

[142] J. Walls, R. Ashby, J. Clarke, B. Lu, and W. van Wijngaarden. "Measurement of isotope shifts, fine and hyperfine structure splittings of the lithium D lines". English. In: *The European Physical Journal D - Atomic, Molecular, Optical and Plasma Physics* 22.2 (2003), 159–162. URL: http://dx.doi.org/10.1140/epjd/e2003-00001-5 (cit. on p. IV).

[143] A. Beckmann, K. Böklen, and D. Elke. "Precision measurements of the nuclear magnetic dipole moments of ^{6}Li, ^{7}Li, ^{23}Na, ^{39}K and ^{41}K". English. In: *Zeitschrift für Physik* 270.3 (1974), 173–186. URL: http://dx.doi.org/10.1007/BF01680407 (cit. on p. IV).

[144] R. W. Molof, H. L. Schwartz, T. M. Miller, and B. Bederson. "Measurements of electric dipole polarizabilities of the alkali-metal atoms and the metastable noble-gas atoms". In: *Phys. Rev. A* 10 (1974), 1131–1140. URL: http://link.aps.org/doi/10.1103/PhysRevA.10.1131 (cit. on p. V).

[145] L. Windholz, M. Musso, G. Zerza, and H. Jäger. "Precise Stark-effect investigations of the lithium D_1 and D_2 lines". In: *Phys. Rev. A* 46 (1992), 5812–5818. URL: http://link.aps.org/doi/10.1103/PhysRevA.46.5812 (cit. on p. V).

[146] E. R. I. Abraham et al. "Triplet s-wave resonance in ^{6}Li collisions and scattering lengths of ^{6}Li and ^{7}Li". In: *Phys. Rev. A* 55 (1997), R3299–R3302. URL: http://link.aps.org/doi/10.1103/PhysRevA.55.R3299 (cit. on p. V).

[147] M. Aymar, A. Débarre, and O. Robaux. "Highly excited levels of neutral ytterbium. II. Multichannel quantum defect analysis of odd- and even-parity spectra". In: *Journal of Physics B: Atomic and Molecular Physics* 13.6 (1980), 1089–1109. URL: http://stacks.iop.org/0022-3700/13/i=6/a=016 (cit. on p. VI).

[148] K. Deilamian, J. D. Gillaspy, and D. E. Kelleher. "Isotope shifts and hyperfine splittings of the 398.8-nm Yb I line". In: *J. Opt. Soc. Am. B* 10.5 (1993), 789–793. URL: http://josab.osa.org/abstract.cfm?URI=josab-10-5-789 (cit. on p. VI).

[149] P. Grundevik, M. Gustavsson, A. Rosén, and S. Rydberg. "Analysis of the isotope shifts and hyperfine structure in the 3988 Å ($6s6p\ ^{1}P_1$–$6s^2\ ^{1}S_0$) YbI line". English. In: *Zeitschrift für Physik A Atoms and Nuclei* 292.4 (1979), 307–310. URL: http://dx.doi.org/10.1007/BF01546427 (cit. on p. VI).

[150] D. C. Morton. "Atomic data for resonance absorption lines II. Wavelengths longward of the Lyman limit for heavy elements". In: *Astrophys. J., Suppl. Ser.* 130 (2000), 403–436 (cit. on p. VI).

[151] L.-Y. Tang, Z.-C. Yan, T.-Y. Shi, and J. Mitroy. "Dynamic dipole polarizabilities of the Li atom and the Be^{+} ion". In: *Phys. Rev. A* 81 (2010), 042521. URL: http://link.aps.org/doi/10.1103/PhysRevA.81.042521 (cit. on p. VIII).

[152] A. J. Thakkar and C. Lupinetti. "The polarizability of sodium: theory and experiment reconciled". In: *Chem. Phys. Lett.* 402 (2005), 270 (cit. on p. VIII).

[153] U. I. Safronova, W. R. Johnson, and M. S. Safronova. "Excitation energies, polarizabilities, multipole transition rates, and lifetimes of ions along the francium isoelectronic sequence". In: *Phys. Rev. A* 76 (2007), 042504. URL: http://link.aps.org/doi/10.1103/PhysRevA.76.042504 (cit. on p. VIII).

[154] J. Mitroy and M. W. J. Bromley. "Semiempirical calculation of van der Waals coefficients for alkali-metal and alkaline-earth-metal atoms". In: *Phys. Rev. A* 68 (2003), 052714. URL: http://link.aps.org/doi/10.1103/PhysRevA.68.052714 (cit. on p. VIII).

[155] A. Miffre, M. Jacquey, M. Büchner, G. Trénec, and J. Vigué. "Atom interferometry measurement of the electric polarizability of lithium". In: *Eur. Phys. J. D* 38.2 (2006), 353–365. URL: http://dx.doi.org/10.1140/epjd/e2006-00015-5 (cit. on p. VIII).

[156] C. R. Ekstrom, J. Schmiedmayer, M. S. Chapman, T. D. Hammond, and D. E. Pritchard. "Measurement of the electric polarizability of sodium with an atom interferometer". In: *Phys. Rev. A* 51 (1995), 3883–3888. URL: http://link.aps.org/doi/10.1103/PhysRevA.51.3883 (cit. on pp. VIII sq.).

[157] W. F. Holmgren, M. C. Revelle, V. P. A. Lonij, and A. D. Cronin. "Absolute and ratio measurements of the polarizability of Na, K, and Rb with an atom interferometer". In: *Phys. Rev. A* 81 (2010), 053607. URL: http://link.aps.org/doi/10.1103/PhysRevA.81.053607 (cit. on p. VIII).

[158] S. G. Porsev and A. Derevianko. "Accurate relativistic many-body calculations of van der Waals coefficients C8 and C10 for alkali-metal dimers". In: *The Journal of Chemical Physics* 119.2 (2003), 844–850. URL: http://scitation.aip.org/content/aip/journal/jcp/119/2/10.1063/1.1578052 (cit. on p. VIII).

[159] D. Spelsberg, T. Lorenz, and W. Meyer. "Dynamic multipole polarizabilities and long range interaction coefficients for the systems H, Li, Na, K, He, H–, H2, Li2, Na2, and K2". In: *The Journal of Chemical Physics* 99.10 (1993), 7845–7858. URL: http://scitation.aip.org/content/aip/journal/jcp/99/10/10.1063/1.465663 (cit. on p. VIII).

[160] O. P. Makarov, R. Côté, H. Michels, and W. W. Smith. "Radiative charge-transfer lifetime of the excited state of $(NaCa)^+$". In: *Phys. Rev. A* 67 (2003), 042705. URL: http://link.aps.org/doi/10.1103/PhysRevA.67.042705 (cit. on p. VIII).

[161] M. Marinescu, H. R. Sadeghpour, and A. Dalgarno. "Dispersion coefficients for alkali-metal dimers". In: *Phys. Rev. A* 49 (1994), 982–988. URL: http://link.aps.org/doi/10.1103/PhysRevA.49.982 (cit. on p. VIII).

[162] J. Kaur, D. K. Nandy, B. Arora, and B. K. Sahoo. "Long-range interactions between the alkali-metal atoms and alkaline earth ions". In: *ArXiv e-prints* (2014). arXiv: 1409.7154 [physics.atom-ph] (cit. on p. VIII).

[163] L.-Y. Tang, Z.-C. Yan, T.-Y. Shi, and J. F. Babb. "Nonrelativistic ab initio calculations for 2S2 , 2P2 , and 3D2 lithium isotopes: Applications to polarizabilities and dispersion interactions". In: *Phys. Rev. A* 79.6 (2009), 062712. arXiv: 0905.2110 [physics.atom-ph] (cit. on p. VIII).

[164] A. Miffre, M. Jacquey, M. Büchner, G. Trénec, and J. Vigué. "Measurement of the electric polarizability of lithium by atom interferometry". In: *Phys. Rev. A* 73.1 (2006), 011603. eprint: quant-ph/0506106 (cit. on p. VIII).

[165] D. A. Steck. *Alkali D line data*. URL: http://steck.us/alkalidata/ (cit. on p. IX).

[166] K. E. Miller, D. Krause, and L. R. Hunter. "Precise measurement of the Stark shift of the rubidium and potassium D1 lines". In: *Phys. Rev. A* 49 (1994), 5128–5130. URL: http://link.aps.org/doi/10.1103/PhysRevA.49.5128 (cit. on p. IX).

[167] J. Jiang and J. Mitroy. "Hyperfine effects on potassium tune-out wavelengths and polarizabilities". In: *Phys. Rev. A* 88.3 (2013), 032505. arXiv: 1308.0407 [physics.atom-ph] (cit. on p. IX).

[168] J. M. Amini and H. Gould. "High Precision Measurement of the Static Dipole Polarizability of Cesium". In: *Phys. Rev. Lett.* 91 (2003), 153001. URL: http://link.aps.org/doi/10.1103/PhysRevLett.91.153001 (cit. on p. IX).

[169] Z.-C. Yan and J. F. Babb. "Long-range interactions of metastable helium atoms". In: *Phys. Rev. A* 58 (1998), 1247–1252. URL: http://link.aps.org/doi/10.1103/PhysRevA.58.1247 (cit. on p. IX).

[170] S. G. Porsev and A. Derevianko. "Multipolar theory of blackbody radiation shift of atomic energy levels and its implications for optical lattice clocks". In: *Phys. Rev. A* 74 (2006), 020502. URL: http://link.aps.org/doi/10.1103/PhysRevA.74.020502 (cit. on p. IX).

[171] T. M. Miller and B. Bederson. "Measurement of the polarizability of calcium". In: *Phys. Rev. A* 14 (1976), 1572–1573. URL: http://link.aps.org/doi/10.1103/PhysRevA.14.1572 (cit. on p. X).

[172] A. E. Blechman. *A Mathematics Primer for Physics Graduate Students*. Version 2.0. 2007. URL: http://www.pha.jhu.edu/~blechman/papers/mpri.pdf.

[173] *Mathematica Stack Exchange*. question and answer site for users of Mathematica. Wolfram Research. URL: http://mathematica.stackexchange.com/.

[174] H. F. Ebel and C. Bliefert. *Bachelor-, Master- und Doktorarbeit: Anleitungen für den naturwissenschaftlich-technischen Nachwuchs*. 4th ed. Weinheim: WILEY-VCH, 2009. URL: http://d-nb.info/994010869.

Danksagung

Für die vielfältige Inspiration, tatkräftige Unterstützung und stete Motivation die zu allem beigetragen haben was diese Arbeit ausmacht, möchte ich an alle daran beteiligten Personen meinen Dank aussprechen.

Insbesondere geht mein Dank an meinen Betreuer und Arbeitsgruppenleiter Dr. René Gerritsma: Nachdem er und Prof. Dr. Ferdinand Schmidt-Kaler mein Interesse für die faszinierende Welt der kalten Ionen geweckt hatten, öffnete ein von ihm betreuter Seminarvortrag mein Fenster zur Quantensimulation. Sowohl schon vor Beginn, bei der Anmeldung, als auch über die gesamte Dauer meiner Masterarbeitsphase hinweg, zeigte er größtes Engagement. Er war stets gerne bereit sein Wissen in allen angrenzenden Themen der Physik zu teilen — seien es vielfältigste Theorien zur Physik des hybriden Experiments oder experimentelle Techniken im Labor. Sei es zur Vorbereitung auf die Vorträge im Rahmen meiner Masterarbeit oder während der Anfertigung dieser Arbeit gewesen, sein kompetenter Rat und konstruktive Kritik sind stets eine große Hilfe gewesen. Sein Forschergeist, Wissensdurst und die Beharrlichkeit in theoretischen Untersuchungen mit Mathematica sind äußerst ansteckend für mich gewesen. Danke für die intensiven, meist 2π-mal länger dauernden Diskussionen, bei denen es nicht allzu selten um 2π selbst ging. So konnte ich einerseits viel von ihm lernen, aber andererseits ließ er mir auch die Freiheit das facettenreiche Themengebiet selbst zu studieren und zudem über den Tellerrand hinaus zu blicken, was ich sehr gutheiße.

Prof. Dr. Patrick Windpassinger danke ich für die Ermöglichung eines Gastforscheraufenthaltes in Hamburg am ZOQ/ILP in der Quantengas-Gruppe von Prof. Dr. Klaus Sengstock und der Betreuung eines Seminarvortrages im Vorfeld dieser Arbeit. Hierdurch erhielt ich einen Einblick in die ebenso interessante Welt der ultrakalten neutralen Atome. Auch die Doktoranden seiner Arbeitsgruppe QOQI, Maria Langbecker, Florian Mühlbauer und Mohammad Noaman sind nette und hilfsbereite Kollegen gewesen.

Wie vom Himmel gefallen kam die neu entstandene Arbeitsgruppe HyQS, in der die beiden Welten der ultrakalten Ionen und Atome nun hybridisiert werden sollten. Insbesondere danke ich den beiden *atom-ion* Doktoranden mit denen ich hier zusammen arbeiten durfte: Jannis Joger, der mich in allen Lagen stets hilfreich unterstützte, vor allem beim Bau der beiden Laser und auch sonstigen technischen Fragen im Labor. Sein Wissen über die experimentellen Details und seine Fertigkeiten bei der Konstruktion der nahezu gesamten experimentellen Apparatur teilte er gern. Danke für die etlichen CAD-Zeichnungen. Auch Henning Fürst gebührt großer Dank. Durch sein gutes physikalisches Verständnis und seine Computersimulations-Fähigkeiten hatte ich auf diesem Gebiet einen diskussionsfreudigen Ansprechpartner. Alles in allem danke ich meiner Arbeitsgruppe HyQS für die angenehme, vielfältige und innovative Arbeitsumgebung und Zusammenarbeit.

Zudem danke ich den Mitgliedern der Arbeitsgruppe Kalte Ionen und Experimentelle Quanteninformation — gerade Johannes Roßnagel, Dr. Christian Tomás Schmiegelow, Marcel Salz, Vidyut Kaushal, Andreas Pfister, Max Hettrich, Henning Kaufmann, Marco Dillmann, Thomas Ruster, Georg Jacob und Stefan Ulm — für ihre aktive Unterstützung. Jedes Mitglied

hat auf seine Art das Arbeiten angenehm gemacht und diese Arbeit durch seine Fertigkeiten und Wissen bereichert. Dipl.-Ing. Heinz Lenk hatte für alle Art von Elektronikproblemen eine ausgefeilte Expertenlösung oder auch direkt Bauteile zur Hand. Außerdem geht mein Dank an das QUANTUM Sekretariat, insbesondere Christine Best und Elvira Stuck-Kerth, die stets ein offenes Ohr für allerlei Anliegen hatten und für unmittelbare und tatkräftige Unterstützung sorgten. Während meiner Bachelorarbeit, die Prof. Schmidt-Kaler dankenswerterweise betreut hat, stellte Johannes Roßnagel als unmittelbar betreuender Doktorand eine enorme Hilfe dar. Auch im Rahmen dieser Arbeit wirkte er inspirierend durch kritische Diskussionen zu den theoretischen Untersuchungen, wie auch Dr. Christian Tomás Schmiegelow.

Grundsätzlich danke ich all meinen Lehrern, die mein Interesse an der Physik und Naturwissenschaft maßgeblich geprägt haben: so z.B. Christian Treitz im Leistungskurs Physik, Rolf-Hartmut Lochmann in der Mathematik und Physik, und Inge Metz in der Biologie. Ohne Sie hätte ich womöglich nie den Weg des Physikstudiums eingeschlagen. Zu meinem Glück konnte ich die Quantenoptikvorlesungen von Dr. Kilian Singer besuchen, wo er seine unfassbar ansteckende Begeisterung für Quantenoptik und Quanteninformation überschwappen ließ. Außerdem haben seine Elektronik-Skills zu dem ein oder anderen kreativen Lösungsansatz bei Elektronikproblemen im Rahmen dieser Arbeit geführt.

Ein besonderer Dank geht an die Kommilitonen die mich durch mein Studium begleitet haben, ganz besonders Valéry, Matthias und Jens. Sei haben die Studienzeit nicht nur studien-technisch, sondern auch persönlich bereichert, ebenso wie alle anderen Freundinnen und Freunde. Danke an die Korrekturleser dieser Arbeit. Zu guter Letzt möchte ich mich zutiefst bei meinen Eltern für alles bedanken — Euer Verständnis für meine Begeisterung, Eure vielfältige Unterstützung während meines Studiums, und den Rückhalt und die Liebe die Ihr mir entgegenbringt.

Ach ja, übrigens... Natur & Universum... Danke, dass es Euch gibt und Ihr es Uns scheinbar wie von selbst ermöglicht habt, Euch von Uns nach und nach erforschen — oder Uns zumindest in dem Glauben — zu lassen.

“Remember kids: The only difference between screwing around and science is writing it down.”

*Adam Savage (*1967). MythBusters.*

Eidesstattliche Erklärung

Ich, Norman Vincenz Ewald, versichere, dass ich diese Abschlussarbeit zur Erlangung des akademischen Grades Master of Science selbstständig verfasst und keine anderen als die angegebenen Quellen und Hilfsmittel verwendet sowie wortgetreue als auch sinngemäße Zitate, geistiges Eigentum und Forschungsergebnisse anderer Veröffentlichungen als solche kenntlich gemacht habe. Diese Arbeit ist in gleicher oder ähnlicher Form noch nicht veröffentlicht und noch keinem anderen Prüfungsamt vorgelegt worden.

Mainz, den _____ _____
[Datum] [Unterschrift]

Norman Vincenz Ewald
Hybrid atom-ion Quantum Systems (HyQS)
AG QUANTUM
Institut für Physik
Johannes Gutenberg-Universität Mainz
Staudingerweg 7
D-55128 Mainz
ewaldn@uni-mainz.de